

H4.SMR/1586-7

**"7th Workshop on Three-Dimensional Modelling
of Seismic Waves Generation and their Propagation"**

25 October - 5 November 2004

**Regional Studies of Crustal Anelasticity
Based upon Lg Coda and Surface Waves**

Brian J. Mitchell

Department of Earth & Atmospheric Sciences
St. Louis University,
U.S.A.

Regional Studies of Crustal Anelasticity Based upon Lg Coda and Surface Waves

Brian J. Mitchell
Department of Earth & Atmospheric Sciences
Saint Louis University

CONTENTS

Part 1. Lg Coda Q

Reference: Xie, J., and B.J. Mitchell, A back projection method for imaging large-scale lateral variations of Lg coda Q with application to continental Africa, *Geophys. J. Int.*, 100, 161-181, 1990.

Part 2. Models of shear-wave Q from multimode spectra – Frequency-independent models

Reference: Jemberie, A.L., and B.J. Mitchell, Shear-wave Q structure and its lateral variation in the crust of China and surrounding regions, *Geophys. J. Int.*, in press, 2004.

Part 3. Models of shear-wave Q from multimode spectra – Frequency-dependent models

Reference: Jemberie, A.L., and B.J. Mitchell, Frequency-dependent shear-wave Q models for the crust of China and surrounding regions, *Pure Appl. Geophys.*, 162, 1-16, 2004.

A back-projection method for imaging large-scale lateral variations of *Lg* coda *Q* with application to continental Africa

J. Xie and B. J. Mitchell

Department of Earth and Atmospheric Sciences, St Louis University, 3507 Laclede, St Louis, MO 63103, USA

PUBLICATION No. _____
IN GEOLOGY and GEOPHYSICS
SAINT LOUIS UNIVERSITY

Accepted 1989 April 5. Received 1989 April 4; in original form 1989 January 20

PUBLICATION No. 322
IN GEOLOGY and GEOPHYSICS
SAINT LOUIS UNIVERSITY

SUMMARY

A new method is developed which uses back-projection tomography to regionalize large-scale lateral variations of coda *Q* for *Lg* waves which have traversed long continental paths. Successful use of this method requires precise and stable single-trace measurements of *Lg* coda *Q* (Xie & Nuttli 1988). The method converges rapidly and requires minimal computer storage. It also allows quantitative estimation of resolution and error in imaging lateral variations of coda *Q*. The spatial resolution of this method is limited by the uneven spatial coverage of the data base, by our limited knowledge of *Lg* coda generation, and by the trade-off between the stability and the spatial resolution of the coda *Q* inversion. The method is applied to a large set of digital *Lg* coda data from Africa, where large-scale lateral variations of *Lg* coda *Q* are found to correlate well with major tectonic features. Most of Africa is stable, and like other stable regions, has relatively high coda *Q* values. The lowest values of coda *Q* are associated with the African rift system. Other regions of low-*Q* values include the Atlas mountains and Cape Fold Belt, regions of Mesozoic and younger deformation. The lateral variation of frequency dependence of *Lg* coda *Q* correlates, in most regions, with that of *Q* at 1 Hz. Our analysis of the spatial resolution of this method indicates that the resolving power of *Lg* coda *Q* imaging is comparable to that of velocity tomography using long-period surface waves. Using empirical approaches, we estimate that uncertainties in *Lg* coda *Q* and its power-law frequency dependence parameter are less than about 60 and about 0.2, respectively, for most of Africa.

Key words: *Lg* coda *Q*, back-projection tomography, Africa.

1 INTRODUCTION

Developments in seismic tomography in recent years have greatly advanced the study of lateral variations of velocity structure in continental areas. By contrast, little progress has been made in imaging lateral variations of *Q* of the Earth using tomographic algorithms (Nolet 1987). This is largely due to the lack of precision and stability in *Q* measurements, as well as the lack of a sufficiently large and well-distributed data base.

Vertical-component, high-frequency (~1 Hz) *Lg* waves can be treated as a superposition of higher-mode Rayleigh waves propagating within the continental crust (Knopoff, Schwab & Kausel 1973; Der *et al.* 1984; Kennett 1984). It is reasonable to assume that in the absence of large-scale disruption of the crustal wave guide, *Q* derived from *Lg* or its coda is representative of *Q* of the continental crust (e.g.

Singh & Herrmann 1983; Der *et al.* 1984; Campillo 1987). In this paper we define *Lg Q* as *Q* derived from the direct *Lg* phase and *Lg* coda *Q* as *Q* derived from *Lg* coda. Measuring *Lg Q* requires either records from two stations on the same great circle path or a record from one station produced by an event for which we have knowledge of the source spectrum (Cheng & Mitchell 1981; Campillo 1987). With data currently available, these requirements will likely result in very poor ray path coverage for studying lateral variations of *Q*. *Lg* coda *Q* can, however, be measured at a single station without knowledge of the source spectrum (Aki & Chouet 1975; Herrmann 1980; Xie & Nuttli 1988); it is therefore more useful than *Lg* itself for the study of large-scale lateral variations of *Q*. The interpretation of *Lg* coda, however, is more difficult than that of *Lg*. Because high-frequency coda is highly random, it is difficult to model *Lg* coda properly and regionalized coda *Q* values resulting

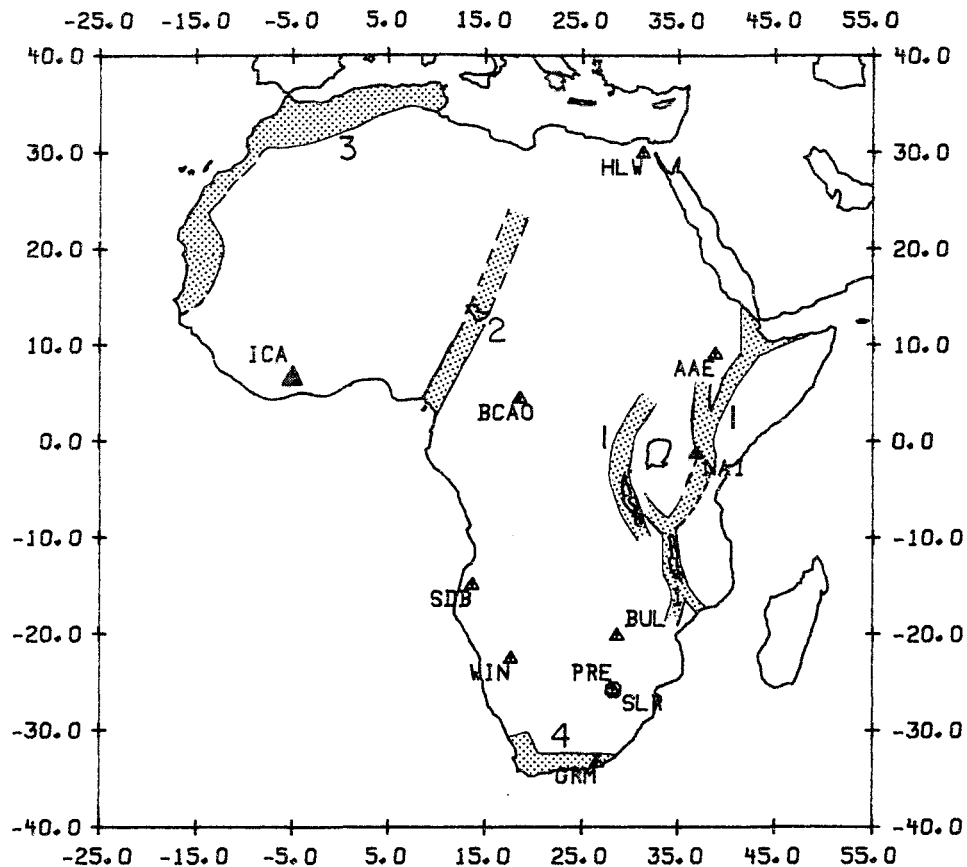


Figure 1. Map showing the locations of seismicographic stations used in this study (triangles and circles), and areas that have been affected by orogenies or large-scale rifting in the last 425 million years (shaded areas): 1, the East African Rift system; 2, the Cameroon rift (or the Cameroon volcanic line) system; 3, the Atlas Mountains; 4, the Cape Fold Belt. Adopted from Clifford (1970), Dott & Batton (1971) and Cahen *et al.* (1984). ICA indicates the Ivory Coast Array.

from inversion may be characterized by large uncertainties. Nevertheless, several studies have determined lateral variations of L_g coda Q (or local coda Q derived from local S -wave coda) in major continental areas such as North and South America and China, using a master curve technique (Herrmann 1980; Singh & Herrmann 1983; Raouf & Nuttli 1985; Jin & Aki 1988). The results of these studies generally show good correlation between lateral variations of Q and the main tectonic features of the continents studied.

In order to improve the precision and stability of L_g and Q measurements, Xie & Nuttli (1988) proposed a stochastic model for L_g coda. They discussed the effects of various physical processes (e.g. dispersion, mode conversions, scattering) which affect the generation of L_g coda. They approximated the randomness of L_g coda by band-limited white, Gaussian noise. This approach allows a quantitative estimate of the variance of Q determined by the inversion process. A stacked spectral ratio (henceforth denoted as SSR) method was proposed for L_g coda Q inversion which allows cancellation of station site effects (provided that those effects are stationary) and results in a large reduction of the variance. Improved Q values obtained by the SSR method, plus the rapid evolution of techniques used in seismic tomography, make it possible to develop more quantitative, or computerized, methods to image lateral variations of L_g coda Q , with more rigorous analysis of error and resolution.

Africa is a continent where no systematic investigation of crustal Q has been conducted. Almost all of Africa has been free of orogenic activity for about the past 500 million years (Clifford 1970; Cahen *et al.* 1984). Africa has some unique and interesting tectonic features, the most striking being the well-developed rift systems and volcanic lines (Moreau *et al.* 1987) in east and west Africa, with lengths of thousands of kilometres (Fig. 1). Other noteworthy features of this continent are the younger mountain ranges at both the southern and northern margins. The Cape Fold Belt in the south and the Atlas mountains in the north were affected by Hercynian or younger orogenies.

2 INVERSE METHODS

As in velocity tomography, the imaging of lateral variations of L_g coda Q proceeds in two steps. First, individual seismograms containing coda are collected and processed to obtain Q values, each being a functional of the distribution of regional L_g Q (or more strictly, of regional L_g coda Q) inside an area sampled by the single-trace coda record. Second, many single-trace measurements are combined to image the lateral variations of Q . A major difference between L_g coda Q tomography and velocity tomography is that the forward modelling involved in the former method must take into account the elliptical region over which

scattering occurs whereas the latter considers seismic waves that are restricted to single paths.

2.1 Single-trace measurement of coda Q

High-frequency coda is highly random and the generation of Lg coda involves various complicated physical processes such as scattering, dispersion, mode summation and mode conversion (Der *et al.* 1984; Snieder 1987; Xie & Nuttli 1988). Consequently, two problems arise in the interpretation of the single-trace coda records. First, because of the randomness of coda it is difficult to obtain a Q estimator which is stable enough to provide an acceptable variance (Der *et al.* 1984). Second, a coda Q estimator may be subject to systematic deviations from an Lg Q estimator due to imprecise forward modelling. In order to solve these two problems Xie & Nuttli (1988) derived a stochastic model and an inverse method for the interpretation of single-trace Lg coda signals. They used a convolutional relationship to model the processes of Lg coda generation. That relationship allows the effect of those processes to be expressed and examined separately in the frequency domain. In particular, they found that the single isotropic scattering (SIS) model can satisfactorily explain previous observations on several major continents, and that the randomness of the Lg coda signal can be approximated by simple band-limited white, Gaussian noise. The latter approximation allows a quantitative estimation of the theoretical variance of coda Q inversion. Xie & Nuttli (1988) found that unacceptably low confidence levels in the Lg coda Q inversion results could occur if a carefully designed variance reduction procedure was not used. At large epicentral distances the problem of low confidence levels can be very serious due to the narrow pass-band of the Q filter. They therefore proposed a SSR method to reduce the variance resulting from the inversion. For convenience of discussion we briefly summarize the SSR method in the following paragraphs.

First, the Lg coda time series is divided by a number, N_w , of non-overlapping time windows with a constant window length, T , where the m th window has a centred lapse time τ_m , and $m = 1, 2, \dots, N_w$. For each window of the time series the discrete Fourier transform is performed to obtain the geometrical mean of the amplitude spectrum, $\langle A_{k,m} \rangle$, at the k th discrete frequency $f_k = k/T$, defined as

$$\langle A_{k,m} \rangle = \prod_{i=k-l}^{k+l} |A_{i,m}|^{1/(2l+1)}, \quad (1)$$

where the subscripts i and k represent discrete frequencies, and m denotes the window number. $|A_{i,m}|$ is the i th discrete amplitude spectral estimate obtained by applying the discrete Fourier transform to the m th windowed time series and $2l+1$ is an integer, which gives the number of amplitude spectral estimates used in each geometrical mean.

The SSR is defined as

$$F_k = \frac{1}{M} \sum_{m=1}^M \frac{1}{\pi(\tau_{M+m} - \tau_m)} \log \left[\frac{G_{M+m} \sqrt{U_m} \langle A_{k,m} \rangle}{G_m \sqrt{U_{M+m}} \langle A_{k,m+M} \rangle} \right], \quad (2)$$

where M is given by

$$M = \begin{cases} N_w/2 & \text{if } N_w \text{ is even} \\ (N_w + 1)/2 & \text{if } N_w \text{ is odd} \end{cases} \quad (3)$$

U_m is the length of each group velocity window for Lg given by

$$U_m = v \tau_m (1/v_{\min} - 1/v_{\max}) \quad (4)$$

where v , v_{\max} and v_{\min} are the average, maximum and minimum group velocities of the Lg wave train, respectively; G_m is the geometrical spreading term which can be expressed as

$$G_m = \left[\frac{1}{4\pi^2 R \sqrt{v^2 t^2 / R^2 - 1}} \Big|_{t=\tau_m} \Delta\phi \right]^{-1/2}, \quad (5)$$

where $\Delta\phi$ is given by

$$\Delta\phi = \int_{\phi=\phi_1}^{\phi_2} d\phi = \phi_2 - \phi_1. \quad (6)$$

We have replaced the symbol η in Xie & Nuttli (1988) by ϕ in order to avoid confusion with the frequency dependence of Q in equation (7) of this paper. Equation (6) is obtained using equations (A1) through (A5) of Xie & Nuttli (1988) but is more general than equation (A5) because here we have generalized the limits of integration for ϕ . When part of the integration path, which is an ellipse, is missing, the numbers ϕ_1 and ϕ_2 can be found using equation (A4) of Xie & Nuttli (1988). An example of this situation is the case when the ellipse intercepts a continental boundary which is non-transmissive to Lg waves. Otherwise $\Delta\phi$ is 2π and the resulting G_m from equation (5) becomes

$$G_m = (2\pi R)^{-1/2} (v^2 \tau_m^2 / R^2 - 1)^{-1/4}. \quad (5')$$

The right-hand side of equation (2) is calculable from a coda time series.

Assuming a power law for the frequency dependence of Q

$$Q(f) = Q_0 f^\eta, \quad (7)$$

where Q_0 and η are Q at 1 Hz and the frequency dependence of Q , respectively, Xie & Nuttli (1988) used linear regression to find η and Q_0 from

$$\log F_k = (1 - \eta) \log f_k - \log Q_0 + \epsilon, \quad (8)$$

where ϵ represents a random error. Both theoretical and observational calculations show that the SSR provides a statistically stable Q estimator, with the resulting standard error in Q_0 being an order of magnitude smaller than Q_0 itself.

A possible source of major systematic deviations of the Lg coda Q estimator from the LgQ estimator is the use of an incorrect geometrical spreading term, G_m in equation (2). Using available observations conducted in various areas, including central Asia, North America and southern Africa, Xie & Nuttli (1988) made a comparison between the LgQ_0 and Lg coda Q_0 calculated from applying the SIS model to digital coda data, and concluded that the geometrical spreading term G_m calculated using the SIS model can be used to calculate the value of Lg coda Q_0 and that that value is close to LgQ_0 averaged over the same area. These areas have widths of about 10^3 km. This conclusion is semi-empirical and many aspects on the generation of Lg coda still remain unclear. For instance, we do not yet understand the details of mode conversion, nor why the SIS model appears to be valid. A further

complication is that the stochastic modeling of Lg coda may be non-unique (Xie & Nuttli 1988).

2.2 Spatial interpretation of single trace coda Q measurements

In order to obtain an image of lateral variation of Lg coda Q which closely resembles the lateral variation of LgQ , one has to interpret single-trace measurements of Lg coda Q in terms of laterally varying LgQ , i.e. one has to make an *a priori* assumption about how the single-trace measurements of Lg coda Q depend on the laterally varying LgQ inside the area sampled by Lg coda. From considerations of the afore-mentioned non-uniqueness in modelling Lg coda and the unclear aspects of Lg coda generation, we think it is premature to assume a detailed, perhaps non-linear, functional relationship of such a dependence to image lateral variation of LgQ . Additional problems in any attempt at using such a detailed functional relationship comes from the tremendous computation time and computer storage involved, and the probability of numerical instabilities (Xie & Mitchell 1988). On the other hand, the Lg coda time series is typically longer than 300 s, thus the moving window stacking defined by equation (2) utilizes many windows and results in a stable measurement of Q . Assuming an Lg group velocity of 3.5 km s^{-1} and single scattering, the area sampled by the single trace Lg coda will always have a width greater than 10^3 km . This distance is about the same as the widths of the areas over which the consistency between averaged LgQ_0 and Lg coda Q_0 were observed (Section 2.1). Therefore we assume that the inverse of Lg coda Q obtained by applying the SSR method (with G_m calculated from the SIS model) to a single-trace record of Lg coda gives the areal average of LgQ^{-1} inside the elliptical area corresponding to the maximum τ_m , which will be denoted as τ_{\max} , of this record. The major and minor axes of this ellipse are given respectively by

$$a = ct/2 \Big|_{t=\tau_{\max}}, \quad (9)$$

where v is the same as in equation (4), and

$$b = \sqrt{v^2 t^2 - R^2} \Big|_{t=\tau_{\max}}, \quad (10)$$

where R is the epicentral distance [Xie & Nuttli 1988, equations (A3) and (A4); note that $r_1 + r_2 = vt$ and that the delta function in equation (A3) results in α being equal to vt/R].

Since the τ_{\max} of a coda record, under the single-scattering assumption, gives the largest possible area sampled by the Lg coda, the above assumption attributes each coda Q value measured from a single-trace record to the average LgQ over the largest possible area. We will use this assumption exclusively in imaging lateral variations of Q . Strictly speaking the image of lateral variations of Q obtained using such an assumption is the image of lateral variations of Lg coda Q , which, as indicated in the above discussion, should closely resemble the lateral variations of LgQ .

It appears that the above assumption will lead to limited resolving power in the imaging of lateral variation of coda Q . Previous practice in determining lateral variations of coda Q (Singh & Herrmann 1983; Raouf & Nuttli 1985; Jin

& Aki 1988) have assigned single-trace Q measurements to spatial points, instead of areas. We think that our assumption is more reasonable since high-frequency seismic coda samples an area rather than a spatial point. Moreover, spatial resolution in imaging lateral variations of coda Q is also limited by the random nature of the high-frequency coda signal. This causes more basic and more severe restrictions in resolution compared to any restrictions artificially caused by the assumptions used in our inversion. This basic restriction is very important and profound but has not been addressed previously. We shall give a detailed discussion on this limitation in the following paragraphs.

There is a trade-off between the stability of single-trace coda Q measurements and spatial resolution. As mentioned by Kopnichev (1980), Der *et al.* (1984) and Xie & Nuttli (1988), the high-frequency Lg coda is highly random. Thus in order to estimate coda Q using spectral ratios, stacking techniques should be used to overcome large variances or uncertainties. Stacking can be applied either to coda data from repeated paths if they are available, or to coda obtained from many time-shifted windows applied to the same single trace. Moving-window stacking (Xie & Nuttli 1988) can provide better data coverage since only one record is required for multiple measurements. In this method, as one moves toward later parts of the coda, the area sampled by the signal successively increases and the spatial resolution becomes poorer. This is a special case of the usual trade-off between variance and resolution in inverse problems (Backus & Gilbert 1970). In measuring coda Q using the master curve method (Herrmann 1980), better constrained coda Q estimates require use of predominant frequencies measured from the later part of coda, unless Q is very low (Singh & Herrmann 1983; Xie & Nuttli 1988). The method of Aki & Chouet (1975) applies linear regression to amplitudes over lapse time for each of several frequency pass-bands. More data points are needed in these regressions to reduce the uncertainty in the estimation of slope (which gives Q); thus the later part of coda is also needed in the method of Aki & Chouet (1975). Therefore to stabilize the Q -inversion using the random coda signal, the later part of coda is needed, regardless of the method used. The increased stability and the reduced uncertainty due to using the later coda, however, is achieved at the cost of poorer spatial resolving power of later coda since it samples a larger area. Eventually one achieves an acceptable uncertainty in coda Q inversion with limited spatial resolution. Compared to this primary limitation in the spatial resolution inherent in narrow-band random coda signal, the limitations associated with our assumptions are secondary and probably trivial. At short distances the low-pass effect of attenuation is not as serious as it is at large distances where Lg coda is observed; therefore for local S -wave coda recorded by broad-band instruments, the variance could be reduced by increasing $2l + 1$ (equation 1) at the cost of frequency resolution if the SSR method is used, and the trade-off could be set toward a higher spatial resolution.

2.3 Method of imaging lateral variations of Lg coda Q

In this section we propose a back-projection algorithm to image lateral variations of Lg coda Q . Suppose we have a

number (N_d) of Lg coda time series collected from a continental region. We shall denote the Q value calculated by applying the SSR method to the n th time series by \overline{Q}_n . We divide the whole area under study into a number of N_g grids with widths of W_{NS} degrees in a north-south direction and W_{EW} degrees in an east-west direction. We parametrize the unknown lateral variation of Lg coda Q by assuming it to be a constant (Q_m) inside the m th grid. Following the assumption in Section 2.2, \overline{Q}_n gives the areal average of LgQ (strictly speaking, Lg coda Q) in the elliptical area sampled by coda waves received at the maximum lapse time, τ_{max} , of the whole time trace. Denoting the area that the n th ellipse overlaps with the m th grid by s_{mn} , we have

$$\frac{1}{\overline{Q}_n} = \frac{1}{S_n} \sum_{m=1}^{N_g} \frac{s_{mn}}{Q_m} + \epsilon_n, \quad n = 1, 2, \dots, N_d, \quad (11)$$

where

$$S_n = \sum_{j=1}^{N_g} s_{jn}$$

and ϵ_n is the residual due to the errors in modelling Lg coda and in the Q measurement. Equation (11) is a sparse linear system because many of the s_{mn} 's are zero. We shall use a back-projection, or ART technique (e.g. Gordon 1974; Dines & Lytle 1979; McMechan 1984; Suetsugu & Nakanishi 1985; Humphreys & Clayton 1988) to solve equation (11). This technique is an iterative 'raw-action' procedure. Our adopted version of this technique to image lateral variation of Lg coda Q is briefly summarized as follows.

- (i) Calculate s_{mn} for all the (m, n) 's and store all the non-zero s_{mn} values.
- (ii) Construct a starting model for Q_m 's, denoted by Q_m^i , for $m = 1, 2, 3, \dots, N_g$, and $i = 0$ (the superscript i will be used to indicate the last iteration completed over all the coda records).
- (iii) For each of the n records ($n = 1, 2, 3, \dots, N_d$), calculate the updated residual Δ_n^i , defined through

$$\Delta_n^i = \frac{S_n}{Q_n} - \sum_{m=1}^{N_g} \frac{1}{Q_m^i} s_{mn}. \quad (12)$$

- (iv) For each of the m grids ($m = 1, 2, \dots, N_g$), a new estimate of Q_m , denoted by Q_m^{i+1} , is made by back projecting Δ_n^i into the inverse of the Q_m^i 's:

$$\frac{1}{Q_m^{i+1}} = \frac{1}{Q_m^i} + \frac{1}{N_i} \sum_{n=1}^{N_d} \frac{\Delta_n^i s_{mn}}{\sum_{j=1}^{N_g} s_{jn}^2}. \quad (13)$$

- (v) A nine-point spatial smoothing proposed by Suetsugu & Nakanishi (1985) is applied to smooth and stabilize the inversion. If we denote the m th grid by $m(l, j)$, where l and j are grid numbers in the east and north directions,

respectively, then the smoothed model $(Q_{m(l,j)}^{i+1})'$ is given by

$$\begin{aligned} & \frac{1}{(Q_{m(l,j)}^{i+1})'} \\ &= \frac{1}{29} \left[\frac{1}{Q_{m(l-1,j-1)}^{i+1}} + \frac{1}{Q_{m(l-1,j+1)}^{i+1}} + \frac{1}{Q_{m(l+1,j-1)}^{i+1}} \right. \\ & \quad + \frac{1}{Q_{m(l+1,j+1)}^{i+1}} + 4 \left(\frac{1}{Q_{m(l,j-1)}^{i+1}} + \frac{1}{Q_{m(l,j+1)}^{i+1}} \right) \\ & \quad \left. + \frac{1}{Q_{m(l-1,j)}^{i+1}} + \frac{1}{Q_{m(l+1,j)}^{i+1}} + \frac{9}{Q_{m(l,j)}^{i+1}} \right]. \quad (14) \end{aligned}$$

This smoothing procedure is much like a spatial Gaussian filter, and we have found that unreasonably low (or even negative) Q^{-1} values could result if this smoothing is not applied.

- (vi) Repeat the iterative procedures in (iii)–(v) until one of the following criteria is satisfied:

$$i + 1 \geq i_{max}, \quad (15)$$

or

$$\frac{\sum_{j=1}^{N_d} (\Delta_j^{i+1})^2 - \sum_{j=1}^{N_d} (\Delta_j^i)^2}{\sum_{j=1}^{N_d} (\Delta_j^i)^2} \leq \delta^2 \quad (16)$$

where i_{max} is an integer which gives the maximum iteration acceptable and δ is the relative change in the overall residual, or the relative improvement of the degree to which the model fits data. Both numbers were chosen by experience after several tests of the method. Both i_{max} and δ are set before the iteration procedure begins.

The advantages of using back-projection techniques include the minimal computer storage involved, and the rapid convergence achieved. These advantages are very important when an entire continent is being studied. The disadvantage of using this technique is that back-projection does not provide formal estimates of resolution, bias and error (Suetsugu & Nakanishi 1985). Humphreys & Clayton (1988) suggested using the 'point spreading function', which we shall denote as p.s.f., as an approximation of the resolution kernel. To obtain the p.s.f. one simply constructs a model composed of one grid with unit-valued Q^{-1} at the geographic point of interest. The Q^{-1} values in all the other grids are set at zero. Synthetic data using this model are then computed and inverted. The resulting image gives the p.s.f. at this geographic point, which in turn gives a measure of spreading of the resolution kernel.

The effect of random noise preserved in single-trace Q estimates on the final image can be empirically tested utilizing the sample standard error in \overline{Q}_n due to the randomness of SSRs (Xie & Nuttli 1988). To do so we denote the standard error associated with \overline{Q}_n by δQ_n , $n = 1, 2, 3, \dots, N_d$ (note that δQ_n is always positive due to the way standard error is estimated), and assume that δQ_n gives a good measure of the absolute value of real error preserved in the corresponding \overline{Q}_n measurements. We then empirically construct a number, N_d , of noise series, whose n th member have an absolute value equal to δQ_n and a sign that is chosen randomly. The n th term of this noise series is

then added to \overline{Q}_n , which we shall denote as

$$\overline{Q}'_n = \overline{Q}_n + \delta Q_n.$$

\overline{Q}'_n values were then inverted to obtain a new Q_m model. The difference between the new image of Q_m values using \overline{Q}'_n and the original image of Q_m values will give us an error estimation for the Q_m values. This process empirically measures the effect of random noise on the Q_m image. The sign of the δQ_n series can be simulated by pseudorandom binary generators in a computer and the process must be repeated several times to obtain an averaged, and more stable error measurement of Q_m values.

3 DATA PROCESSING

In this study we have used *Lg* coda records collected from vertical-component, short-period seismographs installed at 12 stations in continental Africa. Table 1 lists the instrument types of these seismographs, and the codes and locations of the stations. The station locations are also plotted in Fig. 1, where the Ivory Coast Array stations are clustered together and abbreviated as ICA. The data set is composed of the following.

(i) 59 digital records from stations BCAA and SLR, both belonging to the DGSN network. Events recorded by these stations occurred in the years 1979 through 1985.

(ii) 155 analogue records from WWSSN stations AAE, BUL, GRM, HLW, NAI, PRE, SDB and WIN. Events recorded by these stations occurred primarily in the years 1973 and 1974, but two nuclear explosions occurred on 1963, October 20 and 1965, February 27.

(iii) 39 analogue records from the Ivory Coast Array stations. Twelve events recorded at these stations occurred during the years 1978 through 1984. The Ivory Coast Array has five short-period (~1 Hz), vertical seismographs with an instrument response similar to that of WWSSN instruments. These seismographs are located within tens of kilometres of each other. Four of them are high-gain instruments (magnification ≥ 125 k), and one is low-gain (magnification = 62.5 k). We have chosen to use three or four (depending on how many were available to us with acceptable record length and signal/noise ratios) of the records from the high-gain instruments in this study. The response of these instruments varied quite frequently during the years of recording events, but these variations have no effect when the SSR method is used (Xie & Nuttli 1988).

Table 1. Seismographic stations used in this study.

Station Code	Latitude	Longitude	Type of Instrument†
AAE	9.0300° N	38.8000° E	WWSSN
BCAO	4.4335° N	18.5354° E	SRO
BUL	20.1430° S	28.6130° E	WWSSN
DIC	6.6700° N	4.7700° W	IC *
GRM	33.3133° S	26.5733° E	WWSSN
HLW	29.8580° N	31.2420° E	WWSSN
KIC	6.3606° N	4.7411° W	IC *
LIC	6.2244° N	5.2778° W	IC *
NAI	1.2739° S	36.8037° E	WWSSN
PRE	25.7533° S	28.1900° E	WWSSN
SLR	25.7349° S	28.2816° E	DWWSSN
TIC	6.6447° N	5.0200° W	IC *
WIN	20.1430° S	28.6130° E	WWSSN

† all instruments are short period, vertical component

* Ivory Coast Stations. These instruments have responses similar to that of 1-Hz short-period WWSSN instruments.

All of the analogue seismograms were digitized at St Louis University. Figs 2 and 4 display some typical digitized seismograms from WWSSN and Ivory Coast Array stations, respectively. Together with the digital seismograms, we have a total number of 253 *Lg* coda time series. This makes the digital *Lg* coda data set used in this study the largest ever collected for a major continent. Each of the coda time series were segmented by many windows with the centred lapse time, τ_m , starting at roughly the arrival of group velocity of 3.15 km s^{-1} and increasing to successively cover the entire portion of the signal which can be distinguished from the ambient noise. We used a 10 per cent Hanning window with a length of 30 s for the digitized analogue data and a length of 25.6 s for the digital GDSN data. The reference noise spectra for each record were obtained in the way described by Xie & Nuttli (1988), i.e., from the portion of the trace prior to the *P* arrival. The Fast Fourier transform (FFT) was performed on both signal and noise and the effect of noise was empirically reduced by subtracting the reference power spectra of noise from power spectra of the signal. The SSR, defined by equation (2), was then obtained for single-trace *Q* measurements. Table 2 lists the event dates, recording stations, epicentral distances, back-azimuths and the resulting single-trace measurements of *Lg* coda *Q*, together with the estimated standard errors. Fig. 3 gives some examples of the SSR analysis using the digitized WWSSN records displayed in Fig. 2. The frequency band used is from 0.5 to 2.0 Hz. It is noteworthy that the SSR estimated from the event dated 1974 May 5 recorded by station BUL (middle of Fig. 1) fluctuated more than others, perhaps because of fundamental-mode interference. Some examples of SSR analysis using GDSN data can be found in Xie & Nuttli (1988). All of the events recorded by the Ivory Coast Array were a few thousand kilometres from the stations, giving virtually the same traveltimes to all the stations (Table 1). In this case we have treated the records of the same event collected from all the available stations belonging to this array as records of a repeated path and obtained a more stable *Q* measurement by averaging the SSR over the whole array. This permitted us to use a shorter coda time series (roughly 200–300 s), but to still have rather small sample standard errors. Figs 4 and 5 give examples of this averaging process. Fig 4 shows the time traces and Fig. 5 shows the SSRs calculated from each station (curves), their average (dots) and the linear regression over the average (line), together with the resulting Q_0 and η (denoted by z in the plot), and their standard errors.

The lengths of the coda time series we used are between 200 and 800 s. We have determined the sampling areas of these coda records under the assumptions that each coda time series samples an elliptical area with axes given by equations (9) and (10) and that the boundary separating oceanic crust from continental crust forms a non-transmissive barrier to the *Lg* wave. When such a boundary is encountered by the *Lg* wave coming from the continental side, some part of the energy carried by this wave is scattered back into the continental side and the remaining energy is converted into other types of seismic waves which propagate into the oceanic crust or mantle. We further assume that the scattering at this boundary is isotropic and is not abnormally strong, compared to the scattering caused by

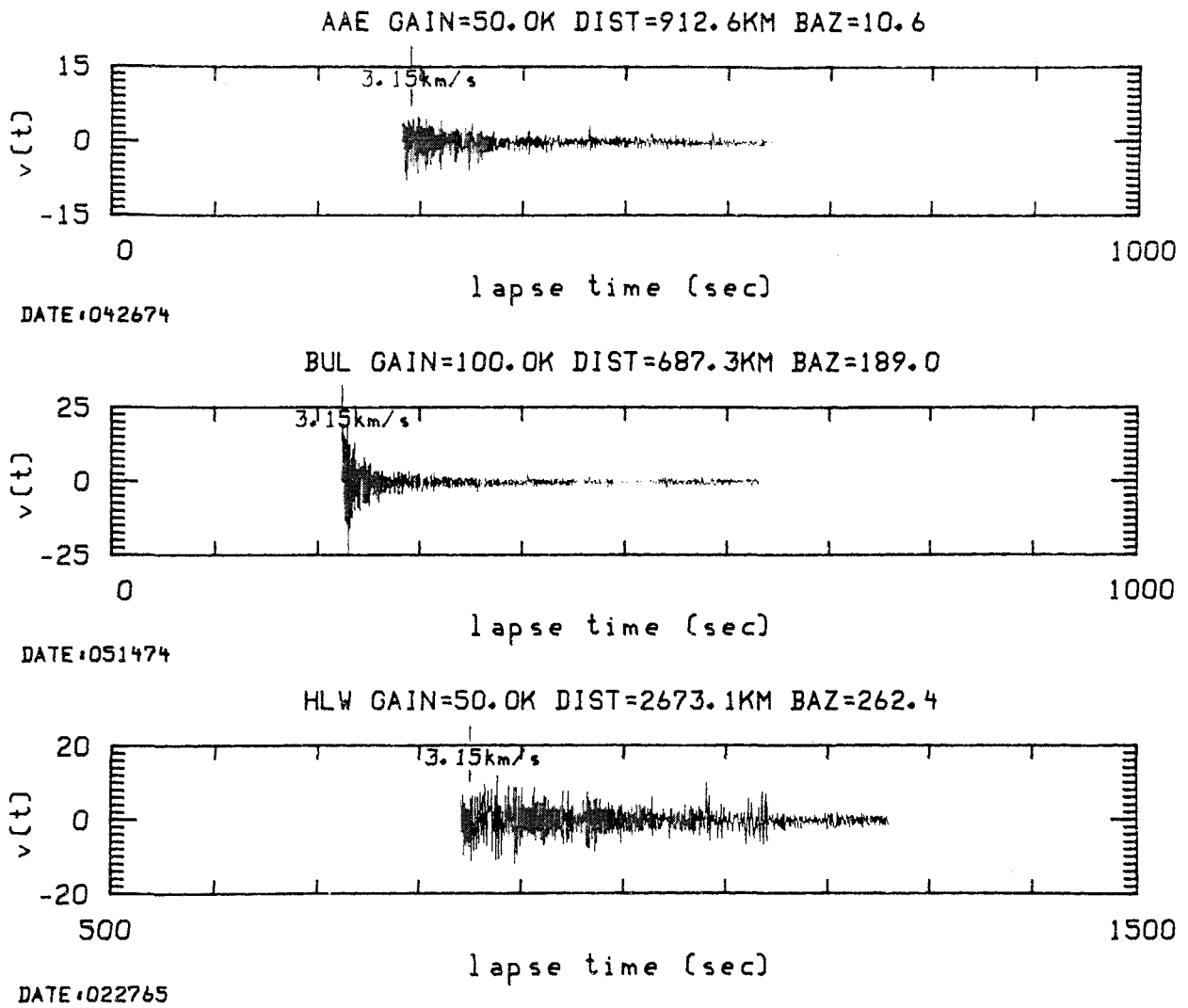


Figure 2. Three typical short-period, vertical-component WWSSN seismograms showing L_g coda. The abscissa indicates the lapse time measured from the earthquake origin time. The seismograms were digitized from analogue records. The station code, gain of the instrument, epicentral distance and back-azimuth (in degrees) are shown above each trace. The event date is indicated below each trace and the arrival times of group velocities of 3.15 km s^{-1} are identified.

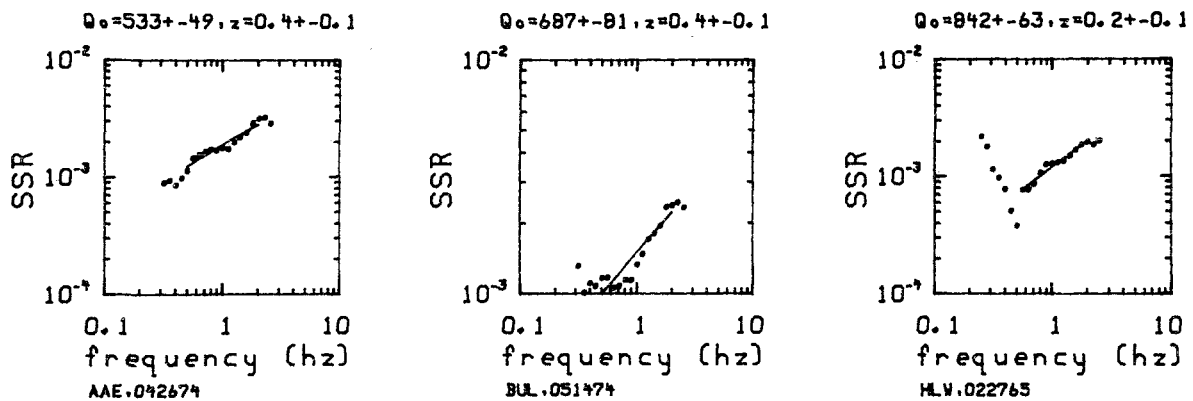


Figure 3. Q_0 and frequency dependence (denoted by η in text and by z in this plot) values and their standard errors obtained by linear regression using SSR values calculated from the records plotted in Fig. 2. The frequency band used is 0.5–2.0 Hz. At lower frequencies the spectral ratio estimates in the middle plot (station BUL) shows some fluctuations, probably due to the fundamental-mode interference.

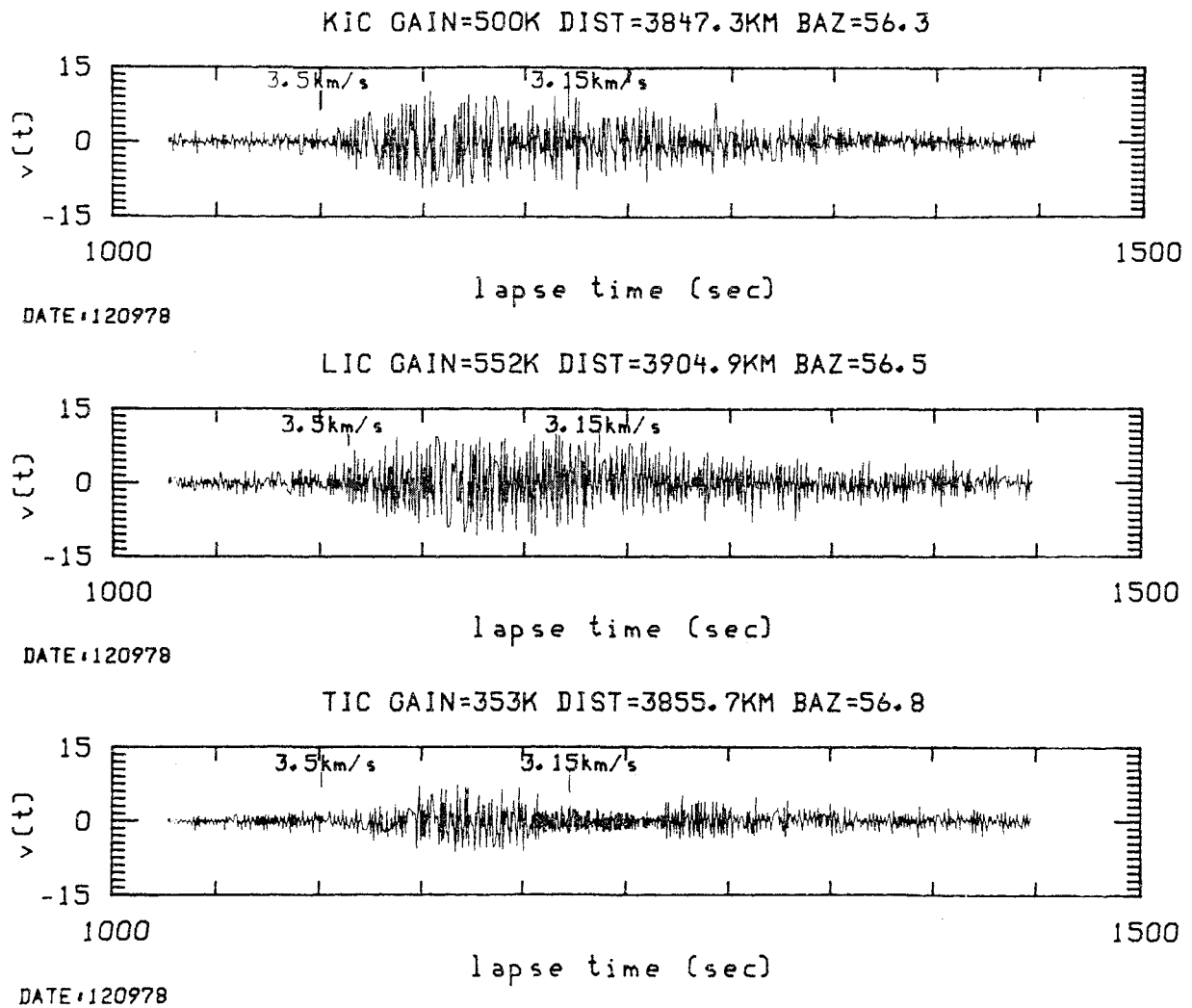


Figure 4. Typical short-period, vertical-component seismograms at three Ivory Coast Array stations showing the long duration of Lg and Lg coda. The abscissa indicates the lapse time. The event is the same for all of the traces. The station code, instrument gain, epicentral distance, and back-azimuth (in degrees) are above each trace. The event date is indicated below and near the beginning of each trace, and the arrival times of waves with group velocities of 3.50 and 3.15 km s^{-1} are identified.

Table 2. Events used and the corresponding results of single-trace analysis of Lg coda Q , with sample standard errors.

Event Date	Origin Time [†]	Recording Station	Epicentral Distance(km)	Back Azimuth	Q_0	η
102063	13h0m0.0s	AAE	3948.9	299.0	724 ± 67	0.3 ± 0.2
022765	11h30m0.0s	AAE	3949.5	299.0	690 ± 91	0.4 ± 0.2
010773	12h17m12.6s	AAE	468.2	207.5	454 ± 40	0.5 ± 0.1
011373	6h5m42.2s	AAE	3076.5	201.9	510 ± 83	0.5 ± 0.1
011473	13h36m59.8s	AAE	1991.2	208.5	461 ± 53	0.5 ± 0.1
030573	23h59m46.6s	AAE	2133.2	346.0	712 ± 89	0.3 ± 0.2
040173	6m29m27.7s	AAE	534.2	57.4	449 ± 49	0.5 ± 0.1
040573	1h59m12.6s	AAE	908.0	66.2	493 ± 54	0.5 ± 0.1
040773	19h17m38.7s	AAE	530.0	55.0	518 ± 34	0.5 ± 0.1
041373	14h13m56.9s	AAE	633.4	59.0	468 ± 61	0.5 ± 0.1
041573	13h13m33.4s	AAE	2024.7	208.1	452 ± 61	0.5 ± 0.3
042273	22h3m43.5s	AAE	1014.1	236.6	499 ± 52	0.5 ± 0.1
051473	20h16m26.8s	AAE	1951.7	210.7	475 ± 56	0.5 ± 0.1
052473	7h15m8.5s	AAE	2211.0	194.7	478 ± 75	0.5 ± 0.2
070773	16h4m9.9s	AAE	1387.7	195.2	425 ± 62	0.6 ± 0.2
071873	19h39m13.0s	AAE	2285.0	192.2	477 ± 55	0.5 ± 0.2
112473	14h5m46.4s	AAE	4591.5	316.1	810 ± 109	0.3 ± 0.2
120173	16h51m14.0s	AAE	1383.3	228.5	441 ± 59	0.5 ± 0.2
021874	9h59m45.7s	AAE	1704.1	217.7	453 ± 65	0.5 ± 0.1
031774	7h31m25.2s	AAE	995.0	298.9	683 ± 53	0.4 ± 0.1
041774	18h27m33.7s	AAE	924.7	10.4	528 ± 45	0.4 ± 0.2
042574	0h3m49.1s	AAE	1310.3	227.8	511 ± 57	0.5 ± 0.1
042674	18h8m16.9s	AAE	912.6	10.6	533 ± 47	0.4 ± 0.1
042974	20h4m39.7s	AAE	2489.4	343.8	721 ± 65	0.3 ± 0.2

Table 2. (continued)

Event Date	Origin Time †	Recording Station	Epicentral Distance(km)	Back Azimuth	Q_0	η
063074	13h26m24.7s	AAE	777.0	6.8	563 ± 49	0.4 ± 0.1
090474	6h29m16.4s	AAE	3717.3	319.5	790 ± 112	0.3 ± 0.2
110880	7h54m18.2s	BCAO	3979.2	334.1	604 ± 61	0.5 ± 0.1
111080	0h1m49.4s	BCAO	3954.2	335.8	537 ± 56	0.7 ± 0.5
111780	8h29m51.6s	BCAO	1661.0	144.4	602 ± 41	0.5 ± 0.1
112080	1h38m29.3s	BCAO	2954.6	142.3	600 ± 37	0.4 ± 0.2
120780	17h37m9.7s	BCAO	3920.0	335.3	557 ± 73	0.6 ± 0.1
020181	13h19m59.2s	BCAO	3940.4	336.2	507 ± 57	0.8 ± 0.3
030481	1h58m55.8s	BCAO	1373.8	103.8	565 ± 26	0.5 ± 0.1
032881	22h28m5.4s	BCAO	3091.2	145.9	664 ± 85	0.4 ± 0.3
071981	8h7m49.8s	BCAO	2664.2	159.5	569 ± 84	0.5 ± 0.4
072381	6h21m52.0s	BCAO	301.7	145.4	796 ± 22	0.3 ± 0.1
031282	4h33m56.8s	BCAO	1478.6	129.2	525 ± 40	0.5 ± 0.1
042282	4h24m54.3s	BCAO	1305.5	129.7	618 ± 120	0.5 ± 0.1
051082	12h47m27.9s	BCAO	2002.0	136.3	652 ± 24	0.5 ± 0.2
060582	19h36m2.3s	BCAO	1381.5	126.7	580 ± 59	0.6 ± 0.1
070382	23h21m1.2s	BCAO	1467.5	127.8	638 ± 55	0.4 ± 0.1
070482	2h22m1.4s	BCAO	1467.3	128.0	644 ± 50	0.4 ± 0.1
072282	9h22m57.9s	BCAO	1349.3	113.5	520 ± 45	0.6 ± 0.1
072482	3h51m41.6s	BCAO	1333.1	105.1	599 ± 51	0.6 ± 0.1
080382	12h19m9.2s	BCAO	1776.8	134.8	611 ± 49	0.6 ± 0.3
080482	1h42m15.3s	BCAO	3093.5	144.5	574 ± 16	0.5 ± 0.3
080682	21h43m23.7s	BCAO	2381.8	159.9	514 ± 48	0.5 ± 0.3
082082	12h57m33.3s	BACO	2599.4	34.1	653 ± 62	0.5 ± 0.2
082182	5h46m1.6s	BCAO	2392.3	160.0	675 ± 97	0.5 ± 0.2
092582	21h51m27.6s	BCAO	1776.8	132.2	665 ± 12	0.6 ± 0.1
110882	18h29m47.7s	BCAO	1770.9	153.9	513 ± 23	0.3 ± 0.2
111882	8h43m19.1s	BCAO	1474.6	125.8	574 ± 19	0.5 ± 0.2
120482	18h3m45.4s	BCAO	1991.2	134.0	758 ± 73	0.6 ± 0.2
120782	9h36m3.3s	BCAO	1807.3	134.2	654 ± 20	0.7 ± 0.3
122282	0h44m50.0s	BCAO	1089.9	117.9	657 ± 38	0.5 ± 0.1
122782	2h43m9.1s	BCAO	2162.3	121.6	570 ± 35	0.6 ± 0.1
011583	16h34m7.8s	BCAO	1366.0	108.2	527 ± 59	0.6 ± 0.2
011783	4h18m16.6s	BCAO	3092.5	145.4	698 ± 71	0.6 ± 0.2
020383	13h46m2.3s	BCAO	3299.8	30.40	811 ± 97	0.2 ± 0.4
022683	19h49m19.1s	BCAO	2121.1	115.5	651 ± 44	0.4 ± 0.1
110283	2h35m12.8s	BCAO	2088.5	112.8	593 ± 75	0.6 ± 0.2
011184	18h40m29.6s	BCAO	1568.9	138.6	768 ± 78	0.5 ± 0.5
011484	13h36m10.3s	BCAO	1686.2	139.8	413 ± 19	0.6 ± 0.3
083084	10h26m49.4s	BCAO	1694.5	141.3	599 ± 57	0.5 ± 0.2
101484	20h41m17.9s	BCAO	1277.2	148.2	396 ± 42	0.4 ± 0.2
103084	15h24m7.5s	BCAO	1162.8	132.8	530 ± 33	0.6 ± 0.1
111784	11h42m45.1s	BCAO	1668.7	141.2	614 ± 39	0.4 ± 0.3
022385	14h45m35.9s	BCAO	1864.7	132.4	646 ± 156	0.5 ± 0.5
022885	16h55m47.2s	BCAO	3063.7	30.3	797 ± 32	0.2 ± 0.1
052885	6h1m32.3s	BCAO	1699.5	127.6	587 ± 57	0.6 ± 0.4
062185	20h41m4.1s	BCAO	1673.1	141.4	401 ± 26	0.7 ± 0.3
062885	22h46m19.8s	BCAO	1381.9	123.3	544 ± 42	0.6 ± 0.2
090385	9h49m22.9s	BCAO	1323.5	116.5	430 ± 21	0.5 ± 0.2
011373	6h5m42.4s	BUL	369.7	355.9	641 ± 53	0.4 ± 0.1
011473	13h36m59.8s	BUL	1480.1	7.3	454 ± 50	0.5 ± 0.1
030973	13h1m46.5s	BUL	882.7	190.0	628 ± 49	0.4 ± 0.1
031173	10h40m6.2s	BUL	400.6	350.6	681 ± 65	0.3 ± 0.2
040873	0h28m18.7s	BUL	1344.6	17.1	573 ± 55	0.5 ± 0.1
041573	13h13m33.4s	BUL	1443.6	7.4	560 ± 66	0.5 ± 0.1
041973	2h12m12.7s	BUL	376.5	352.7	672 ± 57	0.5 ± 0.2
050373	2h27m13.0s	BUL	1367.1	19.6	545 ± 60	0.4 ± 0.1
050773	18h1m2.2s	BUL	412.8	348.9	694 ± 68	0.3 ± 0.2
051473	15h22m41.2s	BUL	507.8	88.6	660 ± 46	0.3 ± 0.1
051473	20h16m26.8s	BUL	1537.5	6.0	506 ± 63	0.4 ± 0.2
052773	9h26m0.7s	BUL	1239.2	30.3	533 ± 48	0.4 ± 0.1
053173	4h19m35.8s	BUL	1374.4	19.1	561 ± 54	0.5 ± 0.2
070773	16h4m9.9s	BUL	2027.8	22.6	509 ± 79	0.5 ± 0.2
071673	18h8m20.0s	BUL	1223.9	30.5	598 ± 39	0.4 ± 0.1
072573	16h59m39.2s	BUL	1011.6	44.3	528 ± 60	0.5 ± 0.2
090173	11h23m54.6s	BUL	894.3	327.0	759 ± 69	0.3 ± 0.1
090773	23h27m50.9s	BUL	531.2	105.8	705 ± 64	0.3 ± 0.1
092173	11h12m48.8s	BUL	1606.6	36.0	563 ± 78	0.3 ± 0.2
121473	15h4m10.5s	BUL	1707.5	358.4	652 ± 53	0.3 ± 0.2
020474	1h29m48.8s	BUL	388.4	353.9	714 ± 49	0.3 ± 0.1
021074	16h29m26.4s	BUL	1994.9	342.7	747 ± 48	0.3 ± 0.2
032174	12h17m37.0s	BUL	686.4	189.8	643 ± 39	0.4 ± 0.1
042474	18h59m53.0s	BUL	747.3	343.1	661 ± 45	0.4 ± 0.1
051474	6h51m15.4s	BUL	687.3	189.0	617 ± 43	0.4 ± 0.1
062474	15h12m57.3s	BUL	691.6	191.3	649 ± 52	0.3 ± 0.1
062574	15h27m32.7s	BUL	687.1	191.6	623 ± 55	0.4 ± 0.2
072374	14h9m56.0s	BUL	733.9	192.7	581 ± 63	0.3 ± 0.2
091774	14h30m54.9s	BUL	1387.8	16.1	527 ± 67	0.5 ± 0.2
100474	17h4m52.6	BUL	1122.3	33.0	633 ± 29	0.3 ± 0.1
101174	12h3m43.7s	BUL	1269.0	200.5	544 ± 56	0.4 ± 0.2
011373	6h5m42.4s	GRM	1386.3	16.5	379 ± 31	0.5 ± 0.1
030973	13h1m46.5s	GRM	592.0	4.6	346 ± 33	0.5 ± 0.1
052473	7h15m8.5s	GRM	2646.4	17.8	369 ± 41	0.5 ± 0.2

Table 2. (continued)

Event Date	Origin Time †	Recording Station	Epicentral Distance(km)	Back Azimuth	Q_0	η
030973*	13h1m46.5s	GRM	735.9	5.9	381 ± 40	0.5 ± 0.1
022765	11h30m0.0s	HLW	2672.0	262.4	842 ± 63	0.2 ± 0.1
030573	23h59m46.6s	HLW	336.0	135.2	659 ± 44	0.4 ± 0.1
022574	16h5m15.7s	HLW	2395.2	155.8	667 ± 71	0.3 ± 0.1
031774	7h31m25.2s	HLW	1834.6	181.6	784 ± 72	0.3 ± 0.1
042574	0h3m49.1s	HLW	3193.8	182.4	662 ± 58	0.4 ± 0.1
063074	13h26m24.7s	HLW	1755.5	149.0	382 ± 25	0.6 ± 0.1
092374	19h28m17.2s	HLW	3857.1	213.5	780 ± 72	0.3 ± 0.1
020878	16h14m38.5s	ICA**	3400.0	78.5	646 ± 51	0.6 ± 0.2
060778	7h21m21.5s	ICA**	3015.9	42.7	757 ± 56	0.6 ± 0.1
120978	7h12m52.4s	ICA**	3859.7	56.4	746 ± 66	0.5 ± 0.1
121178	8h56m36.7s	ICA**	3017.2	9.5	804 ± 42	0.6 ± 0.1
101080	14h44m52.6s	ICA**	3359.9	10.4	608 ± 32	0.8 ± 0.2
101380	6h37m39.2s	ICA**	3365.7	10.8	676 ± 74	0.8 ± 0.2
120380	10h31m20.1s	ICA**	3376.6	10.3	651 ± 45	0.5 ± 0.1
111481	9h5m29.0s	ICA**	4438.8	60.4	768 ± 43	0.6 ± 0.1
091182	21h40m12.2s	ICA**	3379.7	11.2	681 ± 61	0.5 ± 0.1
093083	18h58m14.3s	ICA**	5321.7	79.8	565 ± 61	0.6 ± 0.1
031584	19h0m37.2s	ICA**	3341.4	21.9	701 ± 66	0.5 ± 0.1
070284	1h46m58.9s	ICA**	4683.8	59.2	662 ± 67	0.6 ± 0.1
010773	12h17m12.6s	NAI	722.3	0.4	455 ± 49	0.5 ± 0.2
011473	13h36m59.8s	NAI	948.4	229.3	436 ± 35	0.5 ± 0.1
031173	10h40m6.2s	NAI	1945.5	209.2	499 ± 40	0.4 ± 0.1
040573	2h56m48.0s	NAI	1940.9	209.1	507 ± 37	0.5 ± 0.2
040773	19h17m38.7s	NAI	1584.0	24.5	421 ± 50	0.5 ± 0.1
040873	0h28m18.7s	NAI	946.4	212.5	409 ± 55	0.5 ± 0.1
041373	14h13m56.9s	NAI	1651.4	27.7	440 ± 50	0.5 ± 0.1
041573	13h13m33.4s	NAI	974.5	227.8	419 ± 45	0.5 ± 0.1
041973	2h12m12.7s	NAI	1955.7	208.4	460 ± 40	0.5 ± 0.1
042273	22h3m43.5s	NAI	848.4	312.5	403 ± 35	0.5 ± 0.1
050373	2h27m13.5s	NAI	910.6	209.3	428 ± 29	0.5 ± 0.2
051473	15h22m41.2s	NAI	2097.1	189.7	457 ± 46	0.5 ± 0.1
051473	20h16m26.8s	NAI	932.8	233.3	449 ± 31	0.5 ± 0.1
052473	7h15m8.5s	NAI	1056.4	198.4	435 ± 59	0.5 ± 0.2
070773	16h4m9.9s	NAI	245.8	214.8	431 ± 48	0.5 ± 0.1
071873	19h39m13.0s	NAI	1126.0	193.3	420 ± 48	0.5 ± 0.2
090173	11h23m54.6s	NAI	1927.7	225.8	497 ± 51	0.5 ± 0.1
092173	11h12m48.8s	NAI	767.4	177.2	430 ± 51	0.4 ± 0.2
120173	16h51m14.0s	NAI	837.4	284.6	395 ± 34	0.5 ± 0.1
121473	15h4m10.5s	NAI	1028.4	248.2	441 ± 57	0.5 ± 0.2
121973	3h6m58.8s	NAI	3044.6	199.7	557 ± 60	0.4 ± 0.2
012174	15h15m54.0s	NAI	2896.2	198.0	513 ± 47	0.5 ± 0.1
020174	15h49m29.2s	NAI	2178.9	212.0	558 ± 39	0.4 ± 0.1
020474	13h16m55.3s	NAI	1957.0	208.8	442 ± 51	0.5 ± 0.1
021074	16h29m26.4s	NAI	1506.2	263.1	471 ± 44	0.5 ± 0.2
021874	9h59m45.7s	NAI	841.5	254.9	460 ± 39	0.5 ± 0.1
022574	16h5m15.7s	NAI	1278.9	16.2	443 ± 37	0.5 ± 0.2
031774	7h31m25.2s	NAI	1740.8	337.7	478 ± 45	0.4 ± 0.2
062474	15h12m57.8s	NAI	2945.5	199.5	573 ± 47	0.4 ± 0.1
072374	14h9m56.0s	NAI	2990.1	199.7	581 ± 40	0.4 ± 0.1
011373	6h5m42.4s	PRE	989.9	1.1	779 ± 67	0.3 ± 0.2
011473	13h36m59.8s	PRE	2101.7	6.5	612 ± 79	0.4 ± 0.2
022073	15h19m51.7s	PRE	1005.4	358.5	685 ± 68	0.4 ± 0.2
031173	10h40m6.2s	PRE	1016.4	358.9	651 ± 79	0.4 ± 0.2
040573	2h56m48.0s	PRE	1019.0	359.1	742 ± 74	0.3 ± 0.1
041573	13h13m33.4s	PRE	2065.2	6.5	673 ± 43	0.4 ± 0.2
041973	2h12m12.7s	PRE	994.4	359.8	782 ± 58	0.3 ± 0.1
050073	18h1m2.2s	PRE	1973.3	15.0	639 ± 49	0.5 ± 0.1
050873	5h22m22.9s	PRE	983.5	358.2	772 ± 67	0.3 ± 0.1
051473	15h22m41.2s	PRE	838.4	41.2	681 ± 45	0.4 ± 0.1
051473	20h16m26.8s	PRE	2159.6	5.6	623 ± 49	0.5 ± 0.1
052473	7h15m8.5s	PRE	1802.8	20.0	569 ± 55	0.4 ± 0.1
052773	9h26m0.7s	PRE	1817.9	21.8	608 ± 47	0.5 ± 0.1
053173	4h19m35.8s	PRE	1981.6	14.7	645 ± 57	0.5 ± 0.1
071673	18h8m20.0s	PRE	1801.8	21.9	635 ± 48	0.4 ± 0.1
071873	19h39m13.0s	PRE	1739.7	23.4	611 ± 57	0.4 ± 0.1
082873	22h43m16.7s	PRE	1912.9	9.8	623 ± 56	0.4 ± 0.2
090173	11h23m54.6s	PRE	1440.9	342.1	761 ± 53	0.3 ± 0.1
090773	23h27m50.9s	PRE	730.1	49.5	632 ± 39	0.4 ± 0.1
110373	21h35m44.4s	PRE	719.3	45.9	713 ± 51	0.4 ± 0.1
020174	15h49m29.2s	PRE	898.5	345.3	751 ± 71	0.3 ± 0.2
020474	1h29m48.8s	PRE	1007.2	0.2	687 ± 56	0.3 ± 0.2
020474	13h16m55.3s	PRE	998.8	359.3	730 ± 68	0.3 ± 0.2
021074	16h29m26.4s	PRE	2584.5	347.6	761 ± 51	0.3 ± 0.1
040874	6h12m49.2s	PRE	2377.5	21.3	545 ± 62	0.5 ± 0.2
042474	18h59m53.0s	PRE	1347.2	352.6	754 ± 53	0.4 ± 0.1
022765	11h30m0.0s	SDB	4406.6	347.7	590 ± 61	0.5 ± 0.1
040982	2h33m58.7s	SLR	885.0	351.2	650 ± 32	0.4 ± 0.1
062582	18h0m0.8s	SLR	288.4	217.5	475 ± 72	0.6 ± 0.1
070482	2h22m1.4s	SLR	2428.4	1.7	670 ± 75	0.3 ± 0.1
080482	1h42m15.3s	SLR	1087.7	41.6	623 ± 66	0.5 ± 0.1
080682	21h43m23.7s	SLR	1124.3	347.5	625 ± 88	0.4 ± 0.1
081982	14h6m13.1s	SLR	292.0	21.3	505 ± 72	0.5 ± 0.1

Table 2. (continued)

Event Date	Origin Time †	Recording Station	Epicentral Distance(km)	Back Azimuth	Q_0	η
120482	18h3m45.4s	SLR	1979.4	10.3	612 ± 70	0.4 ± 0.1
081884	10h50m1.1s	SLR	2021.2	359.0	708 ± 150	0.3 ± 0.1
082584	20h37m49.8s	SLR	1929.6	14.0	600 ± 124	0.4 ± 0.1
022285	14h45m35.9s	SLR	2094.2	8.2	464 ± 48	0.6 ± 0.1
050885	11h35m45.7s	SLR	506.8	218.4	504 ± 42	0.4 ± 0.2
051485	13h24m57.8s	SLR	2175.1	41.9	639 ± 83	0.4 ± 0.2
062885	7h32m19.9s	SLR	2158.2	41.6	623 ± 76	0.6 ± 0.3
011373	8h5m42.4s	WIN	295.0	42.4	715 ± 53	0.3 ± 0.1
011473	13h36m59.8s	WIN	2207.2	40.0	648 ± 96	0.5 ± 0.2
020673	9h50m41.4s	WIN	1171.3	113.3	722 ± 67	0.3 ± 0.1
022073	15h19m51.7s	WIN	1264.8	60.8	750 ± 78	0.3 ± 0.2
030973	13h1m46.5s	WIN	1124.4	124.2	680 ± 59	0.3 ± 0.1
031173	10h40m6.2s	WIN	1275.9	60.5	760 ± 78	0.3 ± 0.1
041573	13h13m33.4s	WIN	2176.3	40.5	600 ± 57	0.5 ± 0.2
041973	2h12m12.7s	WIN	1278.9	61.7	680 ± 53	0.3 ± 0.2
050373	2h27m13.0s	WIN	2249.3	48.4	590 ± 56	0.5 ± 0.1
050873	5h22m22.9s	WIN	1294.4	61.5	730 ± 68	0.3 ± 0.1
051473	15h22m41.4s	WIN	1669.8	83.0	580 ± 40	0.5 ± 0.1
051473	20h16m26.8s	WIN	2239.8	38.5	580 ± 56	0.5 ± 0.1
052473	7h15m8.5s	WIN	2187.9	54.4	550 ± 51	0.5 ± 0.2
052773	7h15m8.5s	WIN	2229.8	55.5	580 ± 49	0.5 ± 0.1
053173	4h19m35.8s	WIN	2250.8	48.1	590 ± 61	0.5 ± 0.2
070773	16h4m9.9s	WIN	2893.6	44.5	510 ± 52	0.6 ± 0.2
071873	18h8m20.0s	WIN	2217.6	55.8	580 ± 48	0.4 ± 0.1
071873	19h39m13.0s	WIN	2187.3	57.7	490 ± 57	0.5 ± 0.1
082873	22h43m16.7s	WIN	2106.2	45.3	590 ± 54	0.5 ± 0.1
090173	11h23m54.6s	WIN	1234.8	35.0	690 ± 63	0.3 ± 0.2
090673	20h13m35.7s	WIN	1097.5	123.9	760 ± 58	0.3 ± 0.1
110373	21h35m44.4s	WIN	1614.4	87.3	570 ± 52	0.5 ± 0.1
121473	15h4m10.5s	WIN	2280.4	31.5	550 ± 56	0.4 ± 0.1
020174	15h49m29.2s	WIN	1023.1	61.1	780 ± 75	0.2 ± 0.2
020474	13h16m55.3s	WIN	1272.6	61.3	690 ± 48	0.3 ± 0.1
021074	16h29m26.4s	WIN	2265.7	16.7	540 ± 52	0.5 ± 0.1
040874	6h12m49.2s	WIN	2715.5	48.8	500 ± 57	0.6 ± 0.2
042874	12h18m24.4s	WIN	1143.9	112.2	720 ± 57	0.2 ± 0.2
062474	15h12m57.8s	WIN	1060.9	114.6	690 ± 61	0.4 ± 0.1
072374	14h9m56.0s	WIN	1050.3	117.0	770 ± 77	0.2 ± 0.1

† The origin times for the two explosional events dated 10-20-63 and 02-28-65 were given by Bolt (1976). The origin times for all the other events were given in PRE.

* Q_0 and η listed in this line were estimated from averaging spectral ratios obtained from events 03-09-73, 06-10-73, 08-05-73, 09-06-73, 04-26-74, 05-14-74, 06-24-74.

** ICA denotes the Ivory Coast Array. The averaged spectral ratios collected from all the stations were used to estimate Q_0 and η for each event.

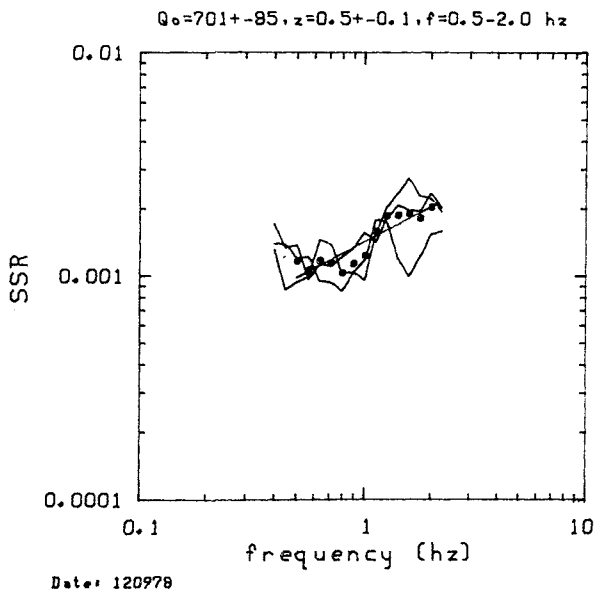


Figure 5. The SSRs calculated from each trace in Fig. 4 (curves), their average (dots) and the result of regression fitting (line) over the average. The resulting Q_0 and frequency dependence (denoted by z in this plot) and the frequency band used are given above the figure.

scatterers inland. When part of the ellipse corresponding to τ_m , the centred lapse time of the m th window (Xie & Nuttli 1988), is oceanic, equation (A4) of Xie & Nuttli has been used to determine the limits of integration [ϕ_1 and ϕ_2 in equation (6) of this paper], to exclude the oceanic crust and to determine the new geometric spreading term, G_m . Our assumption of the absence of abnormally strong scattering (or reflection) of Lg waves toward the receiver by the continental boundary is not necessarily valid in all cases. Although there have been some qualitative demonstrations of the possibility of this type of scattering or reflection, quantitative estimates of its effects are not possible at the present time (Kennett 1986). If abnormally strong scattering or reflection does occur at the continental margin our image of lateral variation of Lg coda Q obtained may be biased near those margins.

The assumption of non-transmissibility at continental margins allows us to exclude any oceanic crust in the scattering ellipse in the Lg coda Q analysis. Fig. 6 shows the pattern of coda sampling area corresponding to our data set. These areas are bounded roughly by complete ellipses corresponding to τ_{max} (equations 9 and 10) but some are truncated by the continental margin.

The density of coverage of these coda sampling areas decreases from south to north. Southern Africa has the densest coda sampling area coverage whereas northern

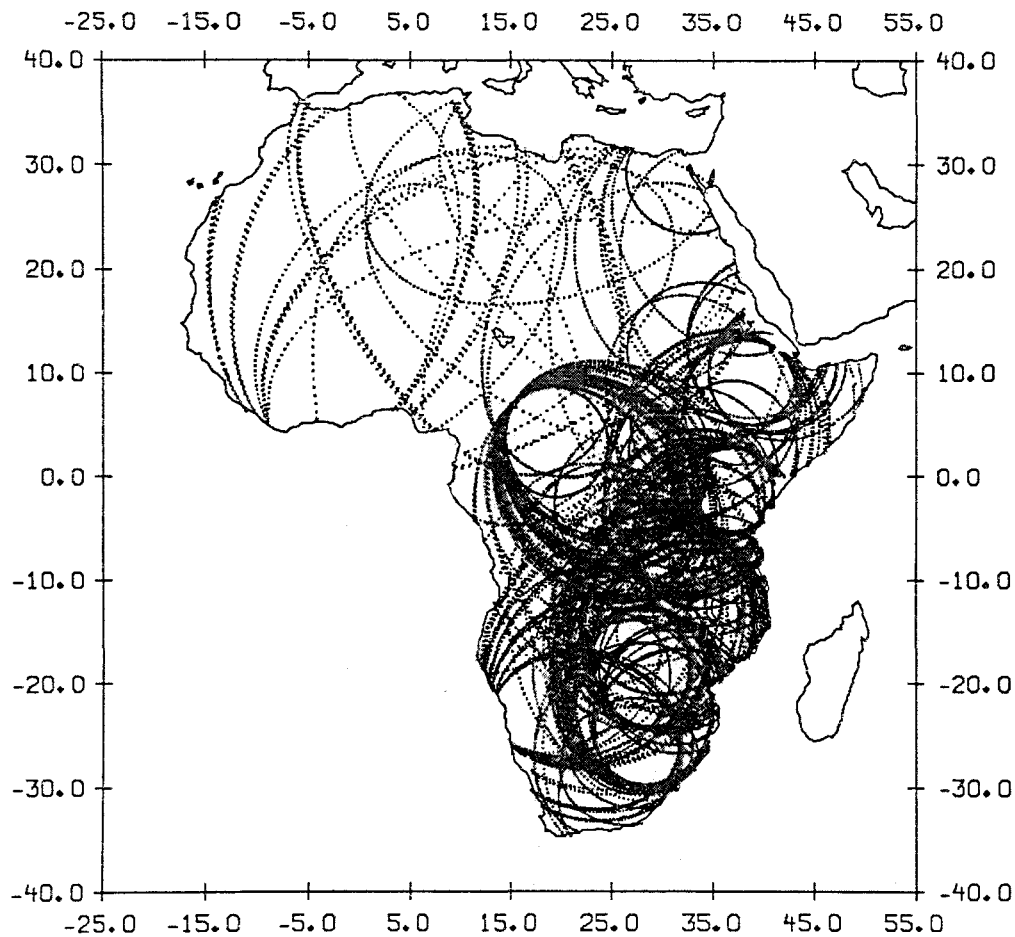


Figure 6. Sampling pattern of *Lg* coda used in this study. Each record of *Lg* coda is assumed to sample an elliptical area corresponding to the maximum lapse time used in the analysis. When the continental boundary is encountered we assume it is a barrier to the *Lg* wave and therefore the sampling area is bounded by this boundary, instead of being bounded by the corresponding segment of the ellipse which extends into the ocean.

Africa has the sparsest. For each of the records, the SSR method was applied to obtain a single-trace measurement of Q_0 and η . Examples of the SSR analysis may be found in Xie & Nuttli (1988) and in Figs 3 and 5 of this paper. Most data provide information in the frequency band between 0.5 and 2.0 Hz but digital GDSN data sometimes has high-frequency cut-offs that are higher than 2.0 Hz. Occasionally, when large-amplitude fundamental-mode waves distort coda signal at lower frequencies, we use slightly higher low cut-off values. The results of single-trace determinations of Q_0 and η , together with the sample standard error (s.s.e.), are listed in Table 2. The s.s.e. values of Q_0 are almost all within 15 per cent of Q_0 and the s.s.e. values of η are mostly within 0.2. This is consistent with the stochastic model mentioned in Section 2.1 of this paper.

4 LATERAL VARIATIONS OF *Lg* CODA Q

The back projection method in Section 2.3 is applied to image lateral variations of *Lg* coda Q in continental Africa. We have divided the whole area into 282 grids with widths W_{EW} and W_{NS} equal to 3° in latitude and longitude, respectively. The latitudes and longitudes of the centres of the grids span the area between 31.5°S , 34.5°N and 14.5°W ,

48.5°E . To find the area sampled by each coda trace we first found the corresponding ellipse in a 2-D Cartesian coordinate system, and projected this ellipse onto the surface of the Earth. Strictly speaking, on a surface with non-zero curvature, an isocron of scatterers corresponding to coda waves received at a constant lapse time is not an ellipse but a more complicated curve. However, we have found that when the axes of ellipses are shorter than approximately 2200 km the difference between the isocron obtained considering the Earth's curvature and the ellipse defined in a Cartesian system without considering the Earth's curvature differs by less than 2 per cent. Since G_m corresponding to an isocron when the Earth's curvature is considered does not have a closed-form solution and since all but a few ellipses in this study have major axes longer than 2200 km, we have ignored the effect of the Earth's curvature on Q imaging.

4.1 Lateral variation of Q_0

To use the iterative back projection method in Section 2.3 to image lateral variations of *Lg* coda Q_0 , we have used a starting model of $Q_m^0 = 600$, $m = 1, 2, \dots, N_g$ for all of continental Africa. This starting model is roughly the average of all of the single-trace measurements of Q_0 (Table

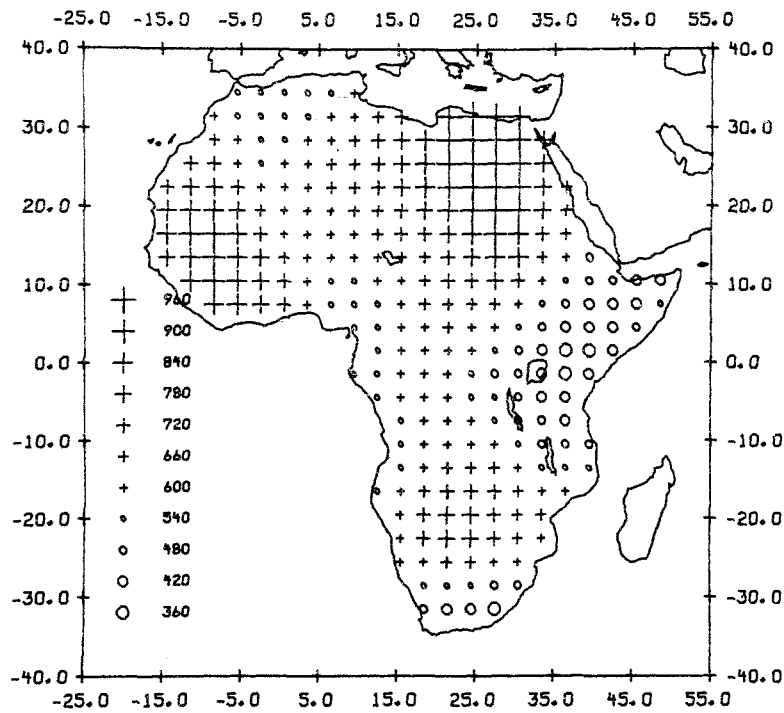


Figure 7. L_g coda Q_0 continental Africa obtained in this study. Circles represent numbers smaller than 570 and crosses represent numbers larger than 570.

2). Single-trace measurements of Q_0 were then used as \overline{Q}_n in Section 2.3 to calculate the residuals in the iteration. The stopping criteria, i_{\max} and δ , defined by equations (15) and (16), were chosen to be 20 and 10^{-5} , respectively. The latter criterion was satisfied after 14 iterations. The whole computational process, including calculation of s_{mn} values, took less than 90 min and less than 25 min of CPU time on a Masscomp MC745 and a Ridge-34 minicomputer, respectively. The variance reduction achieved was 95 per cent. After 15 iterations the left-hand side of (16) started to increase slightly, probably due to the accumulation of computer round-off errors. The resulting Q model did not vary significantly after the 14th iteration. Fig. 7 shows the resulting distribution of Q_0 in continental Africa. Circles represent Q_0 values lower than 570 and crosses represent Q_0 values higher than 570. Each symbol represents a Q_0 interval of 60, e.g. the smallest circle represents a Q_0 value between 510 and 570. The lateral variation of Q_0 is rather smooth, indicating that only large-scale variations of Q_0 are preserved. Low Q_0 values are most apparent in the East African Rift zone and the Cameroon rift (or the Cameroon volcanic line, cf. Moreau *et al.* 1987). Previous single-path observations of the direct L_g phase travelling through segments of the East African Rift also indicate low Q values in that region (Gumper & Pomeroy 1970). Low Q_0 values also occur near the southern and northern margins of Africa, where the Cape Fold Mountains and Atlas Mountains are located (Fig. 1). High Q_0 values occur in central southern Africa where the Congo craton and Kalahari Craton are located, in northwestern Africa where the west Africa craton is located (Clifford 1970; Cahen *et al.* 1984), and in northeastern Africa. The latter area contains the highest mapped Q_0 values. Although this region has undergone a complicated tectonic history (Cahen *et al.*

1984), it has not been affected by either large-scale orogeny or volcanic activity for about the last 550 million years and some basement outcrops in this area are dated at ages greater than two billion years (Klerkx 1980).

4.2 Lateral variation of η

Imaging the lateral variation of frequency dependence, η , requires another procedure. First, we obtained Q_0 and η for each coda record using the SSR method. This allowed us to calculate single-trace measurements of Q at a frequency other than 1 Hz, say at 3 Hz. These single-trace measurements were then used as \overline{Q}_n in equations (11) and (12) to calculate Q_m values at 3 Hz for each of the m grids, $m = 1, 2, \dots, N_g$. Finally, using Q_m for each grid calculated at 1 Hz (Section 4.1) and 3 Hz and assuming exponential frequency dependence of Q , we calculate η for the same grid using the relationship

$$\eta = \frac{1}{\ln 3} \ln \left[\frac{Q(f)|_{f=3\text{Hz}}}{Q_0} \right]. \quad (17)$$

Fig. 8 shows the resulting lateral variation of η in continental Africa. In southern Africa, the frequency dependence is relatively uniform (between 0.3 and 0.5), but is slightly lower (around 0.2–0.3) in central southern Africa, than near the southern margin. η is about 0.5 in the region of the East African Rift system. The areas where η values are slightly higher in southern Africa are also areas where Q_0 is lower (Fig. 7). Near the equator in central Africa (between 10°S and 10°N), η is very uniformly distributed, being about 0.5 inland and about 0.6 in coastal areas. In northern Africa η exhibits significant lateral variations. Even if the extreme values near the western and northeastern margins are ignored (because sampling

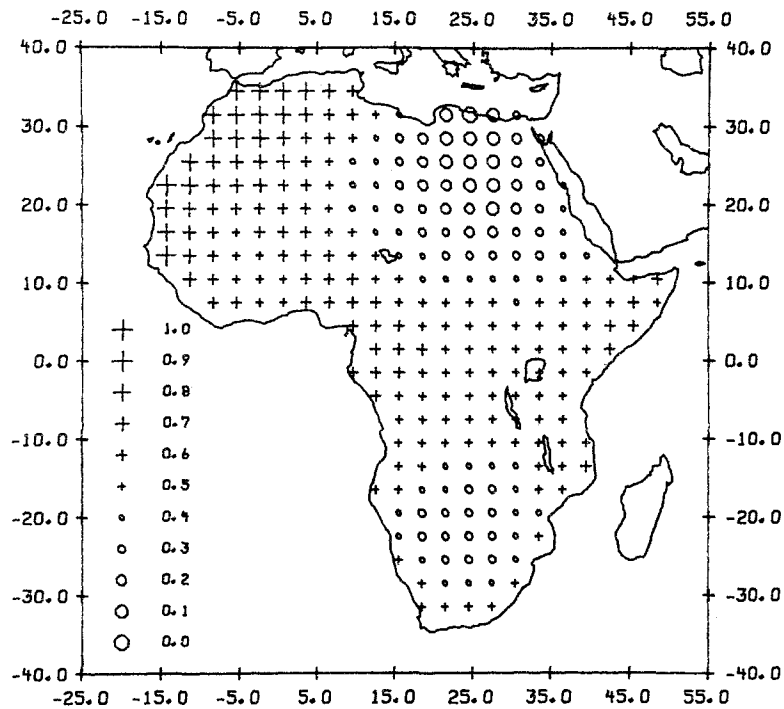


Figure 8. Frequency dependence (η) of Lg coda Q (in the vicinity of 1 Hz) in Africa. Circles represent η values smaller than 0.45 and crosses represent η values larger than 0.45.

coverage is poor), there is still a large change in η from about 0.8 in the West African shield to about 0.1 in the northeastern Africa even though Q_0 is high in both regions. Our images of lateral variation of η and Q_0 do not therefore suggest a systematic correlation between Q_0 and η throughout the whole continent. If northwestern Africa (where the west African shield is located) is ignored, however, then η appears to decrease as Q_0 increases. This tendency is most easily seen in northeastern Africa and southern Africa. Nuttli (1988) suggested that this relation is generally true throughout the world.

5 RESOLUTION AND ERROR

The imaging of Lg coda Q variations is inherently limited because of the trade-off between the stability and the spatial resolving power (Section 2.2). For this reason it is important that any study of Lg coda Q variations include an analysis of resolution and error. We have calculated the p.s.f. defined in Section 2.3 for 12 grids (Fig. 9a–g) to estimate the resolving power at the locations where these grids are centred. These locations include: 31.5°S, 24.5°E (b); 28.5°S, 18.5°E (c); 19.5°S, 30.5°E (d); 13.5°S, 24.5°E (a); 13.5°S, 24.5°E (d); 1.5°N, 30.5°E (b); 4.5°N, 21.5°E (f); 7.5°N, 39.5°E (g); 13.5°N, 39.5°E (e); 19.5°N, 3.5°E (d); 19.5°N, 18.5°E (c); 19.5°N, 33.5°E (a). All of the p.s.f. determinations were normalized such that the maximum values are unity. In general, the degree of spreading of p.s.f.'s increases from south to north. This is to be expected since the coda sampling areas are relatively dense in southern Africa and are less dense toward the north (Fig. 6). The p.s.f. plots in Fig. 9(a)–(d) show that in southern Africa the lateral variation of Lg coda Q is resolvable to spatial wavelengths of between 6° and 20°. Slightly lower

resolving power is obtained in the central part of Africa where the degree of spreading of p.s.f. plots is as low as 12° at 7.5°N and 39.5°E (Fig. 9g) and increases to between 15° and 24° further to the west (Fig. 9b and f). In the north the resolving power decreases drastically, except for some points close to continental margin where resolution spreading is still very low (around 12° to 15°, see Fig. 9a and 9e). For example, at 19.5°N, 18.5°E (Fig. 9c) and 19.5°N, 3.5°E (Fig. 9d) we cannot determine the lateral variation of Lg coda Q with confidence for spatial wavelengths of less than between 24° and 33°. In summary, the spatial wavelengths of lateral variation in Lg coda Q that are resolvable range from about 10° in southern Africa to 30° in northern Africa.

It is interesting to compare our resolution in imaging lateral variation in Lg coda Q to the resolution of 2-D surface wave velocity tomography. Several authors have conducted studies of lateral variations of long-period surface wave phase and/or group velocities in recent years. Suetsugu & Nakanishi (1985), Montagner (1986) and Hadiouche & Jobert (1988) mapped lateral variations of surface wave dispersion in the Pacific Ocean, the Indian Ocean and Africa, respectively, using data at periods between a few seconds and a few hundred seconds. In all these studies the spatial resolving power was generally limited to wavelengths of 15° to 20° or more. Resolving power in some cases was locally limited to 40° for situations where the ray coverage was poor (Suetsugu & Nakanishi 1985). Therefore the resolving power in this study using Lg coda waves at frequencies between roughly 0.5 and 2.0 Hz is comparable to that achievable in surface wave tomography at longer periods. This is somewhat surprising since surface wave tomography uses direct paths whereas imaging of lateral variations in the Lg coda Q uses scattered waves,

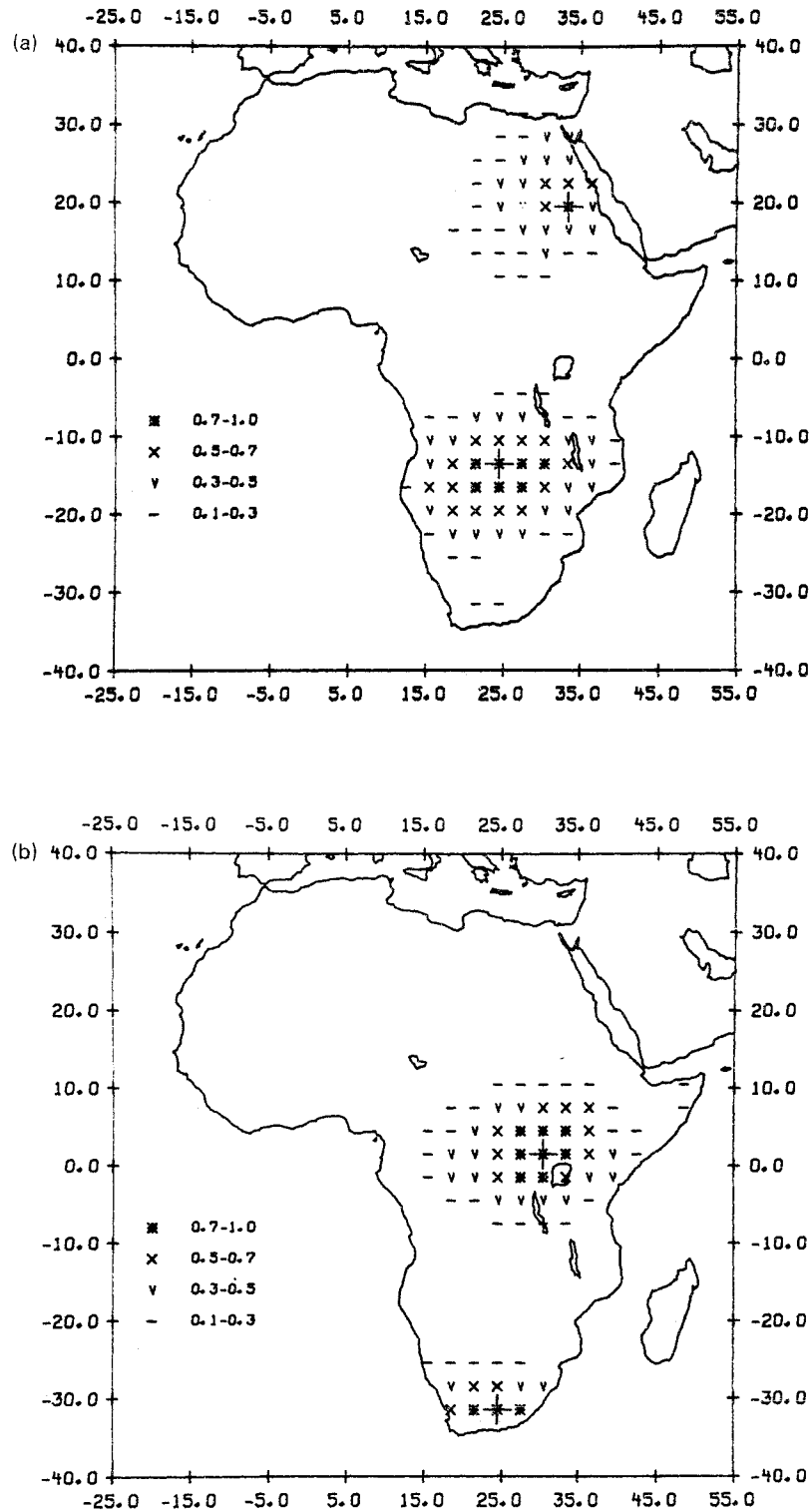


Figure 9. (a) Point spreading function (p.s.f.) plots for grids centred at 13.5°S, 24.5°E and 19.5°N, 33.5°E. The p.s.f. plots have been normalized such that the maximum value is unity. The centre of each grid is marked by a large cross. (b) p.s.f. plots for grids centred at 31.5°S, 24.5°E and 1.5°N, 30.5°E. (c) p.s.f. plots for grids centred at 28.5°S, 18.5°E and 19.5°N, 18.5°E. (d) p.s.f. plots for grids centred at 19.5°S, 30.5°E and 19.5°N, 3.5°E. (e) p.s.f. plot for the grid centred at 13.5°N, 39.5°E. (f) p.s.f. plot for the grid centred at 4.5°N, 21.5°E. (g) p.s.f. plot for the grid centred at 7.5°S, 39.5°E.

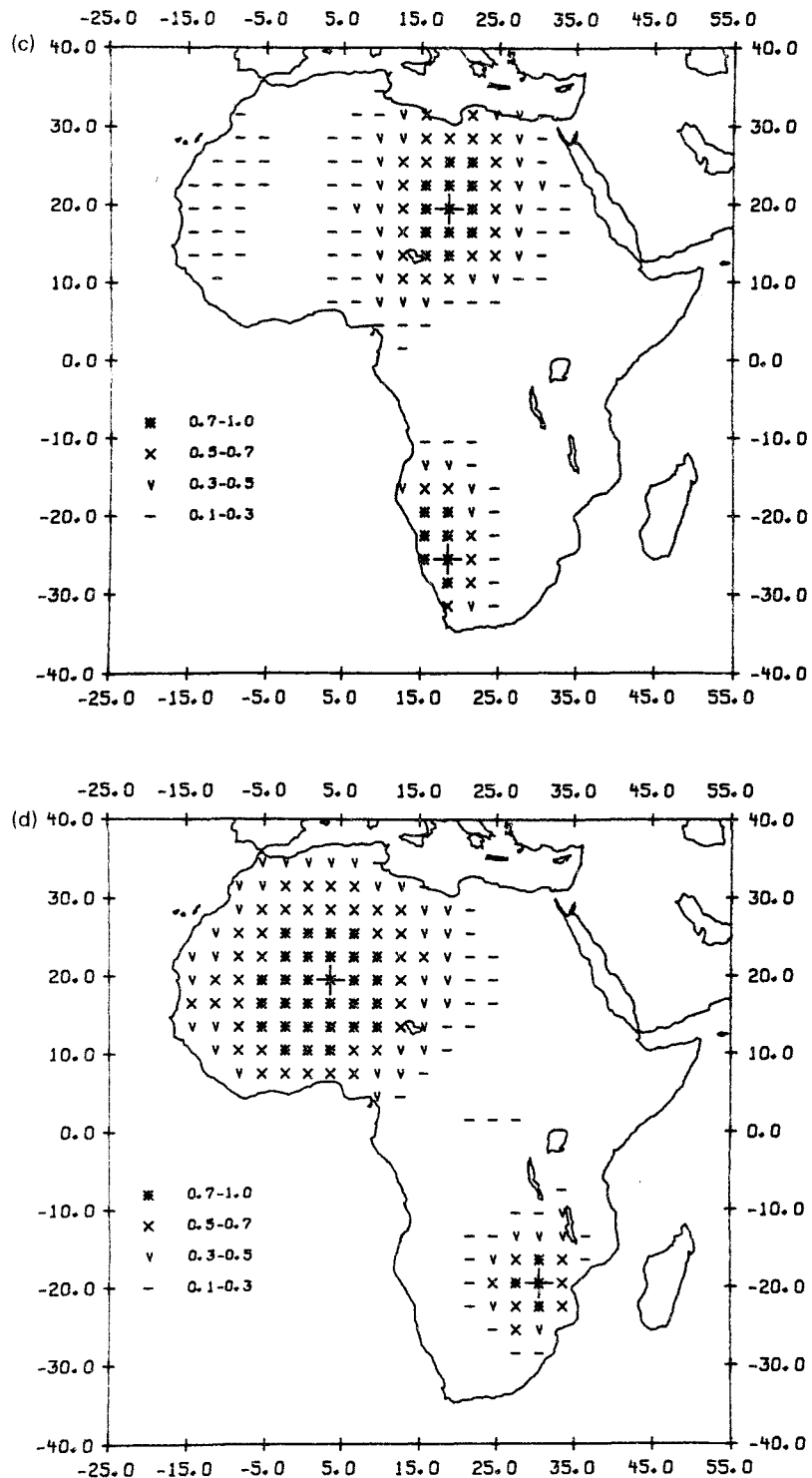


Figure 9. (Continued)

thus requiring smoothing over broader areas. A closer look at this comparison suggested that the resolving power of surface-wave tomography is limited by gaps between ray paths which are typically about 20° . The smoothing techniques used in surface-wave tomography remove these gaps in the inverted velocity image at the cost of resolution. The limitations in resolution in the present study are, however, largely due to the random nature of coda data itself (Section 2.2). Moreover the Q image may be subjected

to greater systematic errors in the single-trace measurements of Q and in their spatial interpretation than are velocity images from surface waves.

The effect of the random error in single trace measurements of Lg coda Q on the image of lateral variations in Q was estimated empirically using the method described in Section 2.3. Five tests were run to estimate the error in the image of Q_0 and η . In each of the five tests we first constructed two noise, or error series. The absolute

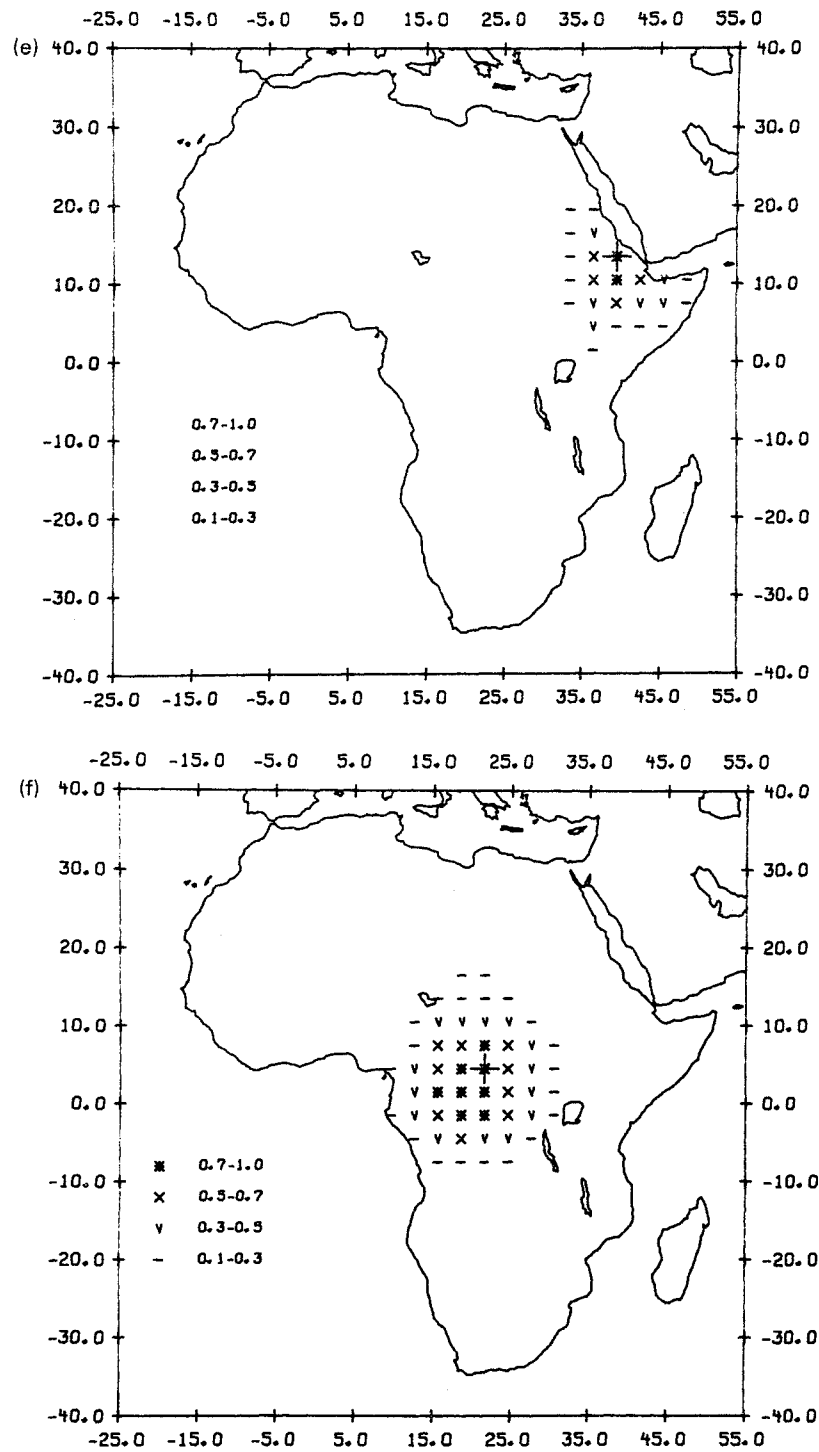


Figure 9. (Continued)

values of the n th terms of the first and the second series equal the sample standard errors in Q_0 and η calculated from the n th coda seismogram, respectively. The signs of the n th term of both noise series were randomly generated by a random binary generator. The n th terms of the two noise series were then added to the n th Q_0 and η measurements to construct a new synthetic set of Q_0 and η values. The new sets of synthetic Q_0 and η values were then inverted using the back projection method to obtain Q_0 and η for all of the grids. The differences between the Q_0 and η

values for the new image and the original image were then calculated and stored at the end of each test. After all five tests, the absolute values of the five differences in Q_0 and η for each grid were averaged. The averaged values thus obtained gave empirical estimates of absolute error in the imaged Q_0 and η values. Figs 10 and 11 give the estimated errors in Q_0 and η , respectively. The errors in Q_0 are small (less than 60) throughout most of Africa. Errors are higher, however, in western Africa and northeastern Africa, where the Q_0 values are high (Fig. 7). Since the relative error in

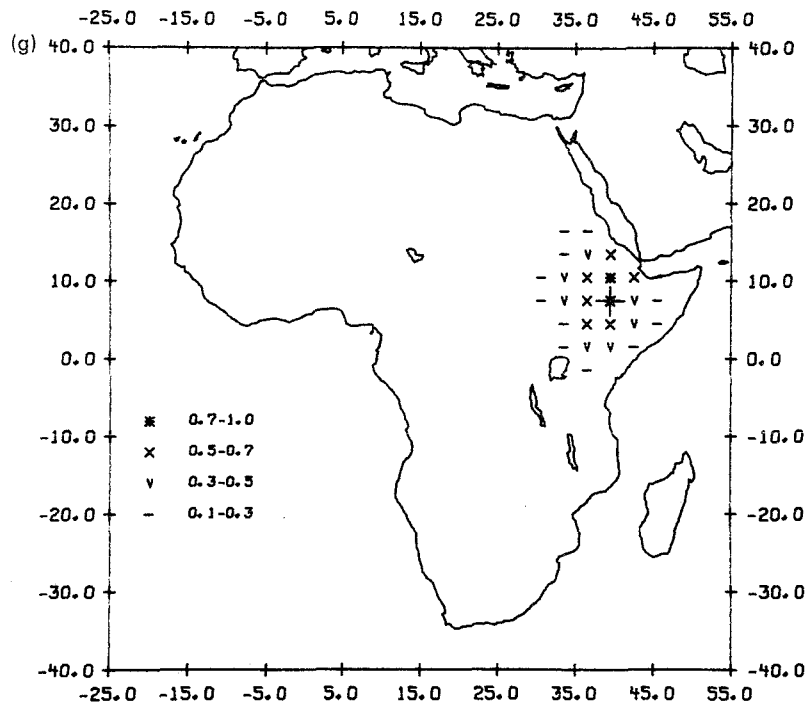


Figure 9. (Continued)

Q_0 tends to have a stochastic distribution (Xie & Nuttli 1988), the increased error in western and northeastern Africa must be partly due to the high Q_0 values. The second reason for these increased errors is the poor spatial coverage, especially along the western margin of the continent where the estimated error is as high as 300. The estimated error in η is small (0.0-0.1) throughout most of

interior Africa and is generally higher at the margins. The error in η at the northern margin is typically between 0.3 and 0.4, and is 0.5 in the region of the western margin where sampling is very poor. These calculations indicate that the errors in both Q_0 and η are inversely related to the density of the coda sampling area.

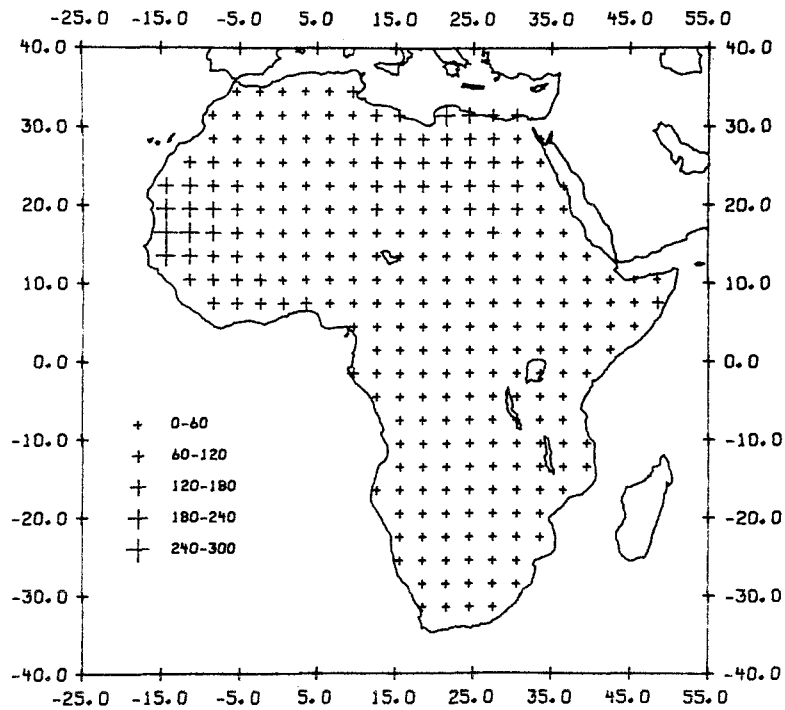


Figure 10. Error distribution in the image of lateral variation in Q_0 on continental Africa. The error is tested empirically, based on the sample standard error in the Q_0 and η values calculated from real data and the psuedo-random sign generators. See text for details.

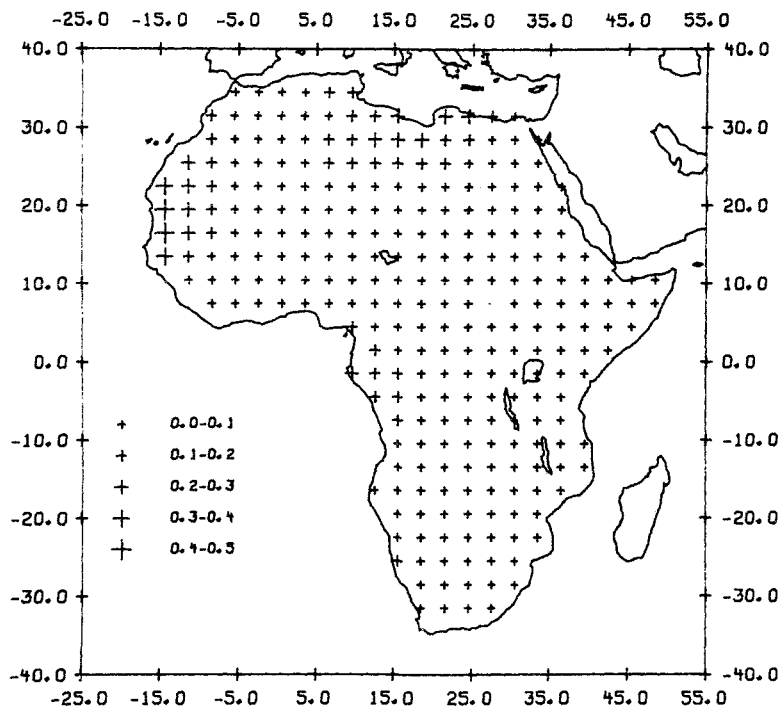


Figure 11. Error distribution in the image of lateral variation in η on continental Africa. The error is tested empirically, in the same manner as that described in Fig. 10.

6 RELATION OF Q VALUES TO GEOLOGICAL FEATURES

The map of Q_0 values in Fig. 7 exhibits broad regional variations of Q_0 values ranging between about 960 and about 360. The higher values are similar to those found in other stable regions of the world. Since almost all of Africa has been stable for the past 500 million years (Clifford 1970; Cahen *et al.* 1984), we might expect that high Q values would be typical of most of the continent. It is therefore interesting to speculate on the mechanism for the regions of low Q which are observed.

The most obvious region of high attenuation (low Q) occurs in eastern Africa and correlates well with the east African Rift system (Fig. 1). This is a region which has been subjected to extensive Cenozoic volcanism and is characterized by Lg coda Q_0 values as low as 360. Although these values are lower than those for most of Africa, they are not as low as those found throughout much of the western United States where Cenozoic volcanism has occurred (Singh & Herrmann 1983). The values in Fig. 7 are, however, averages over broad regions including rift areas as well as areas where volcanism has not occurred. It is possible that our results are averages of lower values occurring in the immediate vicinity of the rifts and higher values occurring between and outside the arms of the rifts.

The low Q values in the region of the East African Rift system can be explained as resulting ultimately from higher than normal temperatures in the crust. Morgan (1982) reported a pattern of heat flow values in which high values (up to 98 mW m^{-2}) occur on the rift floor and lower values (57 mW m^{-2}) occur on the flanks. Mitchell (1975, 1980) proposed that such higher temperatures caused enhanced

levels of hydrothermal fluids in the crust; thus low values of crustal Q can be explained by fluid flow through cracks and connected pore space in the crust by mechanisms such as those proposed by Winkler & Nur (1979) and O'Connell & Budianski (1977).

The Cameroon line running northeastward from the coast in west-central Africa appears to be characterized by relatively low values of Q_0 (about 540). This region is also the site of Cenozoic volcanism, so can be expected to have higher than normal heat flow. Its extent, however, is smaller and reductions in Q are less severe than in the East African Rift system.

The lowest values of Q outside the East African Rift system lie in the region of the Cape Fold Belt in southernmost Africa. Orogenic activity occurred there over the time span from middle Palaeozoic to early Mesozoic (Clifford 1970). Although the low Lg coda Q values in southern Africa appear to be associated with the Cape Fold Belt, the mechanism for the low values is uncertain. They can be explained either by reductions of intrinsic Q produced by interstitial fluids (Mitchell 1975, 1980) or by disruption of the crustal wave guide caused by severe topography and fluctuating thickness of sediments. Higher than normal heat flow values in much of southern Africa (Jones 1988), however, may be suggestive of the former mechanism.

Low Q_0 values (about 540) in northwestern Africa correlate geographically with the Atlas Mountains. These mountains are the result of the most recent orogenic activity in Africa, thus low Q values might be expected to occur in that region.

A broad band of low Q_0 values (about 600) runs in a southeasterly direction from a portion of the Atlas

Mountains near Gibraltar, crosses the Cameroon line, and continues southeastward to about 10°D latitude. Except near the Cameroon line and Atlas mountains, these low values cannot be related to any recent orogenic or volcanic activity in Africa. They do, however, correlate with a broad region of Mesozoic and younger sediments which is mapped in that region (Choubert & Faure-Muret 1971). Mitchell & Hwang (1987) showed that all of the regional variations of *Lg* coda Q in the stable portions of the central United States can easily be explained by high attenuation caused by accumulations of sediments of Mesozoic age and younger.

In summary, Q values throughout most of Africa are high or relatively high and are consistent with values obtained in other stable regions of the world. Low values occur in regions of Cenozoic volcanism and in the two small regions (Cape Fold Belt and Atlas Mountains) where orogenic activity has occurred as recently as the Mesozoic Era. Somewhat low values appear to be associated with broad regions of sedimentary cover of Mesozoic age.

7 CONCLUSIONS AND DISCUSSION

Taking advantage of recent developments in both more stable single-trace measurements of *Lg* coda Q and in the rapid evolution of seismic tomography, a computerized back-projection method is proposed to image large-scale lateral variation of *Lg* coda Q . Several major differences can be recognized between this method and the earlier contouring methods used by various authors. First, this method assumes that each *Lg* coda time series samples an area rather than a spatial point, thus better approximating the real coda sampling process. Second, this method is fully computerized and quantitative, yet requires very small computer memory and time. Even when a major continental area is studied, a minicomputer is more than adequate. This new method also allows quantitative estimates of resolution and error. The analysis of resolution is especially important in coda Q inversion because of the inherent randomness of signal which limits resolution.

We have collected a large amount of digital and digitized *Lg* coda data from continental Africa. Applying the back-projection method to this data base, we find that the lateral variation of Q_0 (Q at 1 Hz) correlates well with major tectonic features. The Cape Fold Belt, the Atlas Mountains, the East African rift and Cameroon rift (or the Cameroon volcanic line) are characterized by relatively low Q values whereas the shields in southern and western Africa are characterized by high Q values. Northeastern Africa, another stable region, also has high Q values. In most regions the frequency dependence, η , increases with decreasing values of Q_0 . However, higher η values were also found in the West Africa Shield where Q_0 is high. It is possible that larger errors or poorer resolution in western Africa has caused this inconsistency.

A quantitative resolution analysis indicates that the resolving power of the *Lg* coda Q image in continental Africa is limited to spatial variations with wavelengths ranging between 10° and 30°. This is comparable to the resolving power of long-period surface-wave tomography applied in earlier studies. The resolution is best in southern Africa where the coda sampling area is densest. The error analysis shows that the errors in the images of both Q_0 and

η inversely correlate with the density of coda sampling area. For most of interior Africa the error in the imaged Q_0 is lower than 60 and the error in the imaged η is less than 0.2. The largest errors occur near the northern and western margins of Africa.

Our knowledge of both the distribution and characteristics of scatterers is limited, and the quantity of available data is still very small. These limitations currently prevent us from obtaining detailed knowledge of the physical process which governs the generation and propagation of the *Lg* coda wave. Our assumption that a single-trace measurement of *Lg* coda uniformly samples an elliptical area limits the resolving power of this imaging process. A non-linear approach may overcome this limitation (Xie & Mitchell 1988), but errors in the forward modelling procedure and in the final image are likely to be larger. A non-linear approach will also greatly increase computer time and will require a very large amount of computer storage. For the present, therefore, it is preferable and more convenient to have lower resolving power than to attempt to achieve greater detail with a non-linear approach. Future work should include systematic studies of more detailed interpretations of the dynamic properties and stochastic characteristics of *Lg* and *Lg* coda, which, if combined with an increased data base, should enable us to improve the resolution and quality of the Q image.

ACKNOWLEDGMENTS

We express our gratitude to the late Otto W. Nuttli, who initiated our interest in lateral variations of *Lg* coda Q in Africa, helped us to obtain the necessary data and shared his experience in the interpretation of *Lg* and *Lg* coda. We also thank Dr R. B. Herrmann for helpful discussions, two anonymous reviewers for providing helpful suggestions, and Dr B. Massinon of Laboratoire de Detection et de Geophysique (L.D.G.), France for providing us with a large package of seismograms from the Ivory Coast Array stations. R. B. Herrmann, E. J. Haug, S. T. Morrissey and H. A. A. Ghalib assisted in implementing our computational procedures on minicomputers at The Department of Earth and Atmospheric Sciences, St Louis University. This research was supported by the Advanced Research Projects Agency of the Department of Defense and was monitored by the Air Force Geophysics Laboratory under contract F19628-87-K-0036.

REFERENCES

- Aki, K. & Chouet, B., 1975. Origin of coda waves: source, attenuation and scattering effects, *J. geophys. Res.*, **80**, 3322–3342.
- Backus, G. & Gilbert, F., 1970. Uniqueness in the inversion of inaccurate gross earth data, *Phil. Trans. R. Soc. Lond.*, **266**, 123–192.
- Bolt, B. A., 1976. *Nuclear Explosions and Earthquakes, the Parted Veil*, W. H. Freeman, San Francisco.
- Cahan, L., Snelling, N. J., Delhal, J. & Vail, J. R., 1984. *The Geology and Evolution of Africa*, Clarendon Press, Oxford.
- Campillo, M., 1987. *Lg* wave propagation in a laterally varying crust and the distribution of the apparent quality factor in central France, *J. geophys. Res.*, **92**, 12 604–12 614.
- Cheng, C. C. & Mitchell, B. J., 1981. Crustal Q structure in the United States from multi-mode surface waves, *Bull. seism. Soc. Am.*, **71**, 161–181.

- Choubert, par, G. & Faure-Muret, A., 1971. Grand bassins sedimentaires de L'Afrique occidentale, in *Tectonics of Africa*, Unesco, Paris.
- Clifford, T. N., 1970. The structural framework of Africa, in *African Magmatism and Tectonics*, eds Clifford, T. N. & Gass, I. G., Oliver & Boyd, Edinburgh.
- Der, Z., Marshall, M. E., O'Donnell, A. & McElfresh, T. W., 1984. Spatial coherence structure and attenuation the L_g phase, site effects, and interpretation of the L_g coda, *Bull. seism. Soc. Am.*, **74**, 1125-1148.
- Dines, K. A. & Lytle, R. J. 1979. Computerized geophysical tomography, *Proc. IEEE*, **67**, 1065-1073.
- Dott, R. H. & Batten R. L., 1971. *Evolution of the Earth*, McGraw-Hill, New York.
- Gordon, R., 1974. A tutorial on ART, *IEEE Trans. Nucl. Sci.*, **NS-21**, 78-93.
- Gumper, F. & Pomeroy, P. W., 1970. Seismic wave velocities and earth structure on the African continent, *Bull. seism. Soc. Am.*, **60**, 651-668.
- Hadiouche, O. & Jobert, N., 1988. Geographical distribution of surface wave velocities and 3-D upper mantle structure in Africa, *Geophys. J.*, **95**, 87-110.
- Herrmann, R. B., 1980. Q estimates using the coda of local earthquakes, *Bull. seism. Soc. Am.*, **70**, 447-468.
- Humphreys, E. & Clayton, R. W., 1988. Adaptation of back projection tomography to seismic travel time problems, *J. geophys. Res.*, **93**, 1073-1086.
- Jin, A. & Aki, K., 1988. Spatial and temporal correlation between coda Q and seismicity in China, *Bull. seism. Soc. Am.*, **78**, 741-769.
- Jones, M. Q. W., 1988. Heat flow in the Witwatersand Basin and Environs and its significance for the South African Shield geotherm and lithospheric thickness, *J. geophys. Res.*, **93**, 3243-3260.
- Kennett, B. L. N., 1984. Guided wave propagation in laterally varying media—I. Theoretical development, *Geophys. J. R. astr. Soc.*, **79**, 235-255.
- Kennett, B. L. N., 1986. L_g waves and structural boundaries, *Bull. seism. Soc. Am.*, **76**, 1133-1141.
- Klerkx, J., 1980. Age and metamorphic evolution of the basement complex around Jadal al'Awaynat, in *The Geology of Libya, Part III*, pp. 901-906, eds Salem, M. J. & Busrewil, Academic Press, London.
- Knopoff, L., Schwab, F. & Kausel, E., 1973. Interpretation of L_g , *Geophys. J. R. astr. Soc.*, **33**, 389-404.
- Kopnichev, Y. F., 1980. Statistical models for the generation of coda and short-period L_g -phases and the results of their joint interpretation, *Izv. Akad. Nauk USSR. Earth Phys.*, **16**, 99-108.
- McMechan, G. A., 1983. Seismic tomography in boreholes, *Geophys. J. R. astr. Soc.*, **74**, 601-612.
- Mitchell, B. J., 1975. Regional Rayleigh wave attenuation in North America, *J. geophys. Res.*, **80**, 4904-4916.
- Mitchell, B. J., 1980. Frequency dependence of shear wave internal friction in the continental crust of eastern North America, *J. geophys. Res.*, **85**, 5212-5218.
- Mitchell, B. J. & Hwang, H. J., 1987. Effect of low Q sediments and crustal Q on L_g attenuation in the United States, *Bull. seism. Soc. Am.*, **77**, 1197-1210.
- Montagner, J. P., 1986. Regional three-dimensional structures using long-period surface waves, *Ann. Geophys.*, **4**, 283-294.
- Moreau, C., Regnault, J-M., Deruelle, B. & Robineau, 1987. A new tectonic model for the Cameroon line, central Africa, *Tectonophysics*, **139**, 317-334.
- Morgan, P., 1982. Heat flow in rift zones, in *Continental and Oceanic Rifts*, ed. Palmason, G., *Geodynamics Series*, **8**, American Geophysical Union, Washington DC, Geological Society of America, Boulder, Colorado.
- Nolet, G., 1987. Seismic wave propagation and seismic tomography, in *Seismic Tomography with Applications in Global Seismology and Exploration Geophysics*, ed. Nolet, G., Reidel, Dordrecht.
- Nuttli, O. W., 1988. L_g magnitudes and yield estimates for underground Novaya Zemlya nuclear explosions, *Bull. seism. Soc. Am.*, **78**, 873-884.
- O'Connell, R. J. & Budianski, B., 1977. Viscoelastic properties of fluid-saturated cracked solids, *J. geophys. Res.*, **82**, 5719-5735.
- Raoof, M. & Nuttli, O. W., 1985. Attenuation of high-frequency earthquake waves in south America, *Pure appl. Geophys.*, **22**, 619-644.
- Singh, S. K. & Herrmann, R. B., 1983. Regionalization of crustal coda Q in the continental United States, *J. geophys. Res.*, **88**, 527-538.
- Snieder, R., 1987. Surface wave holography, in *Seismic Tomography with Applications in Global Seismology and Exploration Geophysics*, ed. Nolet, G., Reidel, Dordrecht.
- Suetsugu, D. & Nakanishi, I., 1985. Tomographic inversion and resolution for Rayleigh wave phase velocities in the Pacific Ocean, *J. Phys. Earth*, **33**, 345-368.
- Winkler, K. & Nur, A., 1979. Pore fluids and seismic attenuation in rocks, *Geophys. Res. Lett.*, **6**, 1-4.
- Xie, J. & Mitchell, B. J., 1988. Tomographic imaging of large scale lateral variations in L_g coda Q , *EOS Trans. Am. Geophys. Un.*, **69**, 1309.
- Xie, J. & Nuttli, O. W., 1988. Interpretation of high-frequency coda at large distances: stochastic modeling and method of inversion, *Geophys. J.*, **95**, 579-595.

Shear wave Q structure and its lateral variation in the crust of China and surrounding regions

Alemayehu L. Jemberie* and Brian J. Mitchell

Department of Earth and Atmospheric Sciences, Saint Louis University, 3507 Laclede Ave., St Louis 63103, MO, USA

Accepted 2003 October 29. Received 2003 February 24

SUMMARY

We have obtained three-layer crustal models of shear wave Q (Q_μ) for several surface wave paths in China and peripheral regions using a single-station, multimode method in which amplitude spectra of fundamental-mode and higher-mode Rayleigh waves, computed for known source depths and mechanisms, are compared to measured spectra. The three layers, totaling 60 km in thickness, roughly comprise the entire crust in the Tibetan plateau and include both the crust and part of the uppermost mantle in other regions where the crust is thinner. Q_μ in the shallowest layer, 10 km thick, is lowest (about 40) in the western portion of the Tibetan plateau and highest (about 250) in southeastern China. In the middle layer, at 10–30 km depth, Q_μ is lowest (60–80) beneath Tibet and the Pamir thrust system and highest (120–140) in central China and parts of the Sino-Korean platform. Uncertainties of Q_μ in the deepest layer, at 30–60 km depth, are much greater than in the upper two layers but available results suggest that Q_μ is lowest (about 80) under the Pamir thrust system and highest (about 180) under southern Mongolia. The densities of event and station coverage, although wanting in some regions, allow us to develop the first regionalized maps of crustal Q_μ variation for continents. The maps, for depth ranges 0–10 km and 10–30 km, generally show good agreement with Q results obtained earlier with other phases and good correlation with the tectonics of this active region.

Key words: multimode spectra, Rayleigh waves, shear wave Q .

INTRODUCTION

In recent decades surface wave dispersion has been used increasingly, on both global and continental scales, to develop tomographic maps of velocity variation. Eurasia has been well studied using these methods and maps of Rayleigh wave variation and shear wave variation at upper-mantle depths show patterns that generally correlate with surface tectonics and geological features (Trampert & Woodhouse 1995; Curtis *et al.* 1998; Ekström *et al.* 1997; Wu 1997; Ritzwoller & Levshin 1998; van Heijst & Woodhouse 1999).

Studies of surface wave attenuation variation have lagged behind those of velocity variation throughout the world because of well-known difficulties in making reliable amplitude measurements. Surface wave amplitudes may be contaminated by lateral refraction and consequent multipathing and focusing/defocusing. If, however, we are interested in studying lateral variations of seismic attenuation we are helped by the fact that lateral variations of attenuation and intrinsic Q in the crust, can be very large and thus easily observed even if the measurements are marked by relatively large errors (Mitchell 1995).

*Now at: CERL, University of Memphis, 3876 Central Ave., Memphis 38152, TN, USA.

It is important to study seismic wave attenuation because it is very sensitive to some geophysical and geological parameters that are not easily studied using seismic velocities. Some studies of seismic wave attenuation (e.g. Mitchell *et al.* 1997) have shown that seismic Q values in any region are strongly affected by the temporal history of tectonic or orogenic activity there. As such, Q values may be related to temperature and/or the presence of fluids in faults, fractures, and permeable crustal material and their variation with depth. For these reasons determinations of shear wave Q (Q_μ) at various depths in the crust should provide information on the tectonic history of the region of study.

Much of China and surrounding regions (Fig. 1) are characterized by a high level of tectonic activity due to the collision of India with the southern margin of Eurasia and to underthrusting of oceanic lithosphere along the eastern coast of Asia. It is complex in both its topography and geology. It is therefore important in surface wave studies there to minimize systematic errors due to lateral refraction of those waves and focusing/defocusing. To do that we use paths that are relatively short and that are restricted, as much as possible, to a single tectonic province. This means that, because surface waves attenuate slowly with distance, we will sacrifice precision of measurement to minimize systematic errors that we know can be large in amplitude measurements.

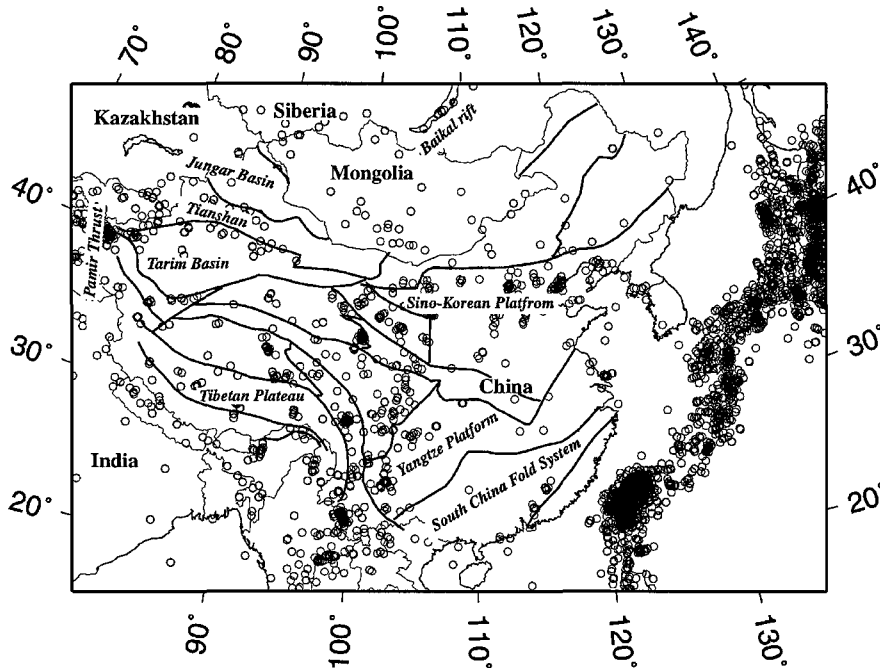


Figure 1. Map of China and surrounding regions showing major faults (Ren *et al.* 1987), major tectonic features and earthquake epicenters for events (circles) with magnitudes between 3.5 and 6.5 that occurred between 1970 and 1990.

We have obtained several models of Q_μ for three depth ranges in the crust of China and surrounding regions by fitting predicted spectral amplitudes of fundamental- and higher-mode Rayleigh waves to observed spectra. The method has been applied successfully in North America (Cheng & Mitchell 1981), the Barents shelf (Kijko & Mitchell 1983) and the Middle East (Cong & Mitchell 1998) but, in all cases, on a much more limited scale than the present study where our data covers a large portion of China and surrounding continental regions. Path coverage is relatively good in some regions but limited, or absent, in others. Using individual Q_μ models obtained in this study we are able, however, to develop the first contour maps of Q_μ variation over a broad region of the continental crust. Because we obtained reliable Q_μ values for two depth ranges between the surface and a depth of 30 km we can determine, in some cases, if Q_μ increases or decreases with depth. Although better coverage would be desirable in some regions the well-mapped areas provide new insights on Q_μ variation and its relation to tectonics in this portion of Asia.

REGIONAL TECTONIC SETTING

China and peripheral regions, like much of the rest of Eurasia, consist of several continental blocks that separated from Gondwanaland and drifted northward during the Palaeozoic era. The blocks slowly merged to become the geologically complex region that we have today (Metcalf 1990; Chung *et al.* 1998). Continental reconstructions show steady convergence of India and Eurasia since the late Cretaceous and collision in the Eocene. Tapponnier & Molnar (1977), using Landsat imagery, identified many important fault systems that are associated with regions of high historical seismicity through much of China and found that movement along east–west trending fault systems displace much of China eastward, a process that is key to much of the tectonics of the region. Seismic and ge-

ological evidence indicate that deformation from that convergence has occurred throughout a broad zone in Asia extending as much as 3000 km northeast of the Himalayas (Fig. 1) and that the crust has shortened by about 1500 km. Molnar & Tapponnier (1975) proposed that this was accomplished by:

- (i) Crustal shortening and underthrusting of India beneath the Himalayas and Tibet.
- (ii) Thrusting and crustal thickening in the Pamir, Tien Shan, Altai, Nan Shan, and other mountain belts.
- (iii) Movement of material out of the way of the two plates along major east–west strike slip faults.

The collision of India with the southern margin of Eurasia is thought to have caused progressive fracturing of the China plate which, in turn, led to Miocene-to-Recent volcanism in central and southeastern Asia. This is thought to have been superimposed on developing hot cell conditions caused by the insulating effect of the overlying lithosphere (Smith 1998).

This eastern portion of southern Asia is thus tectonically active and geologically complex. Because of this we expect that the intrinsic absorption of seismic energy through the crust there will be high (Mitchell 1975, 1995; Mitchell & Cong 1998). This is a distinct advantage for Q measurements because they are easier to make in regions where amplitudes decrease rapidly with distance and shorter paths can be used. We used relatively short paths for the measurements in order to minimize, as much as possible, systematic errors that might be caused by geological complexity of the region.

DATA

We collected a large number of vertical-component broad-band seismograms that recorded fundamental-mode and higher-mode

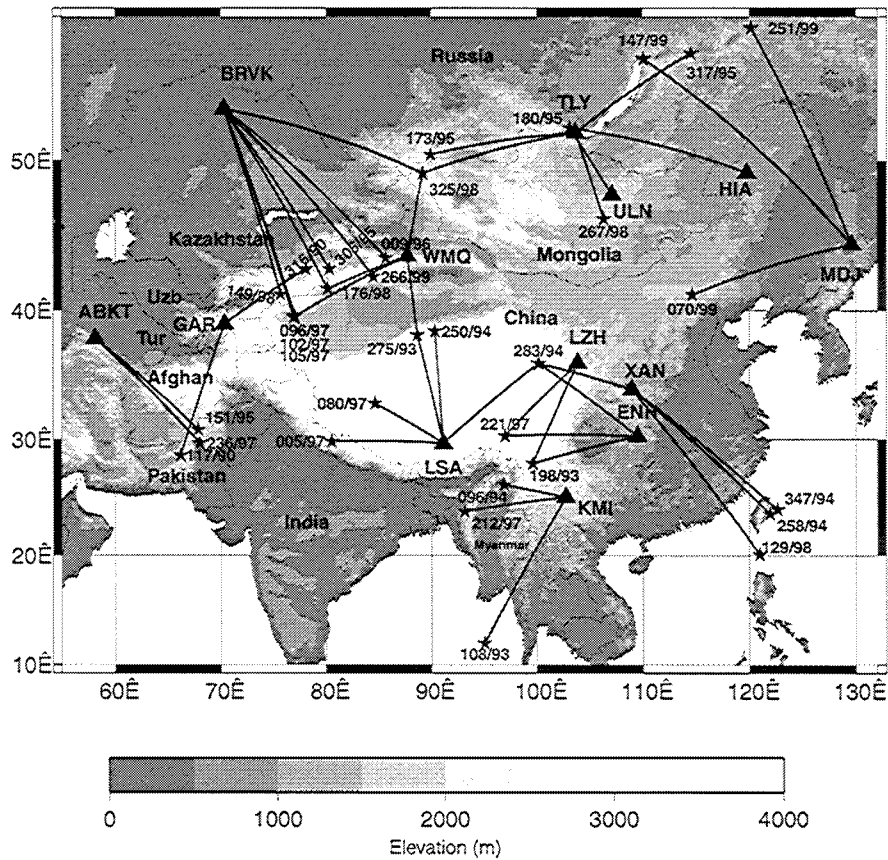


Figure 2. Map of event-station paths used in this study superposed on a topographic map of the region. Stars and triangles denote earthquakes and recording stations, respectively, and lines indicate the travel paths between them. Numbers near each epicenter give the Julian day and year of the event. The white field in the gray scale indicates all elevations greater than 3500 m.

Rayleigh wave energy between 1990 and 1999 in the eastern part of southern Asia. The data primarily pertains to China but some paths cross small regions of Mongolia, Siberia, Kazakhstan, Afghanistan and Pakistan (Fig. 2). We searched the NOAA PDE catalogue for events within specified magnitude, depth and epicentral distance ranges. All earthquakes occurred within, and peripheral to, the study area and were recorded by at least one of the digital stations in that region. We required that the earthquakes meet the following criteria:

- (i) Their m_b magnitude must be between 4.8 and 6.2. We found that events with magnitudes below 4.8 were too small to generate useful surface waves and that those above magnitude 6.2 generated records that were contaminated by effects of a complicated source-time function. Only one event in our final selection was above 5.9 in magnitude.
- (ii) They occurred at depths less than 50 km. Events in this depth range tend to produce large amplitudes for the fundamental Rayleigh mode whereas amplitudes for deeper events are suppressed.
- (iii) Distances between earthquakes and recording stations range between 300 km and 3000 km. By using records at relatively short distances we hope to minimize the degree of lateral complexity along the surface wave path. We avoid paths that are so short that waveforms do not have sufficient time to become well dispersed, as

well as paths that are so long that they will enhance the likelihood of multipathing and focusing/defocusing.

From the set of events that met these criteria we searched for waveforms with amplitude spectra that vary smoothly with period and group velocity dispersion curves that do not exhibit unrealistic abrupt offsets. We discarded data that did not meet these criteria taking such fluctuations and/or offsets to indicate that the data were contaminated by off-great-circle path arrivals and/or focusing/defocusing. Table 1 lists dates, origin times, magnitudes and hypocentral information for all events that were used in this study. The 33 events in the table produced 43 useable records. Fig. 3 shows recorded seismograms for three paths of this study. They lie predominantly in southern Tibet, eastern Kazakhstan, and near the border between Russia and Mongolia. Note that both fundamental and higher Rayleigh modes can be identified on all four records. The waveforms for the path throughout southern Tibet is marked by lower predominant frequencies than are the waveforms for the other paths. Later sections will show that southern Tibet has the lowest average Q_μ value of any part of our study area at depths between the surface and 30 km.

Observed spectra of the fundamental Rayleigh mode and the superposition of modes that comprise the higher-mode energy were obtained by applying the multiple-filter method (Dziewonski *et al.* 1969) to many vertical-component seismograms recorded by

Table 1. Dates, origin times, body wave magnitudes and hypocentral information for the earthquakes used in this study. ϕ , δ and λ denote, respectively, the strike, dip and rake of the fault plane, while EVLA is event latitude and EVLO is event longitude.

Day/Year	Date	Origin time	m_b	ϕ	δ	λ	EVLA	EVLO
117/90	1990 April 27	05:29:28.3	5.2	358	57	8	28.66	66.27
316/90	1990 November 12	12:28:49.0	5.9	211	65	23	42.94	78.08
108/93	1993 April 18	04:55:40.0	5.1	194	48	-143	11.96	94.97
198/93	1993 July 17	09:46:34.3	5.4	140	33	-55	28.00	99.64
275/93	1993 October 2	08:42:32.8	6.2	326	42	146	38.14	88.64
096/94	1994 April 6	07:03:27.7	5.6	96	57	26	26.19	96.84
250/94	1994 September 7	13:56:25.1	5.1	238	58	-6	38.42	90.19
258/94	1994 September 15	07:07:08.6	5.0	142	26	45	23.64	121.8
283/94	1994 October 10	14:07:57.1	5.0	327	45	109	36.04	100.2
347/94	1994 December 13	00:50:52.4	5.0	240	07	113	24.05	122.6
151/95	1995 May 31	13:51:20.5	5.3	74	05	-85	30.20	67.93
173/95	1995 June 22	01:01:21.7	5.5	97	34	97	50.33	89.92
180/95	1995 June 29	23:02:31.2	5.6	63	39	-44	51.92	103.1
305/95	1995 November 1	12:29:28.7	5.5	270	13	100	42.99	80.31
317/95	1995 November 13	08:43:14.7	5.9	56	43	-59	56.07	114.5
009/96	1996 January 9	06:27:54.4	5.2	108	23	118	43.70	85.65
005/97	1997 January 5	08:47:25.4	5.6	279	19	68	29.84	80.53
080/97	1997 March 21	21:04:48.6	4.9	35	26	-43	32.93	84.61
096/97	1997 April 6	04:36:35.2	5.6	253	43	-36	39.54	77.0
102/97	1997 April 12	21:09:08.9	5.2	243	48	-65	39.47	76.90
105/97	1997 April 15	18:19:10.1	5.4	170	66	-162	39.63	76.99
212/97	1997 July 31	15:59:37.0	5.5	330	16	40	23.89	93.16
221/97	1997 August 9	04:48:00.7	5.2	73	27	-90	30.29	96.98
236/97	1997 August 24	13:15:21.9	5.3	258	28	74	30.08	68.00
129/98	1998 May 9	02:16:14.4	5.0	160	32	63	20.09	121.0
149/98	1998 May 29	22:49:34.1	5.6	238	42	62	41.17	75.65
176/98	1998 June 25	06:39:20.3	5.2	262	27	129	41.55	80.14
267/98	1998 September 24	18:53:40.2	5.5	91	67	08	46.31	106.3
325/98	1998 November 21	16:59:48.0	5.2	136	18	80	49.23	89.19
070/99	1999 March 11	13:18:09.3	5.1	295	65	-9	41.13	114.7
147/99	1999 May 27	16:01:22.9	4.9	269	78	-7	55.81	110.0
251/99	1999 September 8	02:38:48.5	4.9	240	54	-162	57.43	120.2
266/99	1999 September 23	12:44:34.7	5.3	350	13	83	23.81	121.3

stations in our region of study. Fig. 4 shows a multiple-filter plot for the seismogram obtained for the path between event 305/95 and station BRVK in eastern Kazakhstan. It shows smoothly varying spectral amplitudes for the fundamental Rayleigh mode between periods of *ca* 7 s and *ca* 60 s and for the superposed higher modes at periods between *ca* 3 s and *ca* 8 s. For both the fundamental mode and the set of higher modes, the spectra and the group velocity curves vary smoothly over the period ranges of interest. In addition, those modes are well separated on the multiple filter plot.

There are cases, however, where higher-mode energy was not well recorded. This may have occurred because severe lateral changes in crustal structure disrupted the propagation of those modes as may have been the case in the eastern Tibetan plateau where four paths lack significant higher-mode energy. A short segment of oceanic path can also block higher-mode propagation: this may have occurred for an event in the Indian Ocean just off the continental shelf. In those cases, only the fundamental mode was used for determination of Q_μ models.

METHODOLOGY

The single-station method tries to match theoretical amplitude spectra to two sets of observed spectral amplitude data, one corresponding to the fundamental mode and the other to the super-

position of higher modes that arrives slightly earlier than all but the longest-period measurable fundamental-mode energy. The measured fundamental-mode spectra in this study range from *ca* 5–10 s to *ca* 40–60 s for the fundamental Rayleigh mode and between *ca* 3 s and *ca* 6–8 s for the higher modes.

One requirement for applying the multimode method is knowledge of the velocity structure in the area of interest. Shear wave velocity models for the region of study were obtained from the inversion of measured inter-station Rayleigh wave phase velocities obtained for paths between several pairs of stations (Jemberie & Mitchell 2001). Compressional wave velocities were obtained from the shear wave models assuming a Poisson's value of 0.25. For the determination of a Q_μ model for each single-station path we used the shear wave velocity model using two-station phase velocities that was most appropriate for that path. The only exception to this is Tibet where we used the published velocity model TP-4 of Chun & Yoshi (1977). Previous studies have shown that results are not greatly affected by the choice of velocity model unless the model differs greatly from the correct velocity structure.

Theoretical spectra were computed using the appropriate source parameters for the observed event, a velocity model pertaining to the region traversed by the surface wave path, and a first-guess Q_μ model. The theoretical fundamental-mode amplitude is, of course, computed using a single mode. We computed higher-mode

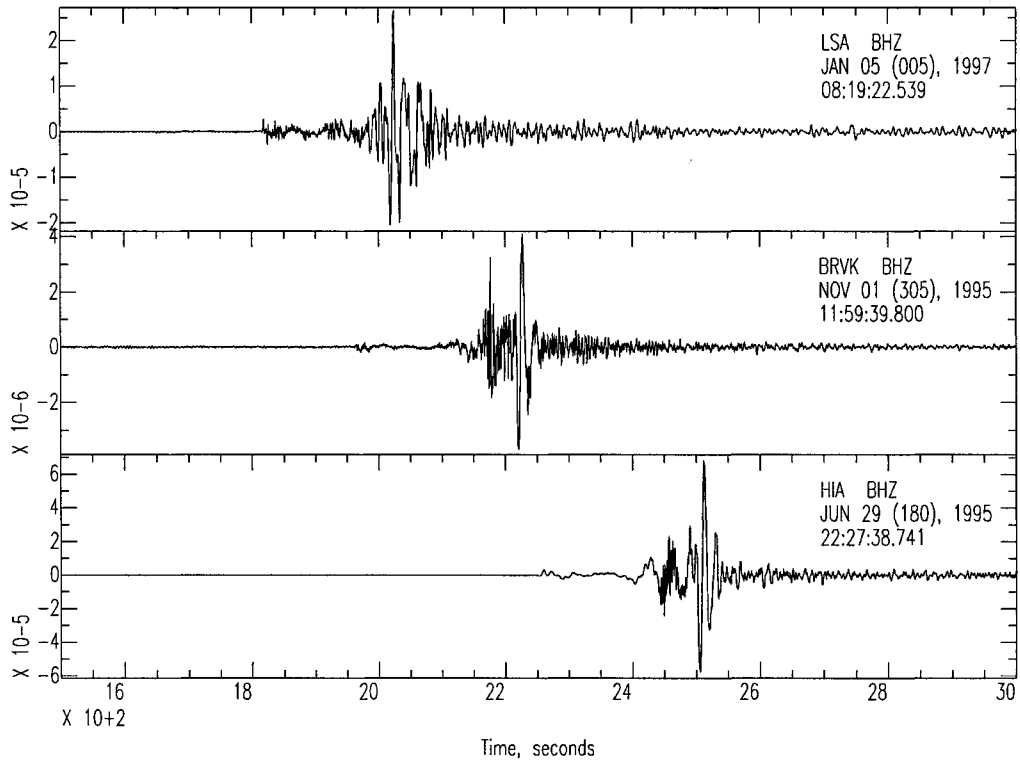


Figure 3. Example seismograms for three paths: top, from event 005/97 to station LSA in the southern Tibetan plateau; middle, from event 305/95 to station BRVK predominantly in Kazakhstan; and bottom, from event 180/95 to station HIA near the border between Russia and Mongolia.

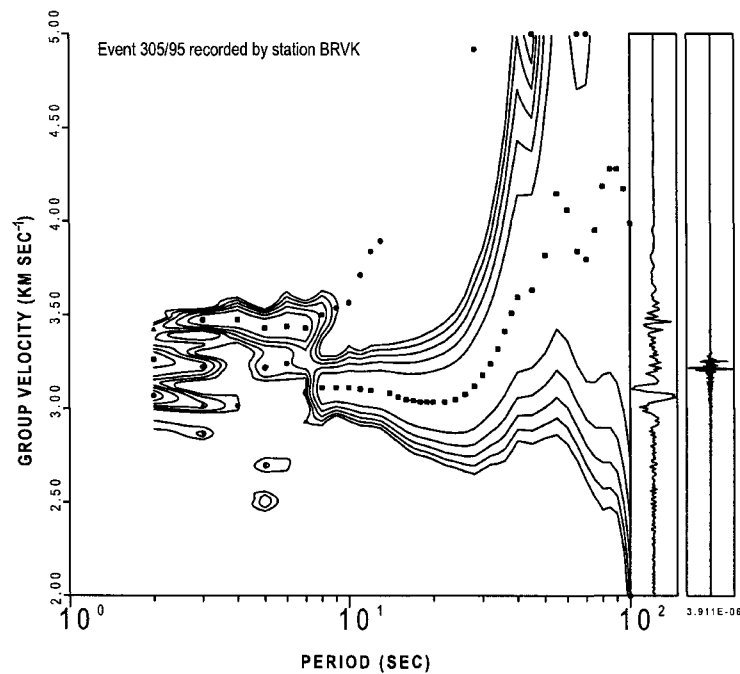


Figure 4. Multiple-filter plot for surface waves recorded on the vertical-component instrument at station BRVK from event 305/95 (middle seismogram of Fig. 2). Squares and circles denote the largest and second largest amplitudes recorded at any period, respectively. Contours show smoothly varying amplitudes and group velocities for the fundamental Rayleigh mode at periods between *ca* 8 and 60 s and for higher modes at periods between *ca* 3 and 10 s. The seismic trace furthest to the right shows the record of ground motion for this event on a linear time scale and the left trace shows the same ground motion plotted as a linear function of velocity to allow direct comparison with the multiple-filter plot.

Table 2. A comparison of depths (d) and seismic moments (M_0) reported by the USGS and Harvard with those obtained by fitting of multimode spectra in this study. * indicates that the depth of an event was taken from the ISCCD catalogue and + indicates that it was taken from the NOAA PDE catalogue.

Day/Year	USGS d (km)	HRV D (km)	This study d (km)	HRV M_0 ($\times 10^{20}$ dyn cm)	This study M_0 ($\times 10^{20}$ dyn cm)
117/90	33	15	15	22700	Same
316/90	05	15	19	329000	Same
108/93	23	17	23	6920	Same
198/93	27	15	15	13600	Same
275/93	16	15	16	164000	364000
096/94	33	15	15	71500	Same
250/94	33	33	33	7720	Same
258/94	53	37	37	7380	10380
283/94	33	33	06	4920	6900
347/94	33	25	36	10280	Same
151/95	33	15	24*	25300	Same
173/95	33	15	15	16700	Same
180/95	33	15	19	52000	89000
305/95	33	15	20+	8690	4000
317/95	24	21	24	55000	Same
009/96	33	33	33	13500	Same
005/97	33	15	15	24500	Same
080/97	33	15	15	11810	Same
096/97	33	15	15	105100	Same
102/97	20	16	20	10620	Same
105/97	23	23	23	65600	Same
212/97	33	42	08	9060	Same
221/97	33	33	17	7780	13670
236/97	33	23	23	33200	83200
129/98	33	15	33	5990	Same
149/98	19	32	19	10020	Same
176/98	33	15	15	5500	8500
267/98	33	33	33	24300	Same
325/98	10	15	10	7410	4410
070/99	33	15	23	5900	Same
147/99	10	15	33	5150	Same
251/99	10	20	10	5190	Same
266/99	33	33	27	8830	Same

spectra using 40 modes, a number we found to be more than adequate to compute realistic spectra for periods of 1 s and greater. The individual higher modes arrive at similar times on a seismogram and slightly earlier than most of the long-period fundamental-mode energy.

We tried to match theoretically predicted spectra for a particular path with observed spectra there. For the computed spectra we initially used moments reported by the Harvard CMT catalogues. In all but eight cases those moments led to theoretical spectra whose levels agreed with those of our observed spectra. In those cases we adjusted the moments to obtain theoretically-predicted spectral levels that agreed with our observed spectral levels. Moment adjustments are accomplished by using a single multiplicative factor to raise or lower the predicted levels of both the fundamental- and higher-mode spectra without changing their shapes. For this study the largest moment change was by a factor of about 2.5 (Table 2).

For source depths we initially used those obtained from the USGS PDE catalogue unless the earthquake depth was reported to be 33 km, a probable default depth. In that case we tried depths given by the Harvard CMT catalogue or catalogues of other agencies such as ISCCD, NOAA PDE or MHDF. For many events, focal depth determinations by the USGS and Harvard differed, sometimes sig-

nificantly. Such differences in focal depth determination are known to be common in catalogues of different reporting organizations. For any event, if there was a difference in reported source depth between the USGS and Harvard catalogues we first computed spectra using both depths. If one produced spectra that agreed with our observed spectra we used that depth. If neither the USGS nor Harvard focal depth generated spectra that were similar to our observed spectra we computed spectra at several depths and used the depth that produced the best agreement with observed spectra.

Determinations of source depth and Q_μ model are usually independent of one another. For shallow regional sources depths have a strong effect on the fundamental Rayleigh mode spectrum but have little effect on the higher modes (Tsai & Aki 1970). One common type of change is that a hole in the fundamental-mode spectrum will move to longer periods with increasing focal depth. For this reason we used only the level of the fundamental mode to determine depth. Source depth determinations are especially easy if a spectral hole is present. The effects of changes in focal depth are different from those caused by seismic moment changes, which increase or decrease all modes in equal proportion and do not depend on period as long as the corner period for the event being considered is smaller than the lowest period of interest.

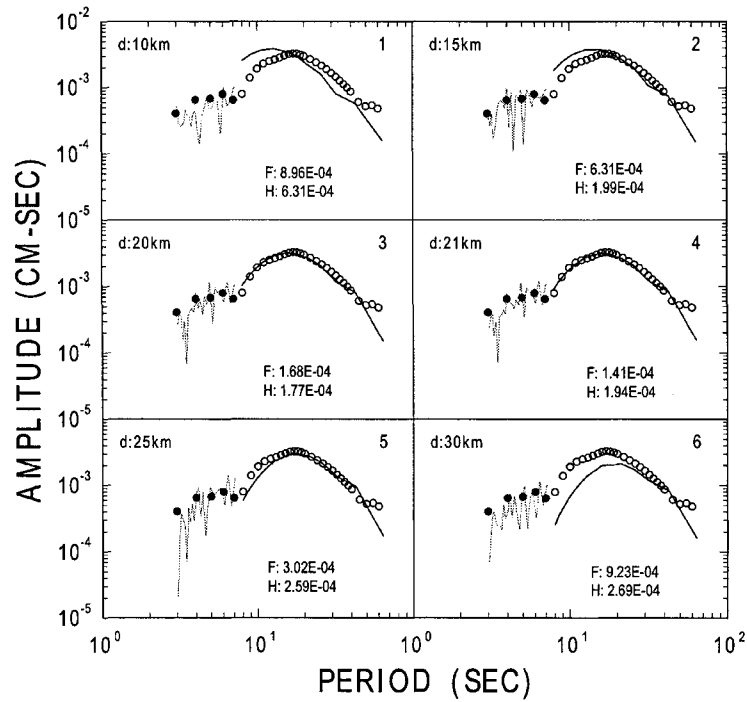


Figure 5. Comparison of theoretically predicted spectra (solid lines), for sources at six depths between 10 and 30 km, with observed fundamental-mode (open circles) and higher-mode (closed circles) spectra for event 305/95 recorded at station BRVK. The observed spectra were best fit by the theoretical spectra for the model in panel 4 of Fig. 7(b) and a source depth of 20 km. Numbers following the letters F and H give, respectively, the RMS misfits between theoretical and measured spectral amplitudes for the fundamental mode and for the higher modes, in cm s.

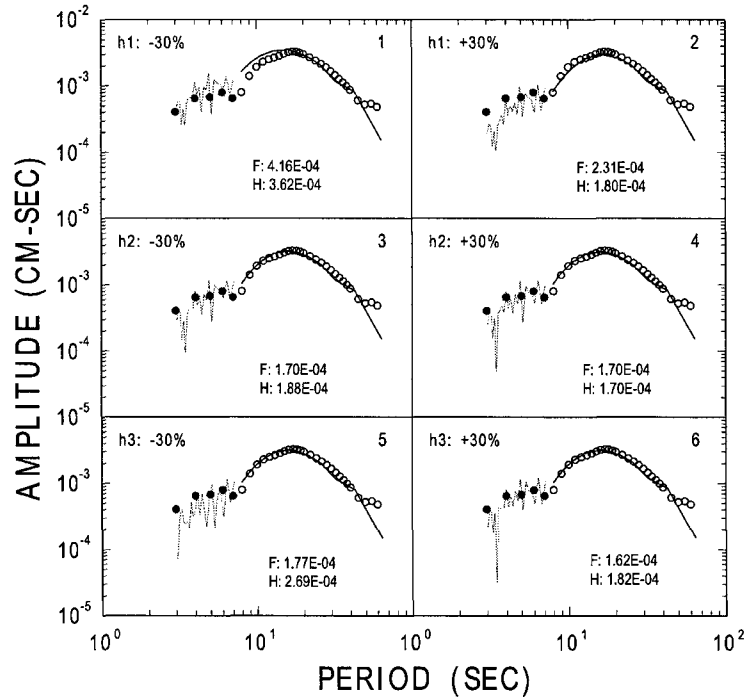


Figure 6. Comparison of theoretically-predicted spectra (solid lines), for models in which the thickness of each of the three crustal layers differs by ± 30 per cent from that for each layer of the model in panel 4 of Fig. 7(b), with observed spectra for event 305/95 recorded at station BRVK. Numbers following the letters F and H give, respectively, the RMS misfits between theoretical and measured spectral amplitudes for the fundamental mode and for the higher modes, in cm s.

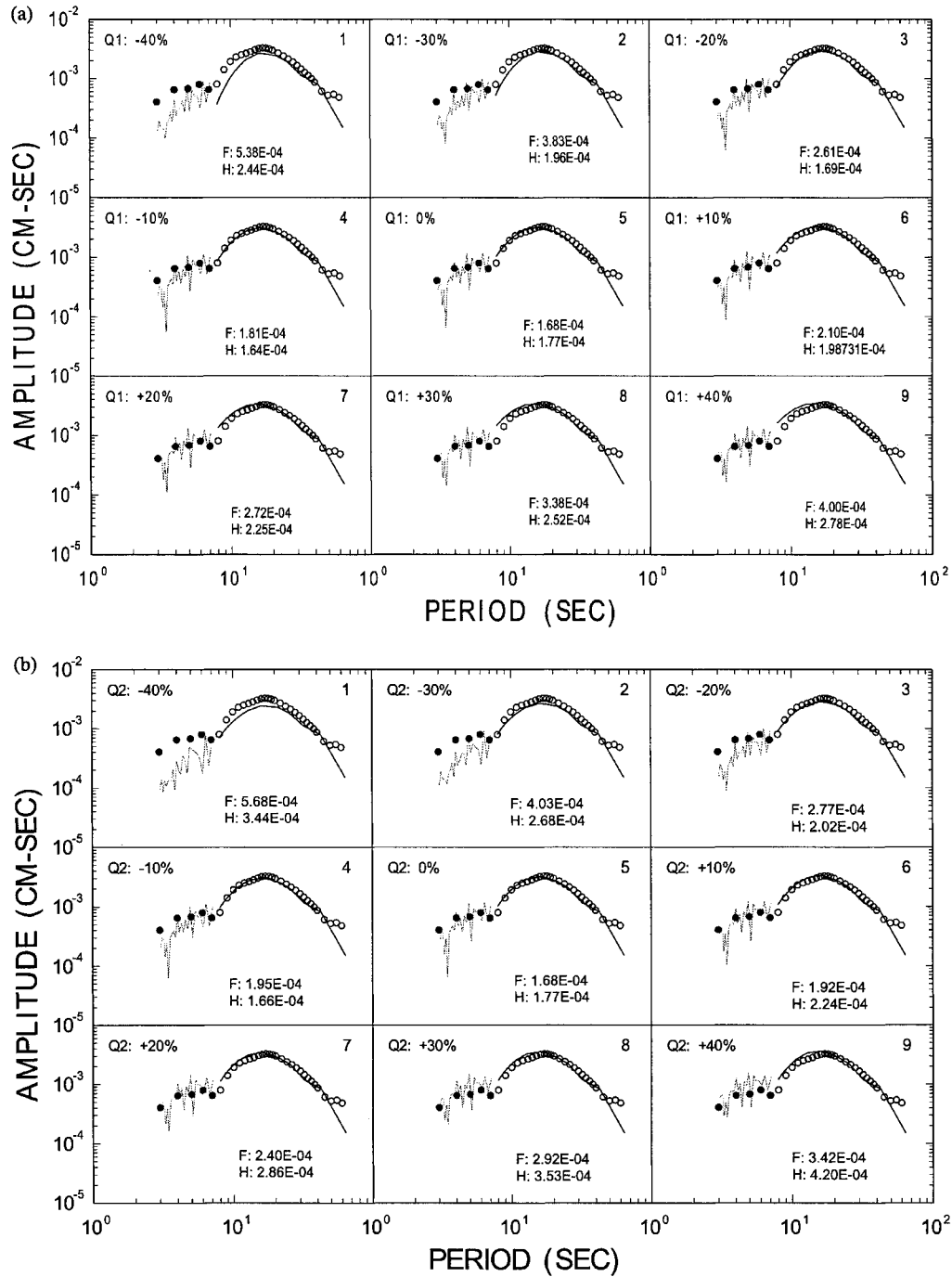


Figure 7. (a) Comparison of theoretically-predicted spectra (solid lines), for models in which Q_0 in layer 1 (0–10 km depth) varies from –40 per cent to +40 per cent from values in the model in panel 4 of Fig. 7(b), with observed spectra for event 305/95 recorded at station BRVK. Numbers following the letters F and H give, respectively, the RMS misfits between theoretical and measured spectral amplitudes for the fundamental mode and for the higher modes, in cm s. (b) Comparison of theoretically-predicted spectra (solid lines), for models in which Q_0 in layer 2 (10–30 km depth) varies from –40 per cent to +40 per cent from values in the model in panel 4 of Fig. 7(b), with observed spectra for event 305/95 recorded at station BRVK. Numbers following the letters F and H give, respectively, the RMS misfits between theoretical and measured spectral amplitudes for the fundamental mode and for the higher modes, in cm s. (c) Comparison of theoretically-predicted spectra (solid lines), for models in which Q_0 in layer 3 (30–60 km depth) varies from –40 per cent to +40 per cent from values in the model in panel 4 of Fig. 7(b), with observed spectra for event 305/95 recorded at station BRVK. Numbers following the letters F and H give, respectively, the RMS misfits between theoretical and measured spectral amplitudes for the fundamental mode and for the higher mode, in cm s.

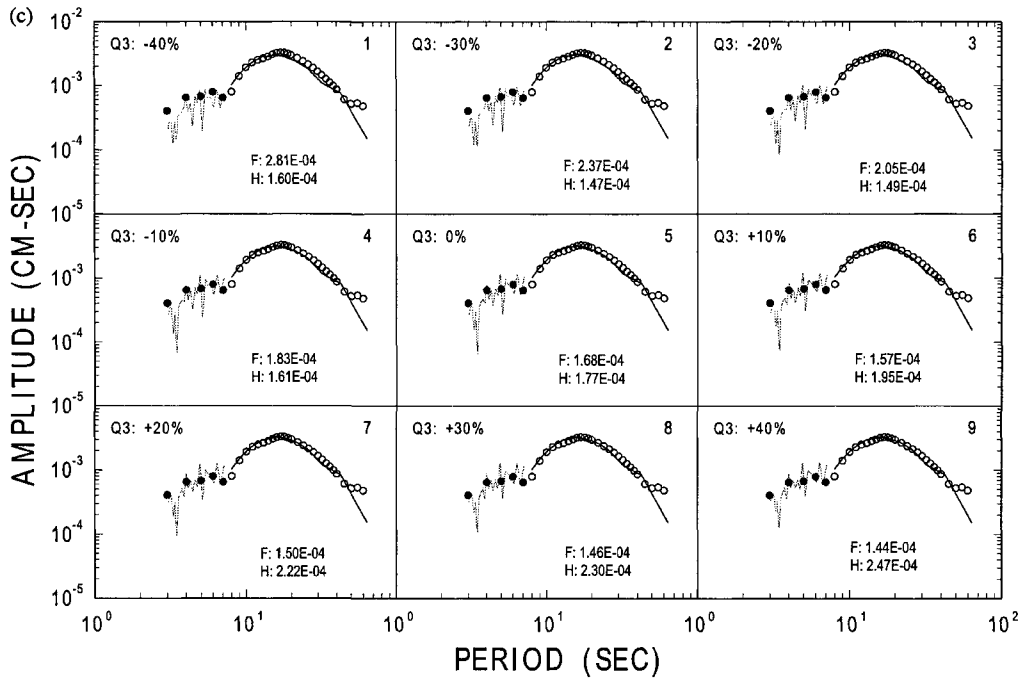


Figure 7. (Continued.)

Table 2 compares depths reported by the USGS, seismic moments reported by the Harvard CMT catalogue, and those that we obtained in the present study if using the USGS and Harvard values prevented good agreement between theoretical and observed spectra. For moment values used in this study, the word ‘same’ in Table 2 indicates that we used Harvard seismic moment values in our computations unless otherwise indicated.

After determining the best possible values for source depth and seismic moment for each event, we attempted to match observed and theoretical spectral amplitudes by systematically varying the Q_μ value of each layer. We started the process by assuming a constant Q_μ value for all three layers of the model and computed theoretical amplitude spectra for it. It was not necessary to consider the value of Q_μ in the half-space beneath the three crustal layers because it was found to have no effect on the computed spectra.

We then decreased or increased Q_μ in layer 1, depending on whether fundamental-mode theoretical spectral amplitudes are higher or lower, respectively, than observed amplitudes. Once we obtained a fit between fundamental-mode theoretical and observed spectral amplitudes at short periods, we varied the value of Q_μ for layer 2 until we obtained the best fit between theoretical and observed spectral amplitudes for both the fundamental and higher modes. If necessary, the same process was repeated for layer 3, but in many cases the sensitivity of the spectra to changes in Q_μ for that layer was too small to affect the spectra.

EFFECT OF SOURCE DEPTH, LAYER THICKNESS AND Q_μ ON COMPUTED SPECTRA

Variations in source depth have long been known to have a significantly greater effect on the spectral shape of fundamental-mode

Rayleigh waves than do other source parameters and they have a smaller effect on higher-mode spectra (Tsai & Aki 1970). This was also shown to be the case for earlier studies that employ multimode spectra (Cheng & Mitchell 1981; Kijko & Mitchell 1983; Cong & Mitchell 1998). Fig. 5 shows computed spectra for the focal depth and source parameters corresponding to event 305/95 as recorded at station BRVK for a path across eastern Kazakhstan. The spectra for a source depth of 20 km, the depth reported by the NOAA PDE catalogue (panel 3 of Fig. 5), provides a good fit to the observed spectra except for points at the longest periods of the fundamental mode where the signal/noise ratio is small. A change in source depth of 1 km (panel 4 of Fig. 5) has little effect on the spectra but effects caused by changes of 5 km are easily seen and those of 10 km are quite large.

Fig. 6 shows the effect that changes in layer thickness of 30 per cent have on the spectra. Using the same measured spectra as that in Fig. 4, the figures show that effects of a 30 per cent thickness change can only be seen for the uppermost layer (panels 1 and 2) and even there the change is relatively small.

Figs 7(a)–(c) show how values of Q_μ , varying between –40 and +40 per cent from the values in our chosen model affect the computed spectra for layers 1, 2, and 3. For the shallowest layer (0–10 km depth) Fig. 7(a) shows that for decreasing Q_μ differences in the computed spectra can start to be seen for a change of 20 per cent in Q_μ and are easily measurable for a change of 30 per cent. For increasing Q_μ clear differences do not occur until Q_μ becomes ca 30 per cent larger than that for our accepted model. These computations show that low values of Q_μ affect spectral amplitudes more severely than do high values of Q_μ . For layer 2, between depths of 10 and 30 km (Fig. 7b), the percentage-wise changes required for measurable changes in the spectra are about the same as those for layer 1. Similar computations for layer 3 (Fig. 7c), between depths of 30 and 60 km, show that changes in Q_μ have little effect on the

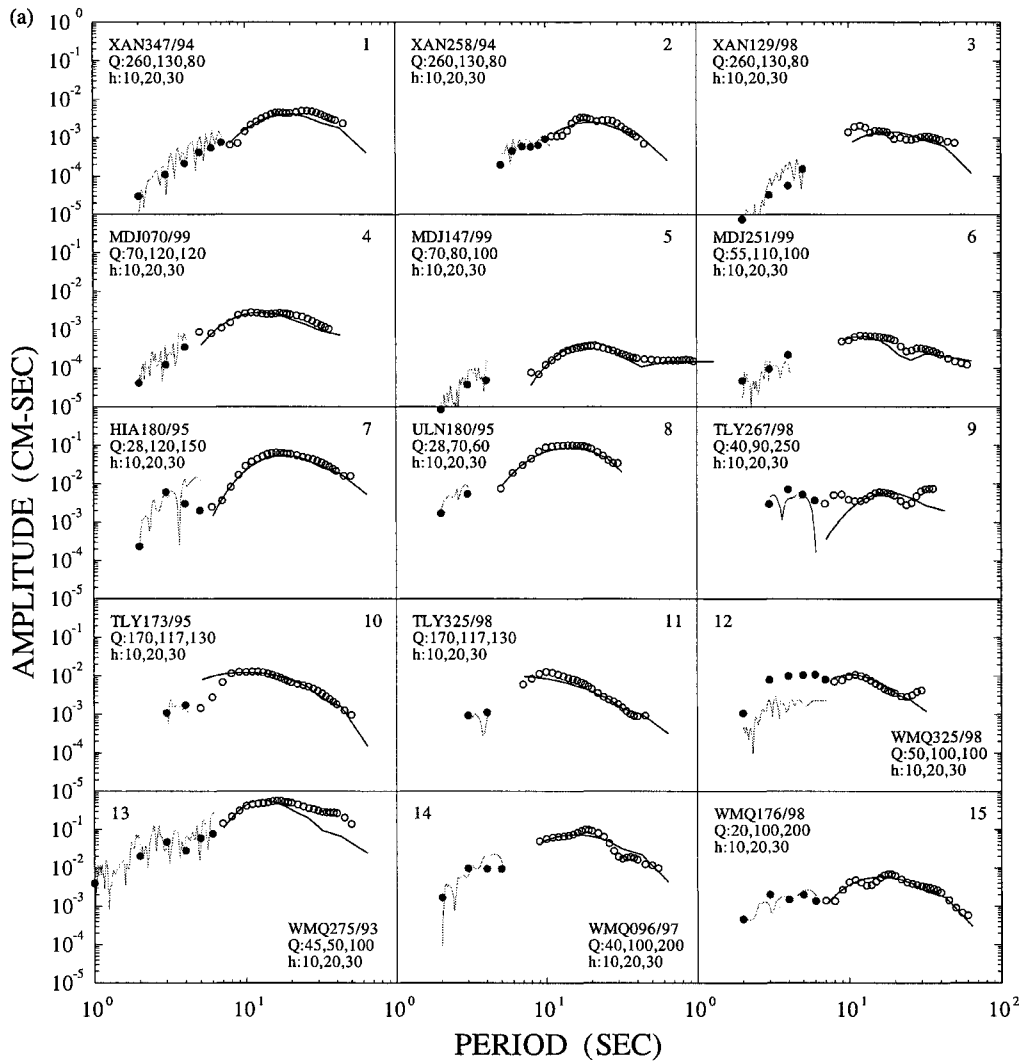


Figure 8. (a) Comparison of computed spectra (solid lines) predicted by the final models of this study with observed fundamental-mode and higher-mode amplitude spectra for paths from 13 events to stations XAN, MDJ, HIA, ULN, TLY and WMQ. Open and solid circles denote, respectively, fundamental mode and higher mode observed spectral amplitudes. (b) Comparison of computed spectra (solid lines) predicted by the final models of this study with observed fundamental-mode and higher-mode amplitude spectra for paths from 13 events to stations BRVK, GAR and ABKT. Open and solid circles denote, respectively, fundamental mode and higher mode observed spectral amplitudes. (c) Comparison of computed spectra (solid lines) predicted by the final models of this study with observed fundamental-mode and higher-mode amplitude spectra for paths from six events to stations LSA, ENH, XAN, KMI and TLY. Open and solid circles denote, respectively, fundamental mode and higher mode observed spectral amplitudes. (d) Comparison of computed spectra (solid lines) predicted by the final models of this study with observed fundamental-mode spectra for paths from five events to stations LSA, LZH and KMI. Open and solid circles denote, respectively, fundamental mode and higher mode observed spectral amplitudes.

computed spectra for the case where Q_μ is relatively high in layer 3. For paths where Q_μ in layer 3 is lower, that change can produce significant changes in the spectra. As indicated earlier, variations in the half-space of our models, at depths greater than 60 km, have no measurable effect on the spectral amplitudes over the period range of interest.

ERROR ESTIMATES FOR THE Q_μ MODELS

Following the expression derived by Anderson *et al.* (1965) for Rayleigh wave Q (Q_R), Cheng & Mitchell (1981) showed that the

logarithmic difference between theoretical, y_i , and observed, z_i , spectral amplitudes at period T_i can be expressed as

$$\ln(y_i) - \ln(z_i) = \frac{r\pi}{T_i} \sum_{i=1}^N \left\{ \frac{1}{2} \frac{\alpha_i}{C_i^2} \frac{\partial C_i}{\partial \alpha_i} + \frac{\beta_i}{C_i^2} \frac{\partial C_i}{\partial \beta_i} \right\} \Delta Q_{\beta_i}^{-1}, \quad (1)$$

where r is the epicentral distance, while α_i and β_i are shear wave and compressional wave velocities, respectively of layer 1. $\Delta Q_{\beta_i}^{-1}$ is an estimate of model uncertainties for $Q_{\beta_i}^{-1}$ at the indicated depth.

The above equation can be written in matrix form as

$$Ax = b, \quad (2)$$

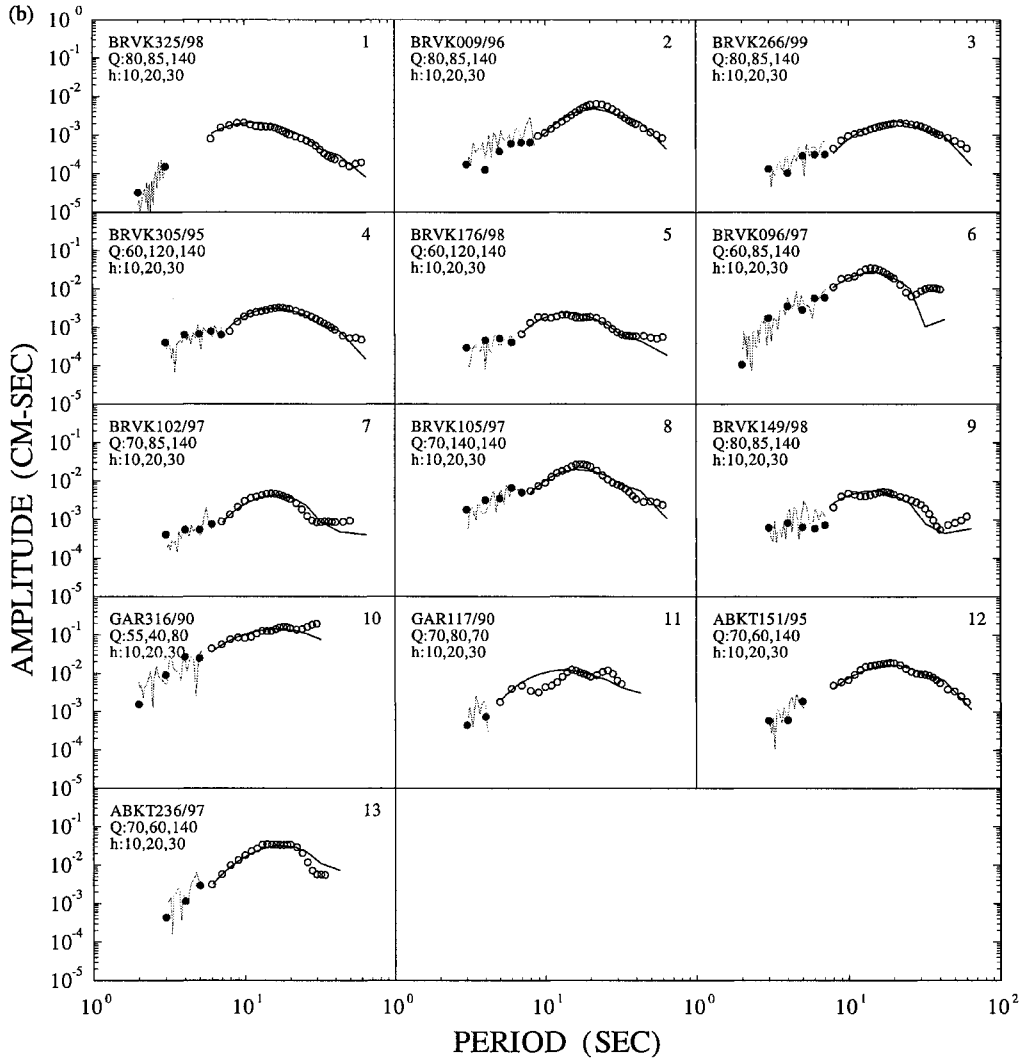


Figure 8. (Continued.)

where $x = (\Delta Q_{\beta 1}^{-1}, \Delta Q_{\beta 2}^{-1}, \dots, \Delta Q_{\beta N}^{-1})$,

$$b = \{[\ln(y_1) - \ln(z_1)], [\ln(y_2) - \ln(z_2)], \dots, [\ln(y_M) - \ln(z_M)]\}^T$$

and A is an $M \times N$ matrix of the elements

$$A_{il} = \frac{r\pi}{\tau_i} \left\{ \frac{1}{2} \frac{\alpha_l}{C_i^2} \frac{\partial C_i}{\partial \alpha_l} + \frac{\beta_l}{C_i^2} \frac{\partial C_i}{\partial \beta_l} \right\}, \quad (3)$$

for $i = 1, \dots, M$ and $l = 1, \dots, N$.

The least-squares solution of eq. (2) is

$$X = (A^T A)^{-1} A^T b = Hb. \quad (4)$$

For statistically independent data, the variance of the solution (x) is

$$V = \sigma^2 H H^T, \quad (5)$$

where σ^2 is the estimate of the variance of observations.

The mean-square value of the residuals $[\ln(y) - \ln(z)]$ for each layer, over all periods, is considered to be σ^2 . Therefore, the standard deviation of the solution is estimated as

$$\sigma_{\text{sol}} = \pm \sqrt{V}. \quad (6)$$

Using (6), σ_{sol} is computed for each of the three layers for selected paths in southeastern Asia. The Q_{μ}^{-1} structure plots with standard deviations are shown in Figs 8(a)–(d).

SPECTRA AND MODELS

This section discusses our measured spectra and the Q_{μ} structure obtained from them for selected subregions of our study area. We tried to obtain as many sets of useable spectral data as possible using paths that were short enough to minimize effects of lateral crustal complexities. There are, however, only a few regions where multiple paths allow us to estimate the consistency of our results. Uneven station and event coverage leave some regions with only sparse coverage and some large gaps between paths. The largest gap occurs in a portion of northern China and southern Mongolia but additional smaller gaps lie in northeastern China, northwestern India and northern Pakistan. Another factor contributing to sparseness of useable data in some regions is the geological complexity of southeastern Asia, which makes it difficult in many regions to

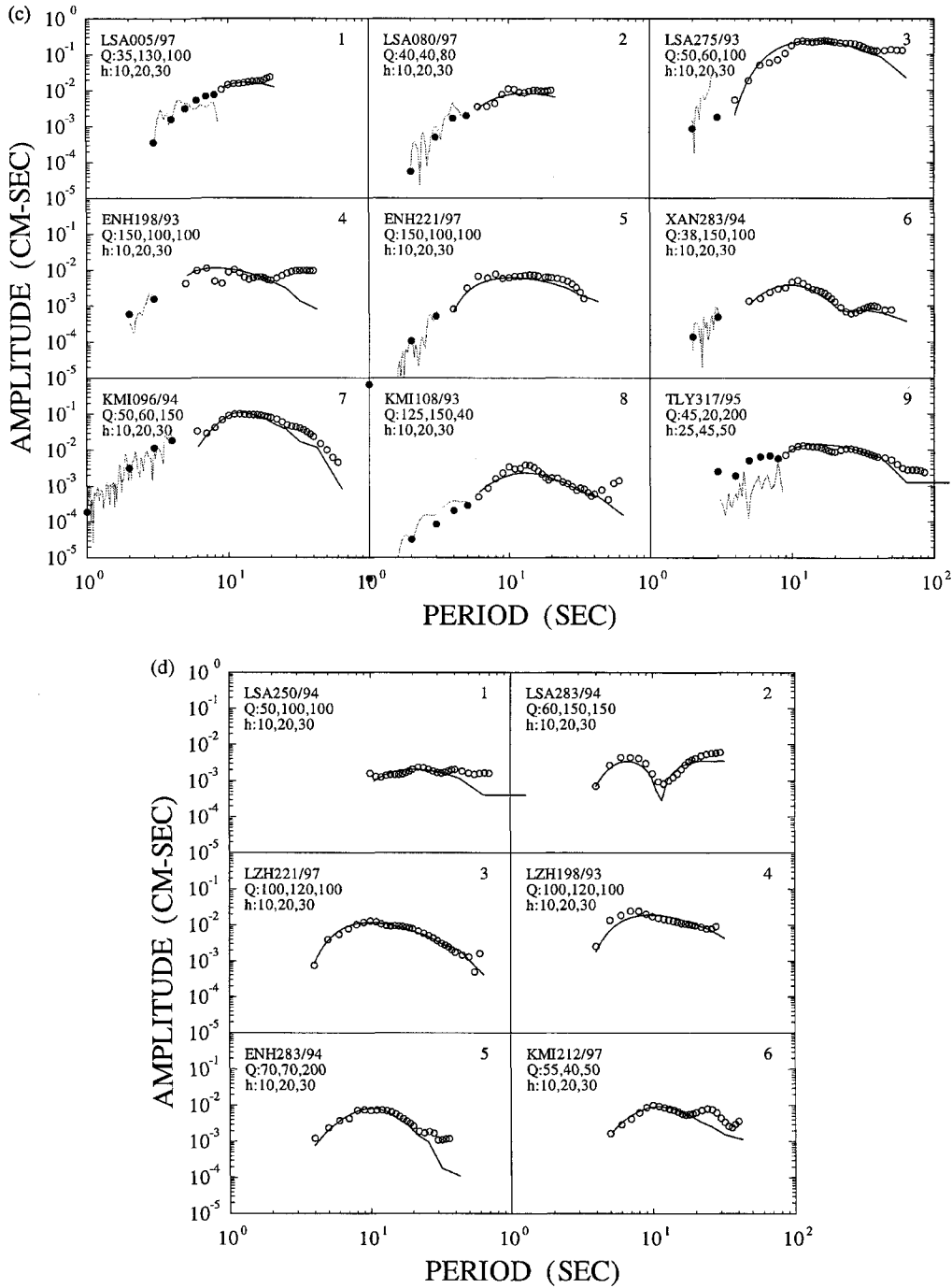


Figure 8. (Continued.)

find seismic recordings that are free from effects of scattering and multipathing that might adversely affect spectral amplitudes. One possible way to fill in gaps might be to assume that Q_{μ} varies in a systematic way that is related to the past tectonic history of a region (Mitchell & Cong 1998).

We computed theoretical spectra for a Q_{μ} structure consisting of three layers that increase in thickness with increasing depth: layer 1 is 10 km thick, layer 2 is 20 km thick and layer 3 is 30 km thick.

These overlie a uniform half-space that roughly corresponds to the upper mantle in the Tibetan plateau. In other regions, where the crust is thinner, the upper two layers form a better approximation to the crust and the third layer contains part of the uppermost mantle. As noted earlier the half-space has virtually no effect on any of the computed spectra.

The following paragraphs discuss our results for five regions where we can compare the models obtained from observed

spectra along two or more paths. We obtained a three-layer Q_μ model, along with an error estimate for Q_μ in each layer, for selected paths.

Station XAN recorded three events just off the continental shelf near Taiwan. The travel paths were to the northwest across southeastern China. Their spectra appear in panels 1, 2 and 3 of Fig. 8(a) and models derived from those spectra appear in Fig. 9(a) (XAN129/98, XAN258/94 and XAN347/94). The models are all very similar with Q_μ^{-1} being about 0.0035 in layer 1, and increasing to 0.0075 in layer 2 and 0.013 in layer 3. The value in layer 1 corresponds to the highest value of Q_μ anywhere in our region or study for that layer. All models indicate that Q_μ decreases with depth.

Within the Tibetan plateau, station LSA recorded five events for which the backazimuth to the station varies from west to northeast. We obtained both fundamental-mode and higher-mode spectra at three stations (Fig. 8b) and fundamental-mode spectra for two stations (Fig. 8d). Station LZH also recorded two events with paths in a southwest–northeast direction across the eastern part of the plateau. Fundamental-mode spectra for those paths appear in Fig. 8(d). At depths greater than 10 km, Q_μ^{-1} , for all but one of these paths, lies between 0.007 and 0.10, and error bars are relatively large (Fig. 9a). For shallower depths Q_μ varies between about 0.01 and 0.28, and some of the error bars are small enough to suggest that there really is a large variation in Q_μ for this region.

Nine paths cross eastern Kazakhstan to station BRVK from events ranging in azimuth between SSE and ESE to that station from events in northwestern China (Fig. 8c). Models obtained from three of those spectra (Fig. 9b) show that Q_μ^{-1} in the uppermost layer varies over the small range 0.013 to 0.017 with lower, but more widely varying values (higher Q_μ) in the deeper layers. This increase of Q_μ with depth differs from the result in southeastern China where Q_μ decreases with depth. Fig. 8b shows two spectra plots for paths across Afghanistan to station ABKT in Turkistan. The models determined for those paths (Fig. 9b) exhibit nearly identical Q_μ values at all depths, being 0.014 in layer 1, 0.017 in layer 2 and 0.007 in layer 3. The nearby path between event 316/90 and station GAR lies along the Pamir thrust and exhibits very low Q_μ , especially in layer 2 where Q_μ^{-1} is about 0.025 ($Q_\mu = 40$).

Station TLY recorded surface waves from two events with similar west–east paths that lie near the Russian–Mongolian border (Fig. 8a). Q_μ^{-1} obtained from multimode spectra for two event-station pair 173/95 and TLY325/98 both exhibit little variation with depth having a value of *ca* 0.006 in the uppermost layer and, between 0.007 and 0.009 at depths greater than 10 km (Fig. 9c).

Station MDJ recorded surface waves generated by three events at azimuths ranging between WSW and NNW (Fig. 8a). The southernmost path was restricted to China and the two more northerly paths traversed a portion of Russia and northeastern China. Fig. 9(c) shows that little difference exists between the three models that we obtained at depths greater than 10 km where values range between 0.008 and 0.012. The upper 10 km shows variations between 0.014 and 0.018 with the smaller values having much smaller error bars than the largest value. Taking the error bars into account, all paths in this region could be explained by the same model. Energy from two paths in Myanmar was recorded by station KMI in southern China. Models obtained for these paths (Fig. 9c) are quite dissimilar but the errors bars for one of the models are very large. Spectra for two paths from a westerly direction to station TLY (Fig. 8a) lead to virtually identical models (Fig. 9c) where Q_μ^{-1} does not differ greatly from 0.007 at any depth.

These comparisons show that there is substantial consistency between models that are obtained for similar paths and that when large

differences occur they do so when one or more models in the group are characterized by large standard error estimates. A perusal of individual models indicates that Q_μ in the upper 10 km of the crust in China shows a decrease from east to west and that Q_μ in western China and Mongolia increases from south to north. For depths between 10 and 30 km paths across the western portion of the Tibetan plateau appear to exhibit lower Q_μ values than do paths in the eastern part of the plateau and values in the eastern part of the plateau seem to be similar to values available from paths further east in China.

Other sets of spectra that are of interest are those for paths that traverse portions of the Baikal rift. Spectra for event-station pairs 267/98 to TLY, 180/95 to HIA, and 180/95 to ULN (Fig. 8a), with short path segments through the rift, can all be explained by models in which Q_μ^{-1} varies between 0.025 and 0.036. These values indicate that Q_μ is very low (between 28 and 40) in the upper part of the crust (Fig. 9d) in the Baikal rift region. Observed spectra for one path (317/95 to TLY) that travels lengthwise through a larger portion of the rift, could not be matched with theoretical spectra. We interpret this to mean that the lateral complexity of the Baikal rift prevents interpretation of this path in terms of a plane-layer model.

MAPS OF Q_μ VARIATION FOR DEPTHS BETWEEN 0 AND 30 km

The previous section described Q_μ values for crustal layers at depths between 0 and 10 km, and between 10 and 30 km, depth in China and some peripheral regions. Although there are relatively large measurement errors for many paths, there is enough consistency within similar regions to suggest that it be worthwhile to construct contour maps of Q_μ variation for those two layers. This should give a better picture of Q_μ variation, based upon all available paths, than can be gleaned from models of individual paths.

Figs 10(a) and (b) show Q_μ contour maps for the layer at depths between 0 and 10 km, and for the layer between depths of 10 and 30 km. Lack of sensitivity to Q_μ changes in many areas prevented us from constructing a contour map for layer 3 at depths between 30 and 60 km. Where path coverage is poor, such as in northcentral China, parts of Mongolia, and the Tarim basin (Fig. 2) interpolated values of Q_μ are used to fill in those regions. Dashed lines on the maps indicate regions that required significant interpolation. Q_μ values in those regions must be considered to be preliminary estimates that may change as more data become available.

Layer 1

Fig. 10(a) indicates that Q_μ is highest (about 250) in the south China block and is relatively high in western Mongolia (up to about 160). Q_μ is lowest in the western portion of the Tibetan plateau and near the Baikal rift (40–60). The low values in Tibet extend as far north as the Tarim Basin. Other regions where Q_μ is low include eastern Mongolia (40–60), Burma (about 60), the Jungar basin and the Tianshan fold system (60–90), and eastern Kazakhstan (70–90). There is a steep positive gradient of Q_μ as we go from the eastern part of the Tibetan plateau to the south China block. This may correspond to a rapid decrease in crustal thickness with distance between the plateau and the lowlands of southeastern China.

Layer 2

Fig. 10(b) indicates that relatively high Q_μ values (120–140) characterize most of central and eastern China and much of Mongolia. Lowest Q_μ values for this layer lie beneath the Tibetan plateau and

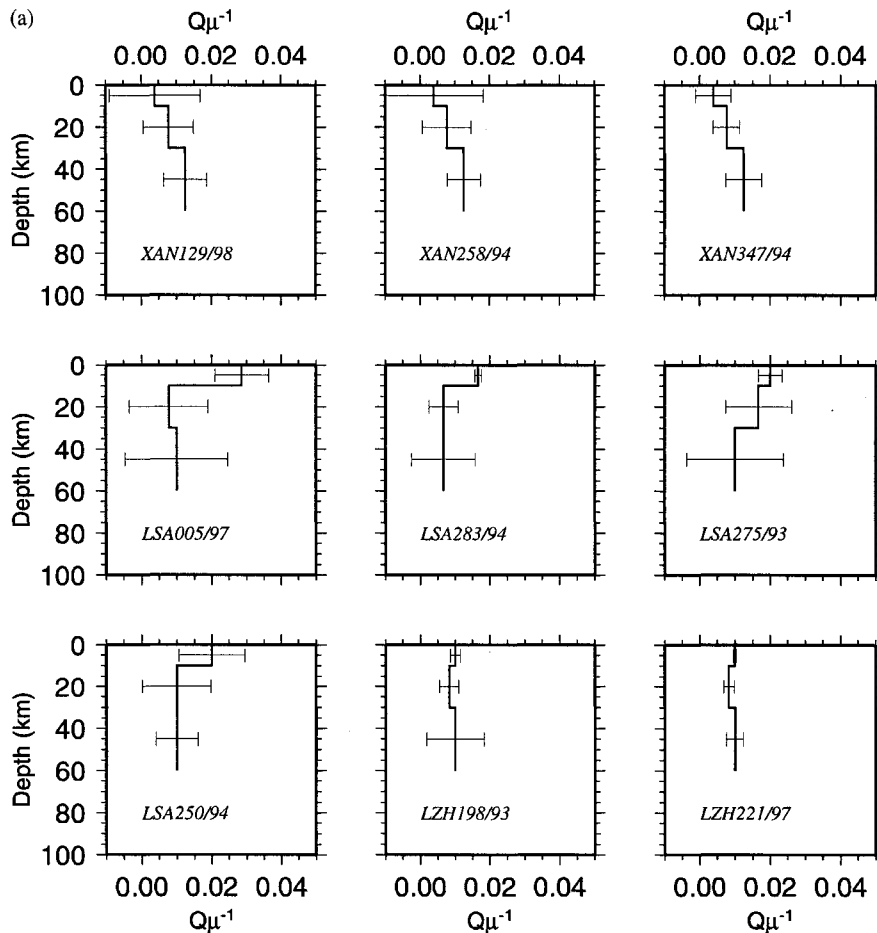


Figure 9. (a) Three-layer Q_{μ}^{-1} models with standard errors obtained for three paths across southeastern China (to station XAN) and for six paths across the Tibetan plateau (to stations LSA and LZH). (b) Three-layer Q_{μ}^{-1} models with standard errors obtained for four paths in Kazakhstan (to station BRVK), two paths across Turkistan and Afghanistan (to station ABKT), and a path along the Pamir thrust (to station GAR). (c) Three-layer Q_{μ}^{-1} models with standard errors obtained for three paths in northeastern China and Russia (to station MDJ), two paths in central China (to station ENH), two paths in Myanmar and southern China (to station KMI), and two paths along the Mongolia–Russia border (to station TLY). (d) Three-layer Q_{μ}^{-1} models with standard errors obtained for three paths that traverse portions of the Baikal rift (to stations HIA, ULN and TLY).

near the Pamir thrust (50–60). The low values beneath the Tibetan plateau in this layer, combined with the low values that also characterize layer 1, give this region the lowest average Q_{μ} anywhere in this southeastern part of Asia. Low values also lie in and around the Baikal rift (50–80) and in Burma (60–100). Q_{μ} values in eastern Kazakhstan range between 70 and 90, and those beneath the Tarim basin between about 90 and 100. The low Q_{μ} values centered near the Pamir thrust belt extend into Afghanistan and Pakistan where they range between 80 and 90.

DISCUSSION

We have determined Q_{μ} primarily in two depth ranges throughout much of China and surrounding regions. Determinations for individual paths show that large variations of Q_{μ} occur for the depth ranges 0–10 km and 10–30 km. In some regions path coverage is dense enough to allow us to construct accurate contours of Q_{μ} variation, but interpolation is required to fill out the map. This marks the

first time that Q_{μ} has been mapped for crustal depths over a broad region of continental crust and results show that Q_{μ} can vary quite rapidly from region to region.

Values of Q_{μ} , at all depths, are lower than those found for most stable continental regions, a result that is consistent with results of numerous previous studies (e.g. Mitchell 1975, 1995). The low Q_{μ} values closely correspond to the broad tectonically active Tethysides belt (Sengör 1987). This correlation provides additional support for the idea that tectonically active regions are characterized by high rates of seismic wave attenuation (e.g. Mitchell 1995). Although all values are low, there is a wide variation in values at all depths that were studied and also in the rate of increase or decrease of Q_{μ} with depth.

The lowest average Q_{μ} values throughout our region of study occur in the Tibetan plateau (Figs 10a and b). These especially low values lie in a region generally coincident with low values of L_g coda Q found there (Mitchell *et al.* 1997) and a recently discovered region of very low values of $L_g Q$ (Xie 2002). This low- Q region has a relatively low level of seismicity differing from most other

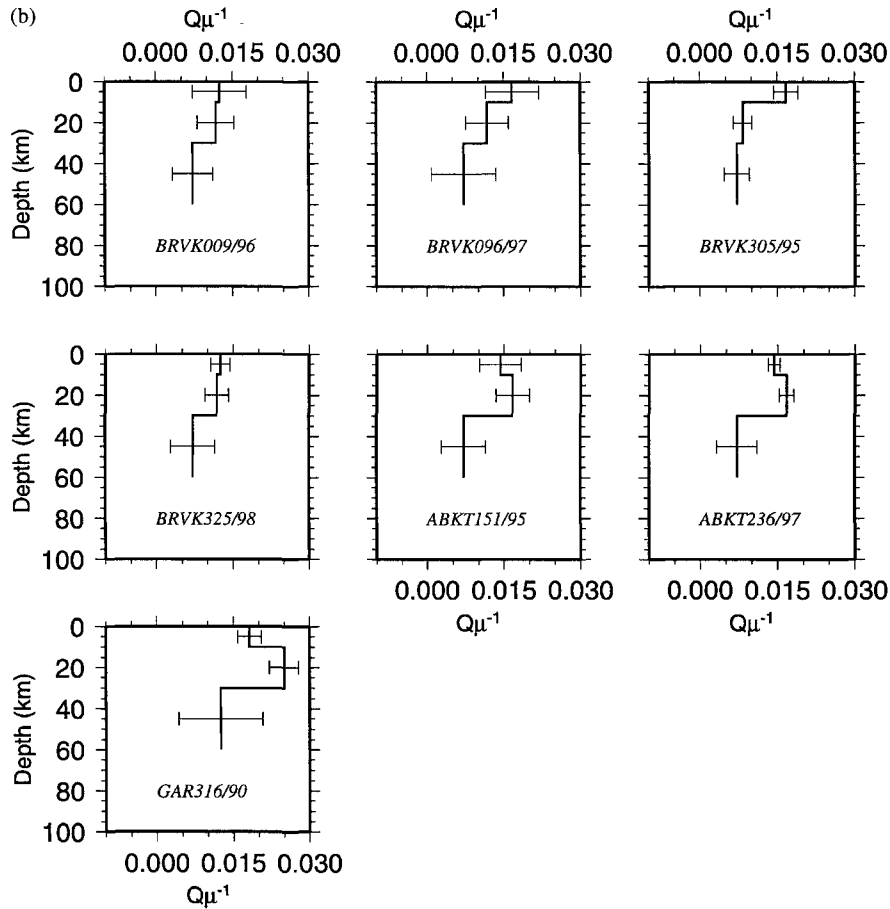


Figure 9. (Continued.)

regions with low- Q crustal rock where seismicity is high. This may occur because low- Q values in the Tibetan plateau are caused by high temperatures and a partially molten middle crust in that region (Nelson *et al.* 1996). Whereas low Q_μ values in most crustal regions may be due to the need for waves to squeeze fluids through faulted and permeable rock where temperatures may be only moderately high, the very hot and partially molten crust in southern Tibet may not be brittle enough to sustain a high level of seismicity.

Our values of Q_μ , obtained from the inversion of Rayleigh wave attenuation at periods between *ca* 3 and 60 s, are lower than those found for Lg Q or Lg coda Q , which were measured for 1 s waves. If $Q_\mu = Q_o \omega^\zeta$ this difference is consistent with values for the frequency dependence parameter (ζ) of Q_μ being between 0.3 and 0.8. This range is similar to that found for this region of Eurasia from studies of Lg coda Q at 1 Hz (Mitchell *et al.* 1997). In a study of Q at higher frequencies (8–12 Hz) Sarker & Abers (1999) find even higher values of Q for paths in Kazakhstan, a result indicating that Q_μ continues to increase with frequency between surface wave frequencies (*ca* 0.02–0.2 Hz) and at least 10 Hz.

Some features of the patterns of Q_μ variation, especially in the uppermost layer (0–10 km depth) correlate well with tectonic features in the region of study. A comparison of Q_μ variations shown by Fig. 10a with earthquake activity (Fig. 1) indicates that the higher values of Q_μ all occur in a broad region of eastern China where earthquake activity is lowest, while lower values of Q_μ are associ-

ated with higher levels of earthquake activity in western and northern China and adjacent regions. The band of rapid lateral change centered near the $Q_\mu = 100$ contour roughly separates relatively stable crust from the more active crust to the north and west.

The broad north–south trending zone of low Q_μ values whose width extends about 1000 km eastward from a longitude just west of the Baikal rift coincides with high heat flow values, while higher Q_μ values in western Mongolia coincide with low heat flow (Khutorskoy & Yarmoluk 1989). Q_μ values in northeastern China, between Mongolia and the northern Yangtse platform range between *ca* 60 and 120, a northeast–southwest trending band that roughly coincides with a region of extruded Cenozoic basalts (Menzies & Xu 1998).

The Q_μ values in southeastern China (100–130) in layer 2 are lower than those in layer 1 (200–250). The decrease in Q_μ value with increasing depth may be related to a shallow asthenosphere that has been interpreted to extend to the base of the crust because of the absence or weak presence of lithospheric mantle (Wier 1982).

The large lateral variations in Q_μ found in this study suggest that determinations of earthquake magnitudes and explosion yields obtained from regional phases could be erroneous if varying rates of attenuation for different paths are not taken into account. In addition, variations in the distributions of Q_μ with depth observed in this study could diminish our ability to discriminate between earthquakes and explosions using ratios of two regional phases that travel predominantly at different depths. If those phases sample different

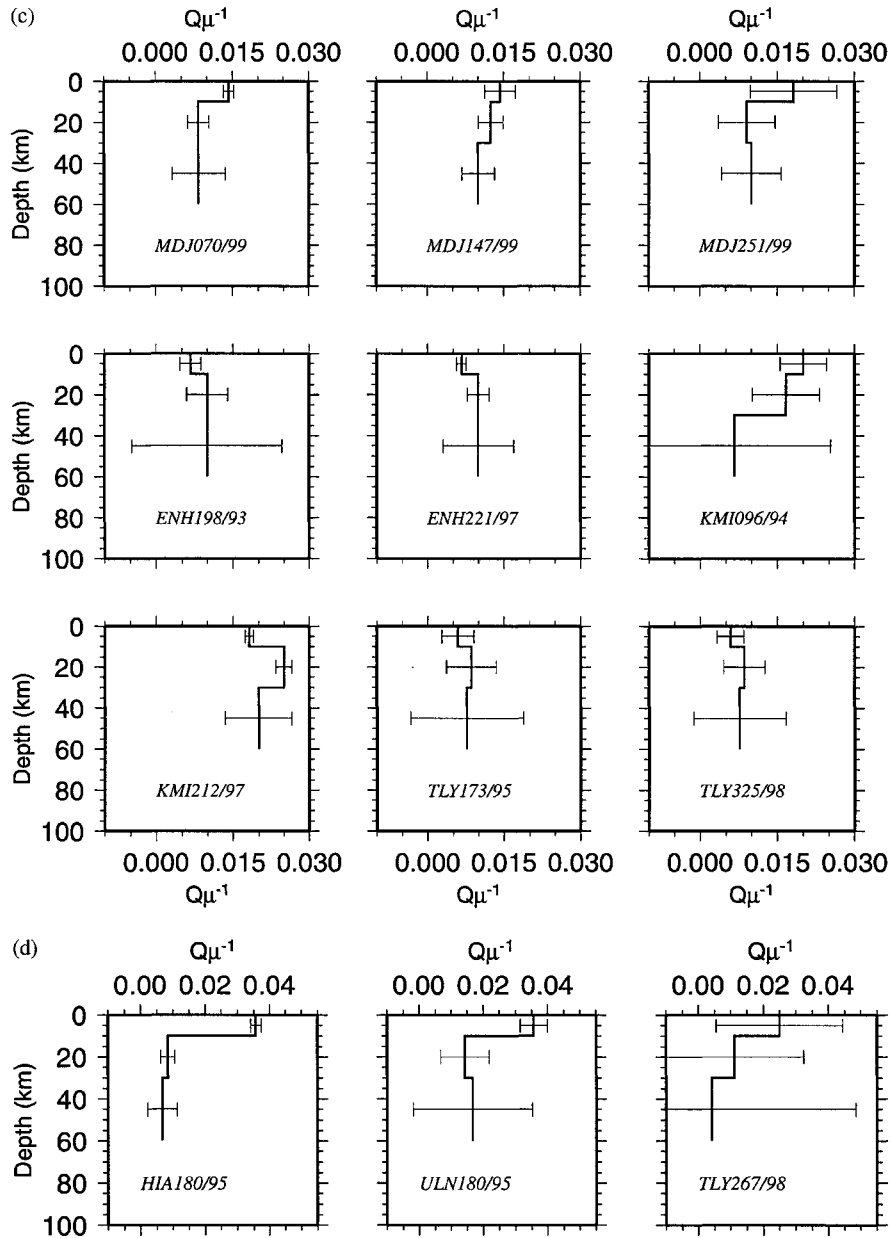


Figure 9. (Continued.)

portions of the crust and upper mantle, a transportable discriminant would require that corrections be made for the different rates of wave attenuation at different depths.

CONCLUSIONS

A single-station method has been used to obtain three-layer models of Q_μ throughout southeastern Asia by matching theoretically predicted amplitude spectra for fundamental- and higher-mode Rayleigh waves. The models indicate that Q_μ exhibits large lateral variations, at least to depths of 30 km.

Q_μ for the uppermost layer (0–10 km) indicates that highest values (as high as 250) occur in southeastern China where earthquake

activity is lowest. Relatively high values (about 160) lie in north-western Mongolia and a southern portion of the Siberian craton. Low values characterize much of the Tibetan plateau, especially the western portion, and the northcentral China fold systems that are tectonically active. Moderately low values (about 70) mark the crust beneath Kazakhstan, Afghanistan and Pakistan. The Q_μ map for the deeper layer (10–30 km) shows that highest values (about 120–140) lie across a broad region of central China and the Sino-Korean platform. The lowest values lie beneath western Tibet and the Pamirs. Although the resolution achievable for layer 3 (30–60 km depth) is poorer than for the shallower layers, our results show, that Q_μ is highest (about 160 or more) beneath the Tarim Basin and southcentral Mongolia and lowest (about 80) beneath the Pamirs.

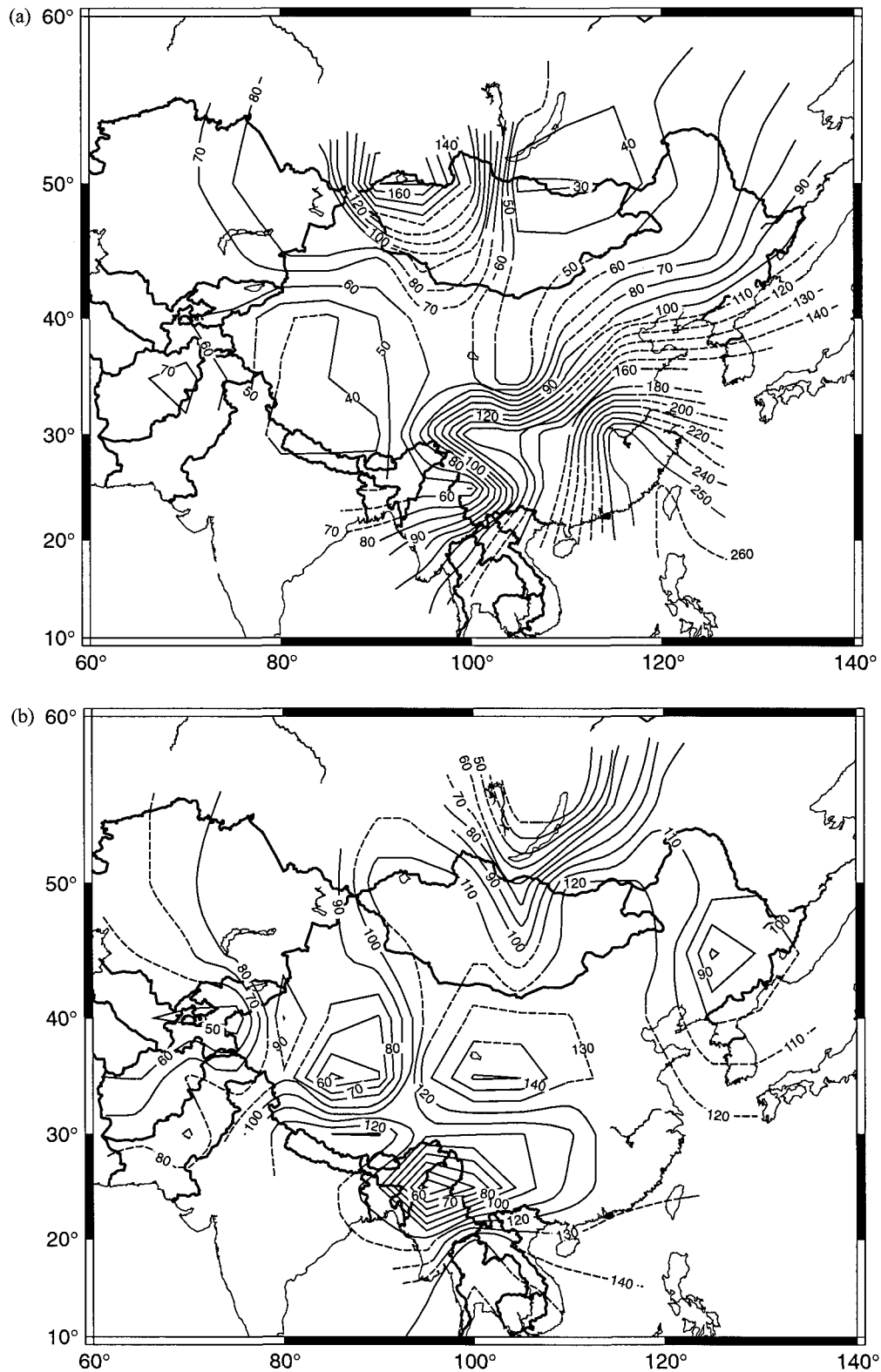


Figure 10. (a) Map of Q_μ variations throughout southeastern Asia for layer 1 (0–10 km depth). Solid contours lie in regions where path coverage is good and dashed contours where coverage requires significant interpolation. (b) Map of Q_μ variations throughout southeastern Asia for layer 2 (10–30 km depth). Solid contours lie in regions where path coverage is good and dashed contours where coverage requires significant interpolation.

Q_{μ} in all layers and its rate of increase with depth, exhibit large lateral variations throughout the eastern portion of southern Asia. Many of these variations correlate well with various aspects of the tectonics of the region. The regional variations, some over relatively small distances, can be expected to have significant effects on magnitude and yield determinations of seismic events as well as on our ability to discriminate between earthquakes and explosions in this easternmost part of southern Asia.

ACKNOWLEDGMENTS

This research was supported by contract DTRA-01-00-C-0213 of the Defense Threat Reduction Agency. All maps were drawn using the Generic Mapping Tools (GMT) developed by P. Wessel and W. H. F. Smith. R. Herrmann wrote the programs for computing amplitude spectra and L. Cong wrote the programs for plotting spectral comparisons used in this study.

REFERENCES

- Anderson, D.L., Ben-Menahem, A. & Archambeau, C.B., 1965. Attenuation of seismic energy in the upper mantle, *J. geophys. Res.*, **70**, 1441–1448.
- Cheng, C.C. & Mitchell, B.J., 1981. Crustal Q structure in the United States from Multi-mode Surface Waves, *Bull. seism. Soc. Am.*, **71**, 161–181.
- Chun, K.Y. & Yoshi, T., 1977. Crustal structure of the Tibetan plateau: A surface-wave study by a moving window analysis, *Bull. seism. Soc. Am.*, **67**, 735–750.
- Chung, S.-L., Jahn, B.-M., Wu, G., Lo, C.-H. & Cong, B., 1998. The Emeishan flood basalt in SW China: A mantle plume initiation model and its connection with continental breakup and mass extinction at the Permian-Triassic boundary, in *Mantle Dynamics and Plate Interactions in East Asia*, Vol. 27, pp. 47–58, eds Flower, M.F.J., Chung, S.-L., Lo, C.-H. & Lee, T.-Y., Geodynamics Ser., Am. Geophys. Union, Washington, DC.
- Cong, L. & Mitchell, B.J., 1998. Seismic velocity and Q structure of the Middle Eastern crust and upper mantle from surface wave dispersion and attenuation, *Pure appl. Geophys.*, **153**, 503–538.
- Curtis, A., Trampert, J., Snieder, R. & Dost, B., 1998. Eurasian fundamental mode surface wave phase velocities and their relationship with tectonic structures, *J. geophys. Res.*, **103**, 26 919–26 947.
- Dziewonski, A.M., Bloch, S. & Landisman, M., 1969. A technique for the analysis of transient seismic signals, *Bull. seism. Soc. Am.*, **59**, 427–444.
- Ekström, G., Tromp, J. & Larson, E.W.F., 1997. Measurements and global models of surface wave propagation, *J. geophys. Res.*, **102**, 8137–8157.
- Jemberie, A.L. & Mitchell, B.J., 2001. Regional variations in the shear-wave Q structure of southern Asia, *Proc. 23rd Seismic Research Review: Worldwide Monitoring of Nuclear Explosions*, pp. 55–61, Jackson Hole, WY.
- Khutorskoy, M.D. & Yarmoluk, V.V., 1989. Heat flow, structure and evolution of the lithosphere of Mongolia, *Tectonophysics*, **164**, 315–322.
- Kijko, A. & Mitchell, B.J., 1983. Multimode wave attenuation and Q_{μ} in the crust of the Barents shelf, *J. geophys. Res.*, **88**, 3315–3328.
- Menzies, M.A. & Xu, Y., 1998. Geodynamics of the North China Craton, in *Mantle Dynamics and Plate Interactions in East Asia*, Vol. 27, pp. 155–165, eds Flower M.F.J. et al., Geodynamics Series, Am. Geophys. Union, Washington, DC.
- Metcalf, I., 1990. Allochthonous terrane processes in Southeast Asia, *Phil. Trans. Roy. Soc. Lond.*, A, **331**, 625–640.
- Mitchell, B.J., 1975. Regional Rayleigh wave attenuation in North America, *J. geophys. Res.*, **80**, 4904–4916.
- Mitchell, B.J., 1995. Anelastic structure and evolution of the continental crust and the upper mantle from seismic surface wave attenuation, *Rev. Geophys.*, **33**, 441–462.
- Mitchell, B.J., Pan, Y., Xie, J. & Cong, L., 1997. L_g coda Q variations across Eurasia and its relation to crustal evolution, *J. geophys. Res.*, **102**, 22 767–22 779.
- Mitchell, B.J. & Cong, L., 1998. L_g coda Q and its relation to the structure and evolution of continents: A global perspective, *Pure appl. Geophys.*, **153**, 655–663.
- Molnar, P. & Tapponnier, P., 1975. Cenozoic Tectonics of Asia: Effects of a Continental Collision, *Science*, **189**, 419–426.
- Nelson, K.D. et al., 1996. Partially molten middle crust beneath southern Tibet: Synthesis of Project INDEPTH results, *Science*, **274**, 1684–1688.
- Ren, J., Jiang, C., Zhang, Z. & Qin, D., 1987. *Geotectonic Evolution of China*, Science Press, Beijing, Springer-Verlag, New York, p. 203.
- Ritzwoller, M.H. & Levshin, A.L., 1998. Eurasian surface wave tomography: Group velocities, *J. geophys. Res.*, **103**, 4839–4878.
- Sarker, G. & Abers, G.A., 1999. Lithospheric temperature estimates from seismic attenuation across range fronts in southern and central Eurasia, *Geology*, **27**, 427–430.
- Sengör, A.M.C., 1987. Tectonics of the Tethysides: Orogenic collage development in a collisional setting, *Ann. Rev. Earth Planet. Sci.*, **15**, 213–244.
- Smith, A.D., 1998. The Geodynamic Significance of the Dupal Anomaly in Asia, in *Mantle Dynamics and Plate Interactions in East Asia*, Vol. 27, pp. 89–105, eds Flower, M.F.J., Chung, S.-L., Lo, C.-H. & Lee, T.-Y., Geodynamic Series, Am. Geophys. Union, Washington, DC.
- Tapponnier, P. & Molnar, P., 1977. Active faulting and Tectonics in China, *J. geophys. Res.*, **82**, 2905–2930.
- Trampert, J. & Woodhouse, J.H., 1995. Global phase velocity maps of Love and Rayleigh waves between 40 and 150 seconds, *J. geophys. Res.*, **122**, 675–690.
- Tsai, Y.B. & Aki, K., 1970. Precise focal depth determination from amplitude spectra of surface waves, *J. geophys. Res.*, **75**, 5729–5743.
- van Heijst, H.J. & Woodhouse, J., 1999. Global high-resolution phase velocity distributions of overtone and fundamental-mode surface waves by mode branch stripping, *Geophys. J. Int.*, **137**, 601–620.
- Wier, S., 1982. Surface wave dispersion and Earth structure in southeastern China, *Geophys. J. R. astr. Soc.*, **69**, 33–47.
- Wu, F.T., 1997. Rayleigh wave group velocity tomography of Siberia, China and the vicinity, *Pure appl. Geophys.*, **149**, 249–264.
- Xie, J., 2002. L_g Q in the Eastern Tibetan Plateau, *Bull. seism. Soc. Am.*, **92**, 871–976.

Frequency-Dependent Shear-wave Q Models for the Crust of China and Surrounding Regions

ALEMAYEHU L. JEMBERIE¹ and BRIAN J. MITCHELL²

Abstract—Starting with fundamental-mode Rayleigh-wave attenuation coefficient values (γ_R) predicted by previously determined frequency-independent models of shear-wave Q (Q_μ), we have obtained frequency-dependent Q_μ models that explain measured values of γ_R as well as of Lg coda Q and its frequency dependence at 1 Hz (Q_o and η , respectively) for China and some adjacent regions. The process combines trial-and-error selection of a model for the depth distribution of the frequency dependence parameter (ζ) for Q_μ with a formal inversion for the depth distribution of Q_μ at 1 Hz. Fifteen of the derived models have depth distributions of ζ that are constant, or nearly constant, between the surface and a depth of 30 km. ζ distributions that vary with depth in the upper 30 km are necessary to explain the remaining seven models. ζ values for the depth-independent models vary between 0.4 and 0.7 everywhere except in the western portion of the Tibetan Plateau where they range between about 0.1 and 0.3 for three paths. These low ζ values lie in a region where Q_{Lg} and crustal Q_μ are very low and suggest that they should also be low for high-frequency propagation. The models in which ζ varies with depth all show a decrease in that value ranging between 0.55 and 0.8 in the upper 15 km of the crust and (with two exceptions where $\zeta = 0.0$) between 0.3 and 0.55 in the depth range 15–30 km. The distribution of ζ values between 0.6 and 0.8 (the higher part of the range) in the upper crust indicates that high-frequency waves will propagate most efficiently, relative to low-frequency waves, in a band that includes, and strikes north-northeastward from the path between event 212/97 and KMI to the path between event 180/95 and station HIA in the north.


Key words: ■ ■.

Introduction

Most mechanisms for intrinsic Q in the Earth predict that it should vary with frequency (e.g., JACKSON and ANDERSON, 1970). The variation of Q with frequency is usually considered to vary as $Q \sim \omega^a$ where the exponent a is termed the frequency dependence parameter and may be different for different attenuating waves. In the present study we represent the parameter for shear-wave Q (Q_μ) by ζ and for Lg coda Q (Q_{Lg}^c) by η . Several studies have addressed the question of frequency dependence of Q in the mantle and have found it to be necessary for simultaneously explaining the attenuation rate of both low- and high-frequency waves. Studies have invoked

¹ CERI, University of Memphis, 3876 Cental Avenue, Memphis, Tennessee 38152, U.S.A.

² Department of Earth and Atmospheric Science, Saint Louis University, 3507 Laclede Ave., St. Louis, Missouri 63103, U.S.A.

	S	B	0	1	2	5	7	7	B	Dispatch: 24.7.2004	Journal: Pure and applied Geophysics	No. of pages: 16
	Journal number		Manuscript number							Author's disk received <input checked="" type="checkbox"/>	Used <input checked="" type="checkbox"/>	Corrupted <input type="checkbox"/>

frequency dependence to reconcile Q values observed for free oscillations of the Earth and 1-Hz body waves (JEFFREYS, 1967; LIU *et al.*, 1976) to explain shear-wave Q observed for ScS waves at low and high frequencies (SIPKIN and JORDAN, 1979), and to explain variations in Q with frequency for teleseismic P and S waves in the range 0.02–4.0 Hz (DER *et al.*, 1982). Frequency dependence of Q for upper mantle material rock has also been observed in laboratory experiments (e.g., GUEGUEN *et al.*, 1989; JACKSON *et al.*, 2003).

Fewer studies have addressed the question of frequency dependence for Q at crustal depths. Combined inversions of surface-wave attenuation at periods between about 5 and 50 s and of Lg coda Q at 1 Hz have shown that Q_{μ} in the continental crust varies with frequency at least at frequencies of about 1 Hz and above (MITCHELL, 1980; MITCHELL and XIE, 1994). Determinations of Lg Q (Q_{Lg}) (e.g., BENZ *et al.*, 1997) or Lg coda Q (Q_{Lg}^C) (e.g., XIE and MITCHELL, 1990a,b) typically suggest the need for frequency-dependent values. It, however, has also been found possible to explain frequency-dependent Q_{Lg} or Q_{Lg}^C with a frequent-independent Q_{μ} model that contains a rapid increase in value at mid-crustal depths (MITCHELL, 1991).

Theoretical work has shown that Q frequency dependence may be associated with intrinsic energy loss due to temperature (GUEGUEN *et al.*, 1989) or to movements of fluid in permeable rock (O'CONNELL and BUDIANSKY, 1977). Recent studies (HAMMOND and HUMPHREYS, 2000; FAUL *et al.*, 2003) have concluded that the latter mechanism is not plausible at mantle depths where pressures are high, although research on this question, to our knowledge, has not yet been conducted for crustal rock at lower pressures. Some calculations, using realistic values for temperature and the frequency dependence parameter for Q , as well as assumed values for Q activation energy, suggest that temperature differences cannot explain regional differences between crustal Q values for the eastern and western United States (MITCHELL, 1995). If this result is correct it suggests that regional Q variations in the upper crust are likely to be caused by regional variations in fluid content in crustal rock. Frequency dependence of Q , at least at high frequencies, may also be attributed to scattering from heterogeneities in material traversed by seismic waves (e.g. DAINTY *et al.*, 1987).

That Q varies with frequency, at least in some portions of the crust and upper mantle and over the frequency range that is relevant to seismic wave propagation over near and regional distances, appears to be well established. Consequently this frequency dependence may be of great practical consequence for magnitude determinations at near and regional distances and in nuclear test ban treaty monitoring, for determining detection thresholds and for the implementation of methods for discriminating between earthquakes and explosions.

In this study we determine frequency dependence values (ζ) for crustal Q_{μ} that simultaneously explain the attenuation observed for fundamental-mode Rayleigh waves at intermediate periods (about 5–50 s) and values of Q_{Lg}^C observed in the southeastern portion of Eurasia that includes China and some adjacent regions. This

will allow us to extend the applicability of previously determined frequency-independent Q_μ models determined from surface waves to higher frequencies that characterize waves recorded at near and regional distances.

Our approach differs from that used in previous surface-wave studies of Q_μ frequency dependence in that we were able, for each path, to use fundamental-mode Rayleigh-wave data and higher-frequency Lg coda data recorded by the same instrument. Earlier studies, before the widespread availability of broadband data (e.g., MITCHELL, 1980), used different instruments for low- and high-frequency data. The top trace in Figure 1 shows ground motion recorded by the broadband station ULN in Mongolia for an earthquake about 530 km distant from Lake Baikal. A seismogram, if recorded by a long-period instrument of the World Wide Standard Seismograph Stations (WWSSN), would be similar to the middle trace of Figure 1 which is obtained by low-pass filtering the upper trace at periods above 4 s. If recorded by a short-period instrument of the WWSSN the seismogram would look like the bottom trace of Figure 1 which was obtained by band-pass filtering the upper trace around 1 Hz.

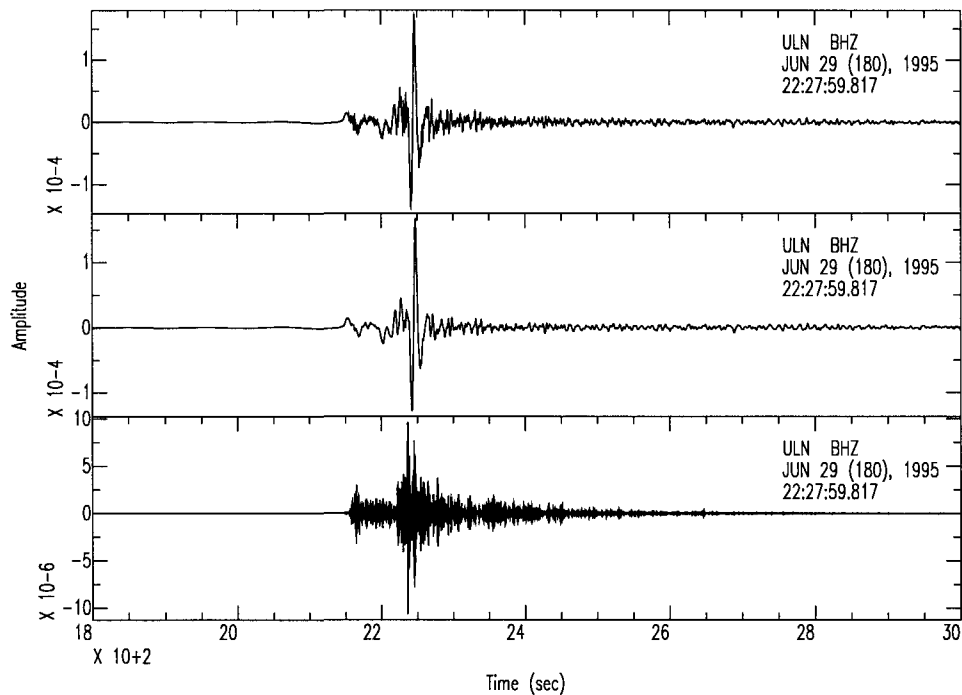


Figure 1

Vertical-component seismogram recorded by the broadband instrument at station ULN for an earthquake that occurred on 29 June, 1995 at an epicentral distance of some 530 km. The top trace shows the original broadband ground motion; the middle trace is the original record after it has been low-pass filtered for frequencies below 0.25 Hz (periods above 4 s), and the bottom trace is the original record after it has been bandpass filtered around 1 Hz.

Determination of Q_μ Structure Using Fundamental-mode Rayleigh Waves

Using a single-station multimode method, JEMBERIE and MITCHELL (2003) determined three-layer frequency-independent Q_μ models for the southeastern portion of Asia that includes China and some adjacent regions. It used surface waves that were well-recorded at surface-wave frequencies (about 5–50 s), an example of which appears in the middle trace of Figure 1. They mapped Q_μ variations for two depth ranges, 0–10 and 10–30 km and also estimated Q_μ in the depth range 30–60 km but with less reliability. They found large regional variations of Q_μ in all of the layers. Q_μ in layer 1 (the upper 10 km) varies between, approximately 250 in southeastern China to about 40 throughout most of the western Tibetan Plateau. In layer 2 (10–30 km depth) Q_μ varies between some 140 in central and eastern China and about 60 in western Tibet and the Burma-Thailand region. The low Q_μ values in western Tibet are among the lowest found in any continental region and correlate spatially with the lowest values of Q_{Lg} ever reported (XIE, 2002).

In order to obtain frequency-dependent Q_μ models our process requires that we invert curves of fundamental-mode Rayleigh-wave attenuation coefficient values (γ) versus period. We did not measure these directly, but instead computed γ values for the Q_μ models of JEMBERIE and MITCHELL (2003) along with appropriate velocity models. This computation is the first step in the inversion process described in a later section.

Lg Coda Q

Lg is usually the most prominent high-frequency phase (~ 0.5 Hz and higher) recorded on seismograms at regional distances in continents and can be observed at distances as great as 3000 km. Because it is so well recorded it has been used to determine magnitudes of small events at regional distances (NUTTLI, 1973) and to study regional variations of attenuative properties of the crust. In stable regions it is characterized by group velocities of about 3.5 km/s and can be as low as 3.2 or 3.3 km/s in tectonically active regions.

Lg can be represented as a superposition of many higher-mode Rayleigh waves at high frequencies. Computed Lg has a relatively sharp onset followed by oscillations or coda that can continue for several minutes if the crustal model used for the computations contains low-velocity layers in the uppermost crust (see the bottom trace in Fig. 1). The coda of observed Lg waves usually continues for a longer time than can be theoretically predicted by theoretical seismogram computations using plane-layer models. These additional oscillations are generally attributed to scattering of wave energy from crustal heterogeneities. Paradoxically, even though the coda of seismic waves is largely due to scattering, theoretical and computational

work indicates that measurements of Q using coda yield values of intrinsic Q rather than scattering Q (e.g., WENNERBERG, 1993). For this reason we combine surface-wave attenuation at intermediate periods (with wavelengths likely to be considerably longer than dimensions of heterogeneities) with Lg coda, at frequencies (near 1 Hz) that are likely to be affected by scattering, to invert for frequency-dependent models of Q_μ for the crust.

Our method for determining crustal Q_μ models is described in the following section. Those models should explain measured values for fundamental-mode Rayleigh-wave attenuation as well as average values of Q_o and η for Q_{Lg}^C along the paths of propagation. The utilization of Rayleigh-wave attenuation was discussed in the previous section. Tomographic maps of Q_o and η at 1 Hz are available for most of Eurasia, including our region of study (MITCHELL *et al.*, 1997). The Q_o values vary between about 150 and 1000 with the lower values occurring in a broadband, the Tethysides belt, that stretches across southern Asia, including China and some adjacent regions pertinent to this study.

Method

As a first step toward determining the frequency dependence of Q_μ and how it may vary with depth in China we have developed a method by which Q_μ frequency dependence can be obtained for our crustal models using a combined forward modeling/formal inversion procedure. It is a variation of a previously developed procedure (MITCHELL and XIE, 1994) and obtains a depth distribution of ζ that reconciles Q_μ values at 1 Hz with those obtained at surface-wave periods (about 5–50 s). Because simultaneous inversions for Q_μ and ζ include more parameters than do inversions for Q_μ alone, an additional level of non-uniqueness is introduced in the models. The process proceeds as follows:

1. Compute attenuation coefficients for the fundamental Rayleigh mode, as a function of period, for the pertinent frequency-independent Q_μ models of JEMBERIE and MITCHELL (2003) and the corresponding velocity models. For our region of study we use the shear-velocity models from JEMBERIE (2002) except for Tibet where we used a model from CHUN and YOSHII, (1977).
2. Assume a depth distribution for the frequency dependence, ζ , of Q_μ and use the attenuation coefficients obtained in step 1 to invert for a new, frequency-dependent, Q_μ model.
3. Calculate the fundamental-mode Rayleigh-wave attenuation coefficient values which are predicted by the model obtained in step 2 and compare them with the values of step 1. An example appears in Figure 2. If they agree within reasonable uncertainties go to step 4; if not, try a new distribution of ζ .
4. Extend step 3 by computing Q_μ at frequencies of interest (1 Hz for the present study). Figure 3 shows an example of 1 Hz Q_μ models computed using five different ζ distributions, assumed to be constant with depth, for a path between

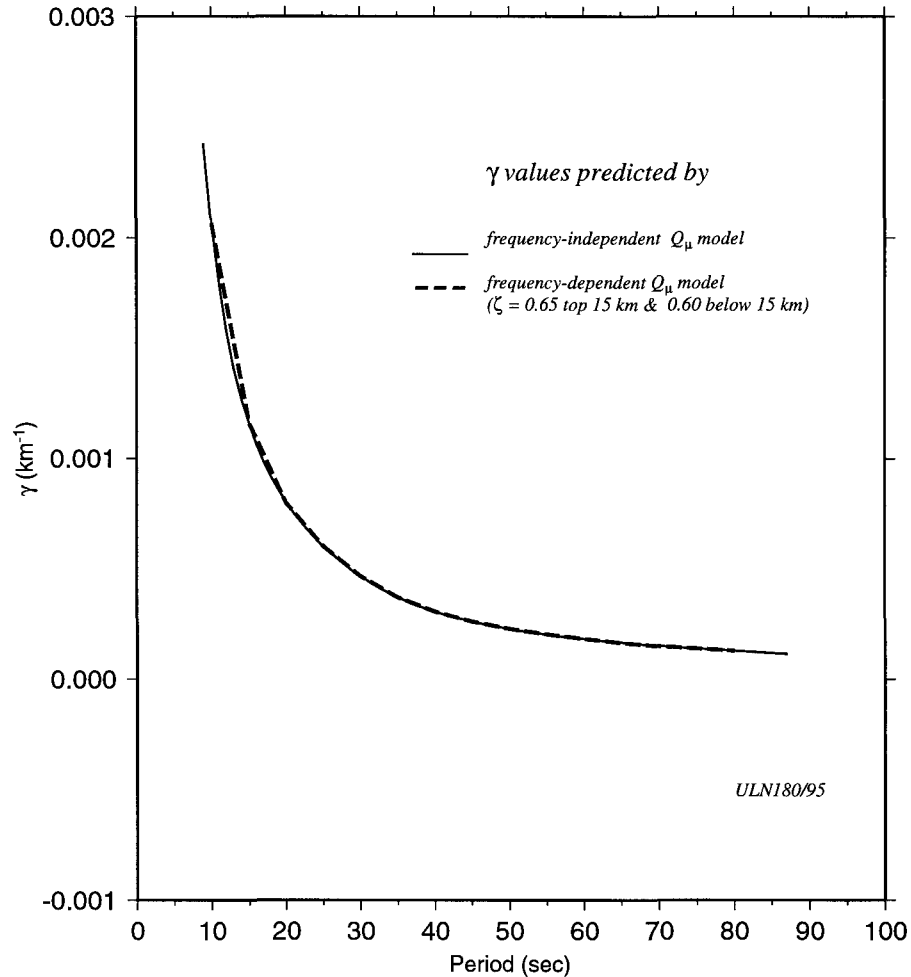


Figure 2

Comparison of Rayleigh-wave attenuation coefficients predicted by the three-layer frequency-independent model of Q_μ with a frequency-dependent model for spectra obtained at station ULN for event 180/95. The necessary ζ values are 0.65 for depths between 0 and 15 km and 0.60 for depths greater than 15 km.

station BRVK and an event that occurred on day 325 of the year 1988 (325/98 in Figs. 5 and 6).

5. Compute synthetic Lg seismograms (Fig. 4) at several distances from a seismic source using the known velocity model and the Q_μ model obtained at 1 Hz.
6. Apply the stacked spectral ratio (SSR) method of XIE and NUTTLI (1988) to the set of synthetic seismograms in step 5 to obtain values of Q_o and η predicted by the derived Q_μ model and compare them to the measured values from maps of Q_o and η (MITCHELL *et al.*, 1997) in Figures 5 and 6.

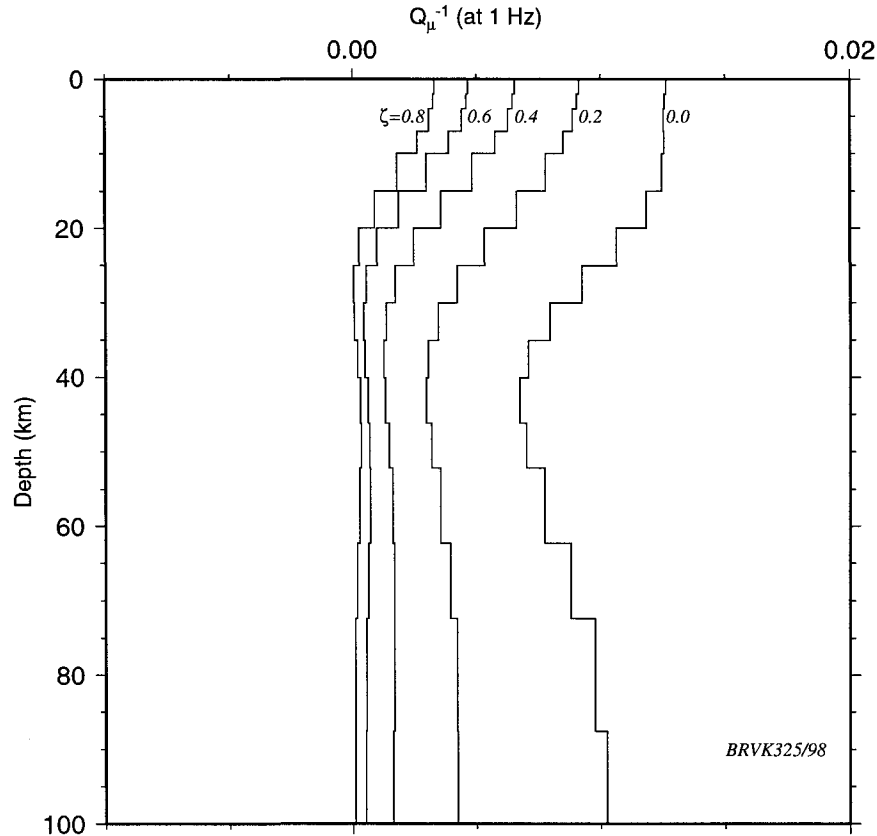


Figure 3
1-Hz Q_μ models computed using five different values of Q_μ frequency dependence (ζ).

7. If necessary, change the depth distribution of ζ in step 2 and repeat the procedure.

Table 1 shows derived Q_o and η values for five different ζ values for a path between event 325/98 and station BRVK. Values of both Q_o and η increase as the value of ζ increases. Comparison of Q_o values in Table 1 with Fig. 5 shows that the best value of ζ that can predict Q_o lies between 0.4 and 0.6. We found (Fig. 7d) that a ζ value of 0.55 best predicts the value of Q_o observed for that path (647 ± 51) and also predicts the η value of 0.37 ± 0.03 . This value is lower than the average ζ value (about 0.5 on average) for the path in Fig. 6. In cases, such as this, where Q_o and η cannot both be fit precisely, we assume that Q_o is more likely to be measured more accurately than η . η values may be inaccurate because they are obtained by differencing values of Q at two different frequencies.

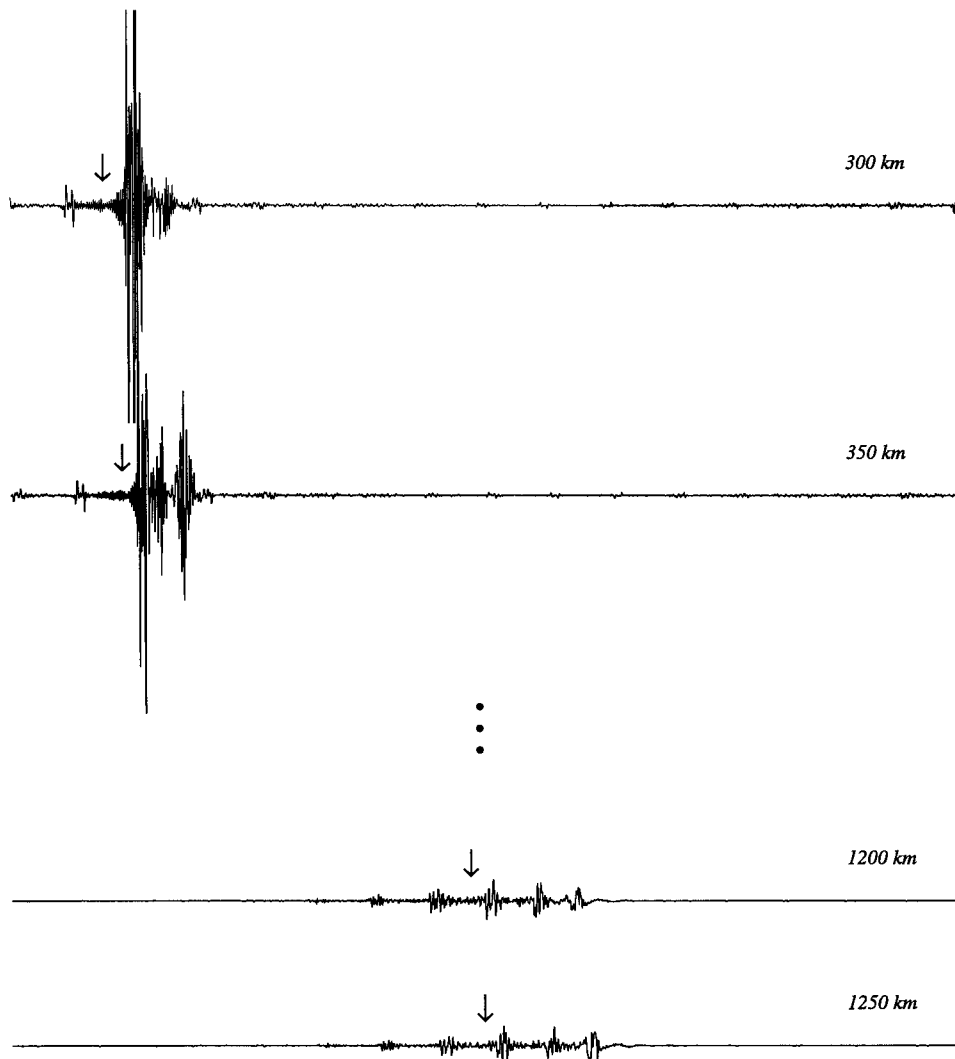


Figure 4

Synthetic Lg seismograms generated using the Q_μ structure obtained at 1 Hz and the velocity model for a subregion of China. The arrows show the predicted onset times of Lg.

Results

The frequency-dependent models obtained using the above procedure appear in Fig. 7a–d. The solid lines on the left-hand side of each pair of boxes are frequency-independent Q_μ models obtained using the single-station multimode method (JEMBERIE and MITCHELL, 2003) and the dashed lines show models at 1 Hz using our procedure for obtaining Q_μ frequency dependence. The boxes on the right-hand

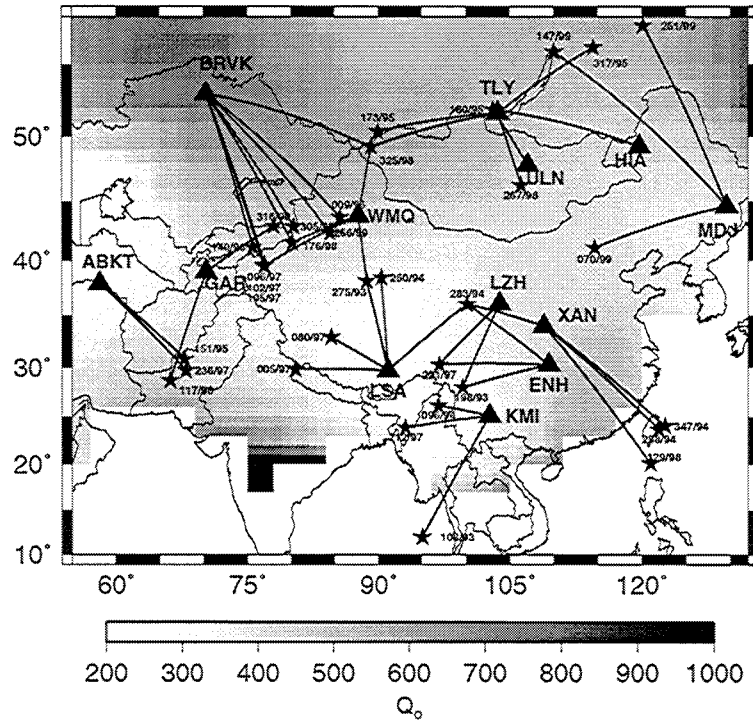


Figure 5

Tomographic map of Lg coda Q at 1 Hz (Q_0) for most Eurasia (modified from MITCHELL *et al.*, 1997), depicting paths between events and stations where frequency-independent models of Q_μ structure were determined by JEMBERIE and MITCHELL (2003).

side of each pair show the assumed distributions of ζ with depth. For 15 of the 22 models a constant value of ζ or a distribution that varies with depth by no more than 0.05 produced acceptable results. Values for these models range between 0.4 and 0.7 throughout the region of study except the western portion of the Tibetan Plateau where values lie in the range 0.1–0.3. One path, 283/94 to LSA in the eastern portion of the Tibetan Plateau has a ζ value 0.45 which is intermediate between values for paths in the western part of the plateau and paths outside, and to the east of the plateau.

The remaining seven models require that ζ values at depths greater than 15 km be smaller than those in the upper 15 km of the crust. For the upper 15-km thick layer ζ ranges between 0.55 and 0.8, and for greater depths ranges (with two exceptions) between 0.3 and 0.55. The exceptional values are both 0.0. Values of Q_0 and η for Lg attenuation at 1 Hz predicted by the models appear with each pair of panels. Note that, as shown by the model in the upper left of Figure 7a, a model with a nearly frequency-independent Q_μ can still produce a frequency-dependent Q_{Lg} value if Q_μ increases rapidly with depth at mid-crustal depths. This phenomenon was shown to

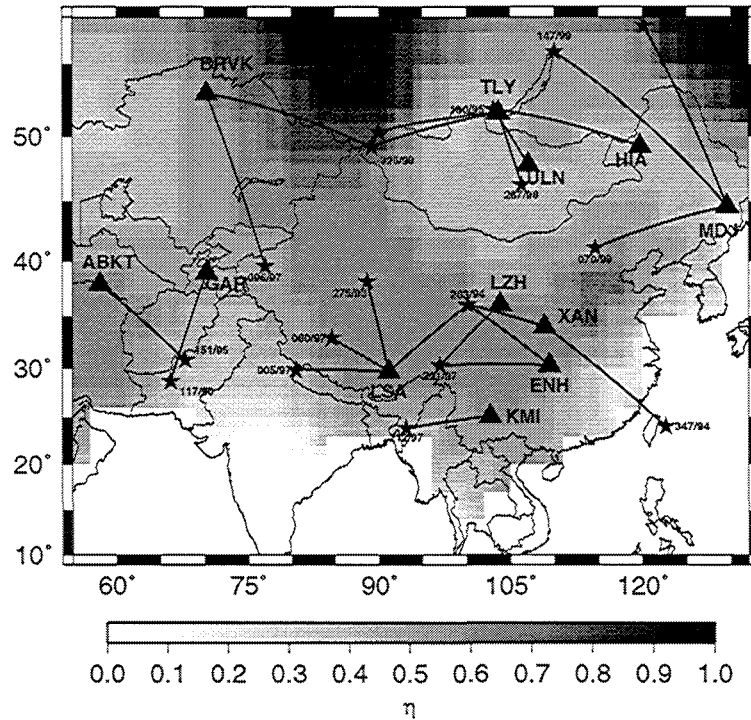


Figure 6

Tomographic map of the frequency dependence (η) of Lg coda Q at 1 Hz for most of Eurasia (modified from MITCHELL *et al.*, 1997) delineating paths between events and stations.

occur in the crust of the Basin and Range province in the western United States (MITCHELL, 1991).

The low values for ζ in the western Tibetan Plateau coincide with very low values of Q_μ found in the crust of this region using multimode surface waves (JEMBERIE and MITCHELL, 2003), as well as with very low Q_{Lg} values at 1-Hz frequencies (XIE, 2003). These results indicate that surface-waves at periods of ~ 5 –50 s as well as Lg or Lg

Table 1

Lg Q at 1 Hz (Q_0) and frequency dependence (η) values derived from the stacked spectral ratios (XIE and NUTTLI, 1988) of the synthetic seismograms obtained using the 1-Hz shear-wave Q (Q_μ) structure and its frequency dependence (ζ) for the path between event 325/98 and station BRVK. The numbers in column for F give the frequency ranges utilized in the determinations.

ζ	Q_0	η	Frequency Range
0.0	117 \pm 14	0.068 \pm 0.266	0.09–2.0
0.2	224 \pm 12	0.172 \pm 0.027	0.8–4.0
0.4	399 \pm 22	0.326 \pm 0.024	0.9–5.0
0.6	762 \pm 76	0.387 \pm 0.040	0.8–5.0
0.8	837 \pm 282	0.833 \pm 0.189	2.0–6.0

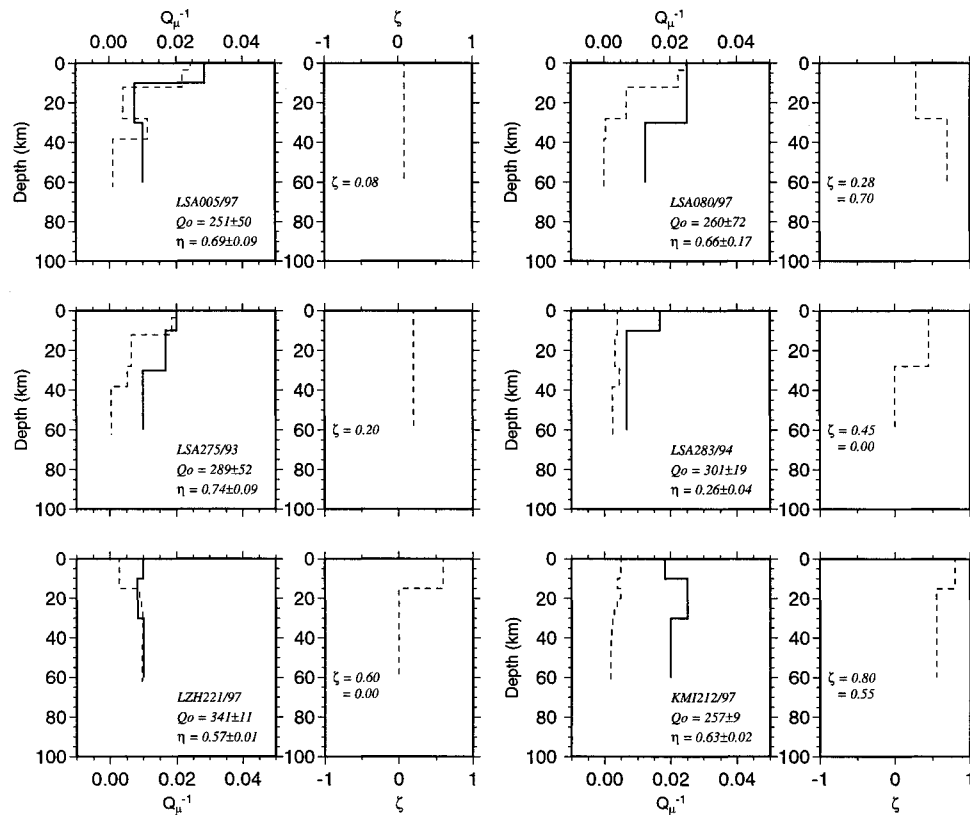


Figure 7a

Frequency-dependent models of Q_μ structure for Tibet and the southernmost portion of the study area. The solid line in the left-hand panels for each path presents frequency-independent Q_μ models that explain measured Rayleigh-wave attenuation at periods between about 5 and 50 s. The model delineated by the dashed line shows a Q_μ model at 1 Hz that explains both fundamental-mode Rayleigh-wave attenuation and measured Lg coda Q values at 1 Hz. The caption identifies the recording station and date of the event and gives values for Lg Q and its frequency dependence at 1 Hz that are predicted by the 1-Hz Q_μ model. The right-hand panel displays the depth distribution of Q_μ frequency-dependence that explains the frequency-dependent Q_μ model at 1 Hz on the left. The caption in this panel gives the value of ζ for the upper 15 km of the model (first number) and for the depth range between 15 and 60 km (second number).

coda at 1 Hz, and probably higher frequencies, propagate less efficiently in western Tibet than anywhere else in our region of study. The rates of attenuation in this region for both surface-wave periods (~ 5 – 50 s) and Lg frequencies (\sim about 1 Hz) are the highest measured to date for any continental region. An early study of Q in the central Tibetan Plateau (CHANG and YAO, 1979), using spectral ratios of S and ScS waves, found a Q value of about 25 that must pertain predominantly to upper mantle depths.

An interpretation of our results in terms of a continuous relaxation model for the crust would indicate that the relaxation spectrum (Q_μ^{-1}) for the western Tibetan

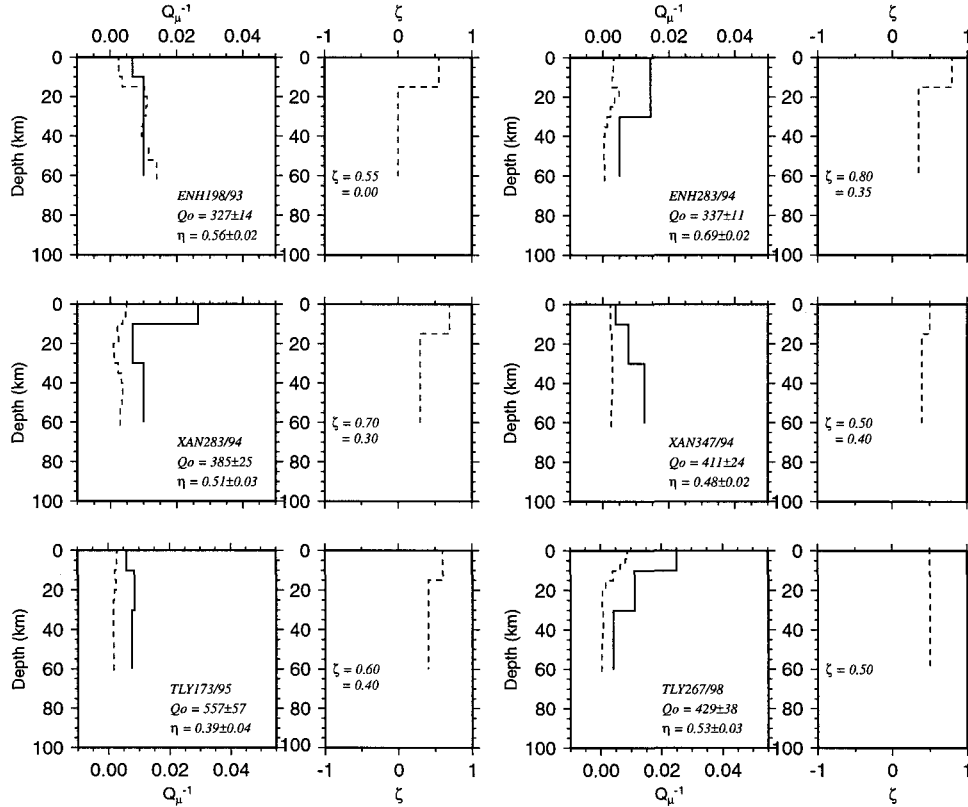


Figure 7b

Frequency-dependent models of Q_μ structure for central and eastern China, Mongolia and peripheral regions. See the caption for Figure 7a for an explanation of the models and symbols.

Plateau is shifted to higher frequencies compared to other parts of our region of study, an effect that could be produced by higher temperatures or elevated levels of tectonic stress. Sublithospheric mantle heat flow estimated by ARTEMIEVA and MOONEY (2001) is elevated throughout the western and central parts of the Tibetan Plateau relative to surrounding regions. It is probably pertinent that electrical resistivity values at mid- and lower-crustal depths are very low there (WEI *et al.*, 2001), suggesting the presence of melt or fluids that may be released by hydrothermal reactions initiated by the high temperatures.

Conclusions

We have obtained frequency-dependent models of Q_μ that explain the variation of fundamental-mode Rayleigh-wave attenuation coefficients with period predicted

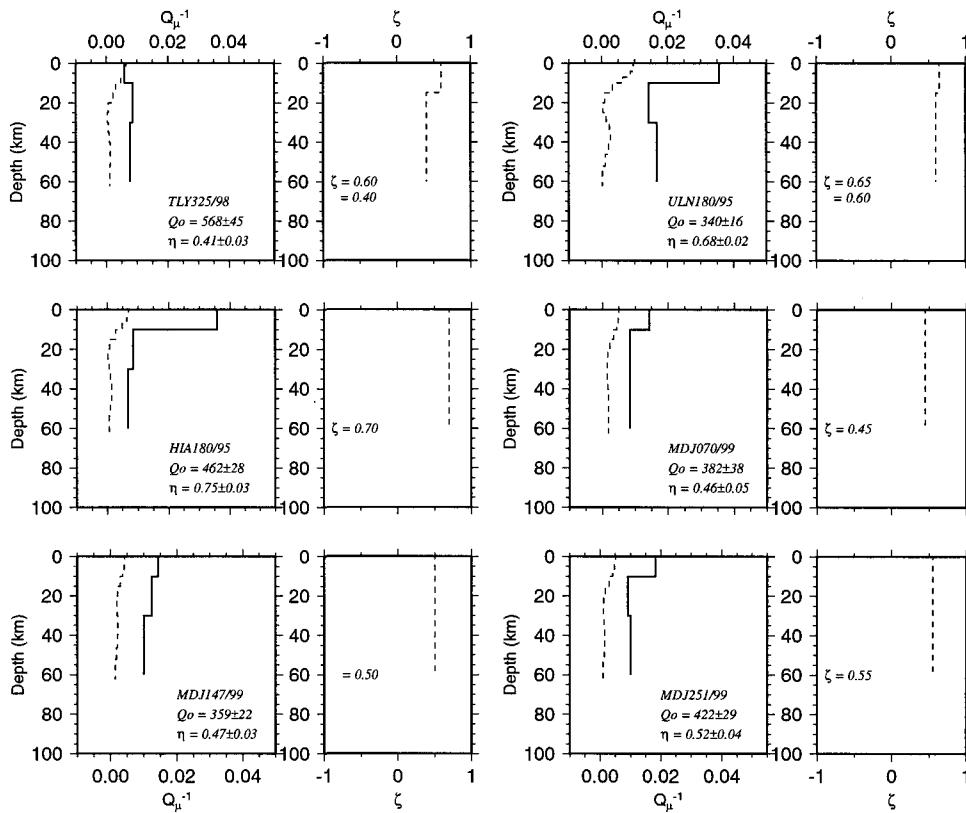


Figure 7c

Frequency-dependent models of Q_μ structure for paths in northern China, Mongolia and portions of southern Siberia. See the caption for Figure 7a for an explanation of the models and symbols.

by the Q_μ models of JEMBERIE and MITCHELL (2003) as well as previously mapped values of Q_o and η in China and some adjacent regions. ζ values for depth-independent models vary between 0.4 and 0.7 through most of the region of study, but range between 0.1 and 0.3 in the western portion of the Tibetan Plateau. The latter (low) ζ values coincide with regions where Q_{Lg} and crustal Q_μ were previously reported to be very low and indicate that high-frequency propagation should also be low compared to other regions. The models in which ζ varies with depth all manifest a decrease in that value ranging between 0.55 and 0.8 in the upper 15 km of the crust and between 0.3 and 0.55 (with two exceptional values) in the depth range 15–30 km. The distribution of highest ζ values (0.55–0.8) in the upper crust indicates that high-frequency waves will propagate most efficiently, relative to low-frequency waves, in a band that includes and strikes north-northeastward from the path between event 212/97 and KMI to the path between event 180/95 and station HIA in the north.

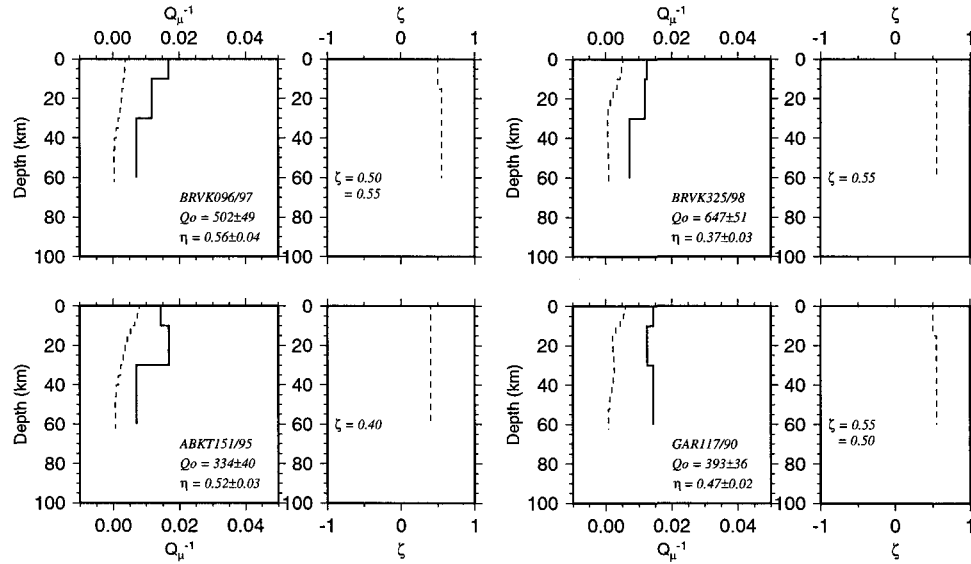


Figure 7d

Frequency-dependent models of Q_μ structure for the western portion of the study area. See the caption for Figure 7a for an explanation of the models and symbols.

Our results indicate that wave propagation at surface-wave periods ($\sim 5\text{--}50$ s), at 1 Hz and probably higher frequencies, are less efficient in western Tibet than anywhere else in our region of study and that the region is characterized by the least efficient propagation of seismic waves, at all seismic frequencies, yet known for any continental region. The low ζ values can be explained if wave propagation in the crust of this region can be characterized by a continuous relaxation model that has been displaced to higher frequencies by temperatures and/or tectonic stress levels that are higher than they are in surrounding regions.

Acknowledgments

We thank Lianli Cong for providing his code for plotting crustal Q models and Robert Herrmann for writing the mode summation code for computing Lg synthetics used in this study. Our work benefited from helpful discussions with Jack Xie at Lamont-Doherty Earth Observatory of Columbia University. This research was sponsored by the Defense Threat Reduction Agency Contract No. DTRA-01-00-C-0213.

REFERENCES

- ARTEMIEVA, I.M. and MOONEY, W.D. (2001), *Thermal Thickness and Evolution of Precambrian Lithosphere: A Global Study*, *J. Geophys. Res.* 106, 16,387–16,414.
- BENZ, H.M., FRANKEL, A and BOORE, D.M. (1997), *Regional Lg Attenuation for the Continental United States*, *Bull. Seismol. Soc. Am.* 87, 606–619.
- CHANG, L. and YAO, Z. (1979), *The Q-value of the Medium of the Tibetan Plateau around Lasa Region*, *Acta Geophys. Sinica* 22, 299–303.
- CHUN, K. and YOSHII, T. (1977), *Crustal Structure of the Tibetan Plateau: A Surface Wave Study by a Moving Window Analysis*, *Bull. Seismol. Soc. Am.* 67, 735–750.
- DAINTY, A.M., DUCKWORTH, R.M., and TIE, A. (1987), *Attenuation and Backscattering from Local Coda*, *Bull. Seismol. Soc. Am.* 77, 1728–1747.
- DER, Z.A., MCELFFRESH, T.W., and O'Donnell, A. (1982), *An Investigation of the Regional Variations and Frequency Dependence of Anelastic Attenuation of the Mantle under the United States in the 0.5–4 Hz Band*, *Geophys. J. Roy. Soc.* 69, 67–99.
- FAUL, U.H., FITZGERALD, J. D., and JACKSON, I. (2003) *Shear-wave Attenuation and Dispersion in Melt-bearing Olivine Polycrystals II. Microstructural Interpretation and Seismological Implications*, *J. Geophys. Res.*, in press.
- GUEGUEN, Y., DAROT, M., MAZOT P., and WOIRGARD, J. (1989), Q^{-1} of Forsterite Single Crystals, *Phys. Earth Planet. Inter.* 55, 254–258.
- HAMMOND, W.C. and HUMPHREYS, E.D. (2000), *Upper Mantle Seismic Wave Velocity: Effects of Realistic Partial Melt Geometries*, *J. Geophys. Res.* 105, 10,975–10,986.
- JACKSON, I., FAUL, U.H., FITZGERALD J.D., and TAN, B.H. (2003), *Shear-wave Attenuation and Dispersion in Melt-bearing Olive Polycrystals I. Specimen Fabrication and Mechanical Testing*, *J. Geophys. Res.*, in press.
- JACKSON, D.D. and ANDERSON, D.L. (1970), *Physical Mechanisms for seismic wave attenuation*, *Rev. Geophys.*, 8, 1–63.
- JEFFREYS, H. (1967), *Radius of the Earth's Core*, *Nature* 215, 1365–1366.
- JEMBERIE, A.L. (2002), *Shear-wave Attenuation and Velocity Studies in Southeastern Asia*, Ph.D. Dissertation, Saint Louis University, St. Louis, Missouri, USA, 218 pp.
- JEMBERIE, A.L. and Mitchell, B.J. (2003), *Shear-wave Q Structure and its Lateral Variation in the Crust of China and Surrounding Regions*, *Geophys. J. Int.*, submitted.
- LIU, H.P., ANDERSON, D.L., and KANAMORI, H. (1976), *Velocity Dispersion due to Anelasticity: Implications for Seismology and Mantle Composition*, *Geophys. J. Roy. Soc.* 47, 41–58.
- MITCHELL, B.J. (1980), *Frequency Dependence of Shear Wave Internal Friction in the Continental Crust of Eastern North America*, *J. Geophys. Res.* 85, 5212–5218.
- MITCHELL, B.J. (1991), *Frequency Dependence of Q_{Lg} and its Relation to Crustal Anelasticity in the Basin and Range Province*, *Geophys. Res. Ltr.* 18, 621–624.
- MITCHELL, B.J. (1995), *Anelastic Structure and Evolution of the Continental Crust and Upper Mantle from Seismic Surface-wave Attenuation*, *Rev. Geophys.* 33, 441–462.
- MITCHELL, B.J. and XIE, J. (1994), *Attenuation of Multiphase Surface Waves in the Basin and Range Province – III. Inversion for Crustal Anelasticity*, *Geophys. J. Int.* 116, 468–484.
- MITCHELL, B.J., PAN, Y., XIE, J. and CONG, L. (1997), *Lg Coda Q Variation across Eurasia and its Relation to Crustal Evolution*, *J. Geophys. Res.* 102, 22,767–22,779.
- NUTTLI, O.W. (1973), *Seismic Wave Attenuation and Magnitude Relations for Eastern North America*, *J. Geophys. Res.* 78, 876–885.
- O'CONNELL, R.J. and BUDIANSKY, B. (1977), *Viscoelastic Properties of Fluid – saturated Cracked Solids*, *J. Geophys. Res.* 82, 5719–5735.
- SIPKIN, S.A., and JORDAN, T.H. (1979), *Frequency Dependence of Q_{ScS}* , *Bull. Seismol. Soc. Am.* 69, 1055–1079.
- WEI, W., UNSWORTH, M., JONES, A., BOOKER, J., TAN, H., NELSON, D., CHEN, L., LI, S., SOLON, K., BEDROSIAN, P., JIN, S., DENG, M., LEDO, J., KAY, D., and ROBERTS, B. (2001), *Detection of Widespread Fluids in the Tibetan Crust by Magnetotelluric Studies*, *Science* 292, 716–718.

- WENNERBERG, L. (1993), *Multiple-scattering Interpretations of Coda-Q Measurements*, Bull. Seismol. Soc. Am. 83, 279–290.
- XIE, J. (2002), *Lg Q in the Eastern Tibetan Plateau*, Bull. Seismol. Soc. Am. 92, 871–876.
- XIE, J. and NUTTLI, O.W. (1988), *Interpretation of High-frequency Coda at Large Distances: Stochastic Modeling and Method of Inversion*, Geophys. J. 95, 579–595.
- XIE, J. and MITCHELL, B.J. (1990a), *A Back-projection Method for Imaging Large-scale Lateral Variations of Lg Coda Q with Application to Continental Africa*, Geophys. J. Int. 100, 161–181.
- XIE, J. and MITCHELL, B.J. (1990b), *Attenuation of Multiphase Surface Waves in the Basin and Range Province, I, Lg and Lg Coda*, Geophys. J. Int. 102, 121–137.

(Received February 11, 2003, accepted October 1, 2003)



To access this journal online:
<http://www.birkhauser.ch>
